MICROFLUIDIC CHIP-BASED SYSTEMS FOR MONITORING CANCER THERAPY

A THESIS SUBMITTED TO
THE GRADUATE SCHOOL OF ENGINEERING AND SCIENCE
OF BILKENT UNIVERSITY
IN PARTIAL FULFILLMENT OF THE REQUIREMENTS FOR
THE DEGREE OF
MASTER OF SCIENCE
IN
MATERIALS SCIENCE AND NANOTECHNOLOGY

By
Eylül Gülşen Yılmaz
December 2022

MICROFLUIDIC CHIP-BASED SYSTEMS FOR MONITORING CANCER THERAPY

By Eylül Gülşen Yılmaz

December 2022

We certify that we have read this thesis and that in our opinion it is fully adequate,in scope and in quality, as a thesis for the degree of Master of Science.

Fatih İnci (Advisor)

Ahmet Acar

Aykut Erbaş

Approved for the Graduate School of Engineering and Science:

Orhan Arıkan
Director of the Graduate School

ABSTRACT

MICROFLUIDIC CHIP-BASED SYSTEMS FOR MONITORING CANCER THERAPY

Eylül Gülşen Yılmaz
M.S. in Materials Science and Nanotechnology
Advisor : Fatih İnci
December 2022

In tumor microenvironment, cancer cells are exposed to a range of fluid shear stresses (FSS); yet, current *in vitro* three-dimensional (3D) models have limitations to investigate the impact of biophysical stimuli on cancer mechanism and chemoresistance in a dynamic manner. In the past few decades, vital demand for exploring biological significance of mechanical forces has led to the development of several innovative approaches. One of these approaches is the integration of microfluidic systems into cancer studies. The use of microfluidic chips has garnered increasing attention since they offer ease-of-manipulation, high-throughput, less material/reagent consumption, and low-cost. On the other hand, the researches have stated explicitly that tumor-derived extracellular vesicles (EVs) regulate local and systemic milieu to drive the development and spread of cancer through nano- and micron-sized vesicles they carry. In this thesis, breast cancer cells (MCF-7) have been utilized as a model cancer system, and accordingly, they are cultivated through SF-coated microfluidic systems in order to mimic tumor microenvironment, exhibiting a more dynamic condition. Simultaneously, traditional static culture of MCF-7 cells is also performed as a control group in order to understand the impact of flow conditions. The effects of FSS on gene expression—in particular, EpCAM and CK-18 genes, which are highly expressed in MCF-7 cells—have been examined at the end of cell culturing process. In addition, cancer cells developing any resistance to anti-cancer drugs on the course of FSS have been

investigated. In this regard, the cells are treated with either doxorubicin or docetaxel (anti-cancer drugs) in the cases of dynamic (microfluidic system) and static (tissue culture flask) culture conditions. Multi-Drug Resistance 1 (MDR-1) and Breast Cancer Resistance Protein (BCRP) gene expression levels have been assessed once anti-cancer treatment has been finalized. The final step of this study relies on the isolation and analysis of EVs from both static and dynamic conditions with the presence and absence of anti-cancer drug treatment. The utility of EVs has been evaluated deliberately as biomarkers for real-time monitoring of treatment efficacy.

Keywords : 3D cell culture, Microfluidic Chips, Cancer, Silk Fibroin, Extracellular Matrix, Anti-cancer Drug Resistance, Extracellular Vesicles (EVs)

ÖZET

KANSER TEDAVİSİNİN İZLENMESİ İÇİN MİKRO AKIŞKAN ÇİP TABANLI SİSTEMLER

Eylül Gülşen Yılmaz
Malzeme Bilimi ve Nanoteknoloji, Yüksek Lisans
Tez Danışmanı : Fatih İnci
Aralık 2022

Tümör mikro çevresinde, kanser hücreleri bir dizi sıvı kesme gerilimine (SKG) maruz kalır; bununla birlikte, mevcut *in vitro* üç boyutlu (3D) modellerin, biyofiziksel uyaranların kanser mekanizması ve kemorezistans üzerindeki etkisini dinamik bir şekilde araştırmak için sınırlamaları vardır. Son birkaç on yılda, mekanik kuvvetlerin biyolojik önemini keşfetmeye yönelik hayati talep, birkaç yenilikçi yaklaşımın geliştirilmesine yol açmıştır. Bu yaklaşımlardan biri de mikroakışkan sistemlerin kanser çalışmalarına entegrasyonudur. Mikroakışkan çiplerin kullanımı, manipülasyon kolaylığı, yüksek verim, daha az malzeme/reaktif tüketimi ve düşük maliyet sundukları için artan ilgi görmüştür. Öte yandan araştırmalar, tümör kaynaklı ekstraselüler veziküllerin (EV'ler), taşıdıkları nano ve mikron boyutlu veziküller aracılığıyla kanserin gelişimini ve yayılmasını sağlamak için lokal ve sistemik ortamı düzenlediğini açıkça belirtmektedir. Bu tezde meme kanseri hücreleri (MCF-7) model bir kanser sistemi olarak kullanılmış ve daha dinamik bir ortam sergileyerek tümör mikroçevresini taklit etmek için ipek fibroin kaplı mikroakışkan sistemler aracılığıyla kültürlenmektedirler. Eşzamanlı olarak, akış koşullarının etkisini anlamak için MCF-7 hücrelerinin geleneksel statik kültürü de bir kontrol grubu olarak kullanılır. Sıvı kesme geriliminin (SKG) gen ekspresyonu üzerindeki etkileri—özellikle MCF-7 hücrelerinde yüksek oranda eksprese edilen EpCAM ve CK-18 genleri—hücre kültürleme işleminin sonunda incelenmiştir. Ek olarak, SKG sırasında kanser hücrelerinin antikanser ilaçlara karşı herhangi bir direnç geliştirip geliştirmediği araştırılmıştır. Bu bağlamda, hücreler dinamik (mikroakışkan

sistem) ve statik (doku kültürü şişesi) kültür koşullarında doksorubisin veya dosetaksel (antikanser ilaçları) ile tedavi edilir. Antikanser tedavisi tamamlandıktan sonra Çoklu İlaç Direnci 1 (MDR1) ve Meme Kanseri Direnci Proteini (BCRP) genlerinin ekspresyon seviyeleri değerlendirildi. Bu çalışmanın son adımı, antikanser ilaç tedavisinin varlığı ve yokluğu ile EV'lerin hem statik hem de dinamik koşullardan izolasyonuna ve analizine dayanmaktadır. EV'nin faydası, tedavi etkinliğinin gerçek zamanlı izlenmesi için kasıtlı bir biçimde biyobelirteçler olarak değerlendirilmiştir.

Anahtar sözcükler : 3D hücre kültürü, Mikroakışkan, Kanser, İpek Fibroin, Ekstraselüler Matriks, Anti-kanser ilaç direnci, Ekstraselüler veziküller (EV)

To my dear family…

Acknowledgement

First and foremost, I would like to express my sincere gratitude to my supervisor Asst. Prof. Dr. Fatih İnci for his support, guidance, and inspiration during the entire period of my master studies. I am grateful to him for allowing me to work in his group. He has developed my scientific thinking throughout all my studies, and he has enabled me to progress continuously with the opportunities he has provided me, without him, I could not come to my current point. I cannot adequately convey my appreciation to him for his priceless patience and comments. I am grateful for the communication he provides not only in the work environment but also outside of work.

I would also like to thank the thesis committee, Asst. Prof. Dr. Aykut Erbaş and Asst. Prof. Dr. Ahmet Acar, for their guidance and support in my thesis.

I would also like to thank Bugamed Biotechnology and Gamze Kara Mağden. Her continuing support has never been lacking throughout my work.

I would like to express my deepest gratitude to Asst. Prof. Dr. Ayça Arslan Ergül. She helped me choose my profession during my high school years and taught me many things by being with me since my undergraduate years. I am very lucky to have crossed paths with someone like her. I am also grateful for her to lift me up even in my toughest moment. I would also like to thank all the members of Arslan-Ergül Lab. Especially, I want to thank Elif Akış. She has always supported me throughout my studies.

I would like to express my biggest thanks to my beloved family, to whom I dedicate this thesis. I am grateful to my dear grandparents Rıza - Gülşen Yılmaz and İhsan - Huriye Yılmaz, my dear parents Hakan - Aysun Yılmaz and my dearest brother Ekin Yiğit Yılmaz for all their support. I would be incomplete without my brother. I became who I am now because they taught me not to give up on what I knew to be true. In any case, they supported me and helped me as much as they could. I would also like to thank all my other family members and most of all my cousins for always supporting me and having fun and laughing together. I would like to thank Eren Kara for motivating me especially during my thesis period. Fortunately, he is both my cousin and my friend.

I would like to thank Dr. Özgecan Erdem, who has been with me throughout my academic process and has helped me a lot, especially recently. The pleasant times I spent with her motivated me a lot. She taught me many things that I did not know. Thank you very much for being a good friend as well as guiding me. I would also like to thank Yusuf

Aslan for making me laugh and always helping me. His support made me do many things easier. I would like to thank Esma Derin and Kutay Sağdıç, who have always supported me even though they are not with me physically lately. Also, thank you to all the other members of the Incilab.

Luckily, I made good friends, they all became my family. I would like to thank Narin Ilgım Ardıç Avcı for her friendship and academic assistance. It is very pleasant to be able to consult with her on the issues that I am stuck with. I would like to thank Merve Erşahin, Rıdvan Ergit, Selin Koç, Seda Çetin, Serdar Akboğa, Şevval Bilser Taşkın, and Batuhan Varol who have never left me alone during this difficult period. It would be unfair to call them friends, they are like my family.

In addition, I am very grateful to the Bilkent University-UNAM M.Sc. Program and the TÜBİTAK BİDEB 2232 - International Fellowship for Outstanding Researchers (Project number: 118C254) for funding my graduate studies.

Contents

CHAPTER 1 ..... **1**

1.INTRODUCTION 1

1.1 Cancer *1*

1.2 Microfluidics Chip Approach in Cancer Studies *5*

1.3 2D and 3D Cell Culture *10*

1.4 Extracellular Vesicles (EVs) as a Biomarker for Cancer *14*

CHAPTER 2 ..... **19**

2.MATERIALS AND METHOD 19

2.1 Materials *19*

2.2 Conventional Protocols for Cell Culture *19*

2.2.1 Static 2D Cell Culture 19

2.2.2 Static 3D Cell Culture 20

2.3 Cell Counting *21*

2.4 Fabricating Microfluidic Chips for Dynamic 3D Cell Culture *22*

2.5 Cell Culture under Dynamic 3D Condition *24*

2.6 Cell Imaging *25*

2.7 Anti-cancer Drug Studies *25*

2.8 Imaging of Anti-cancer Drugs Treated Cells *25*

2.9 RNA Isolation *26*

2.10 RNA Quantification *27*

2.11 cDNA Synthesis *27*

2.12 Confirming cDNA Synthesis *28*

2.13 Quantitative Real-Time Polymerase Chain Reaction (RT-qPCR) *29*

2.14 Isolating Extracellular Vesicles using a Microfluidic Device *30*

2.15 Isolating Extracellular Vesicles *31*

2.16 Determining Protein Concentration of Isolated Extracellular Vesicles *32*

2.17 Characterization Methods *32*

2.17.1 Characterization Surface Chemistry on Microfluidic Chips 33

2.17.1.1 Contact Angle 33
2.17.1.2 Fourier Transform Infrared Spectroscopy (FTIR) 33
2.17.1.3 X-Ray Photoelectron Spectroscopy (XPS) 34
2.17.2 Characterizing Extracellular Vesicles 35
2.17.2.1 Nanoparticle Tracking Analysis (NTA) 35
2.17.2.2 Scanning Electron Microscope (SEM) 35
2.17.2.3 Western Blot 36

CHAPTER 3 39

3.GENE EXPRESSION AND FLUID SHEAR STRESS RELATIONSHIP 39
3.1 Completion of the microfluidic chip 39
3.2 Cell Culturing 44
3.3 Gene Expression Analysis 48

CHAPTER 4 51

4.CHEMORESISTANCE STUDIES 51
4.1 Doxorubicin Studies for Static2D, Static3D and Dynamic Conditions 52
4.2 Docetaxel Studies for Static2D, Static3D and Dynamic Conditions 61
4.3 Gene Expression Analysis 70
4.3.1 Doxorubicin Gene Expression 70
4.3.2 Docetaxel Gene Expression 72

CHAPTER 5 74

5.EXTRACELLULAR VESICLES (EVs) STUDIES 74
5.1 Nanoparticle Tracking Analysis (NTA) Results 75
5.1.1 NTA analysis of Static2D, Static3D and Dynamic conditions without anti-cancer drug 75
5.1.2 Doxorubicin NTA Results 79
5.1.3 Docetaxel NTA Results 88
5.2 Scanning Electron Microscopy (SEM) Results 97
5.3 Western Blot Analysis 99

CHAPTER 6 102

6.CONCLUSION AND FUTURE PROSPECTS 102

List of Figures

Figure 1.1. This illustration shows ten important hallmarks of cancer cells. Reproduced from [5]. *2*

Figure 1.2. A representative image for biological variables that influence drug resistance. Tumors constitute of heterogeneous structure, and they are surrounded by a microenvironment comprised of membrane, capillaries, immune cells, and cancer ecology. Changes in the physical traits, genetic makeup, and environmental factors of the tumor build drug resistance. Reproduced from [21]. *4*

Figure 1.3. Advantages and disadvantages of cell culture methods performed on microfluidic chips and conventional method. Reproduced from [32]..... *7*

Figure 1.4. The use of microfluidic systems in cancer studies. Microfluidic chips offer pivotal advances in isolating circulating tumor cells (CTCs), understanding metastasis, and generating 3D tumor models and tumor-on-a-chip studies. Reproduced from [48]. 9

Figure 1.5. Elements of exosomes discovered in various proteome analyses and their distinct cellular materials are depicted. Reprinted with permission from [90]. Copyright 2022 American Chemical Society..... *15*

Figure 1.6. Exosomes and the establishment of pre-metastatic niches. The initial cancer cells release exosomes into the extracellular environment. The distribution and targeted organotrophic incorporation of these vesicles carrying oncoproteins or nucleic acids result in the formation of a pre-metastatic niche at the secondary site of cancer spread. Activation of many signaling pathways and stimulation of diverse immune cells at the secondary site aid in the establishment of a cancer-favorable inflammatory environment, which supports the effective metastasis of cancer cells [92]..... *16*

Figure 2.1. a) The design parameters of a microfluidic chip are presented. Black color indicates PMMA layers, red color indicates DSA films, and green color represents polystyrene layer. b) A microfluidic chip is constructed with many layers of PMMA, DSA films and polystyrene. The numbers of i-vii numbers indicate these layers from the top to the bottom. The numbers of viii-ix numbers state clamps. c) Top view of a microfluidic chip is exhibited. d) Top view of a microfluidic chip with clamps and screws. e) Through tubings attached to inlet and outlet ports, sampling and collecting cells are utilized... 23

Figure 2.2. Images of cells cultured in a microfluidic chip after 24 hours. Cells are distributed evenly in different regions of the chip. 24

Figure 2.3. a) Design parameters of a microfluidic chip is displayed. Black color state PMMA layers and red color represents DSA films. b) The assembly order of chip components is represented by roman numbers. Moreover, membranes with pore sizes of 200 nm and 50 nm are integrated between layers vi and vii. c) The 3D view of microfluidic chip is denoted. d) Side-view of microfluidic chip is displayed..... 31

Figure 3.1. Contact angle analysis for before (bare versions) and after silk coating to a) glass, b) PMMA, and c) polystyrene surfaces. d) Contact angle changes are presented quantitatively for each surface. 40

Figure 3.2. FTIR analysis for before (bare versions) and after silk coating to a) glass, b) PMMA, and c) polystyrene surfaces..... 41

Figure 3.3. XPS characterization. C1s scans are presented for a) bare and b) SF-coated glass surface. N1s scan are shown for c) bare and d) SF-coated glass surface. For PMMA surfaces, C1s scans are represented for e) bare and f) SF-coated PMMA surfaces. N1s scans are shown for g) bare and h) SF-coated PMMA surfaces. For bare and SF coated PMMA surfaces. For polystyrene surfaces, C1s scans are presented for i) bare and j) SF-coated glass surface. N1s scan are shown for k) bare and l) SF-coated glass surface. 43

Figure 3.4. Microscopic images of MCF-7 cells cultured in static2D, static3D, and dynamic conditions. Brightfield images show monolayer of MCF-7 cells growing in (a) static2D conditions (Scale bar: 200 µm). (b) Cell images are taken under static3D conditions (Scale bar: 100 µm). (c) Cell images are collected under dynamic conditions (Scale bar: 500 µm). Hoechst 33342-stained cells are presented in d) static2D conditions (Scale bar: 20 µm). (e) Likewise, cells are imaged under static3D conditions (Scale bar: 50 µm). (c) Cell images are collected for dynamic conditions (Scale bar: 500 µm). 44

Figure 3.5. a) RNA mass/cell plot was obtained from cells cultured under three different conditions. b) Average of RNA mass/cell values were presented for static2D, static3D, and dynamic conditions. 47

Figure 3.6. Gel images for cDNAs (CK-18, EpCAM, and GAPDH genes) collected from static2D, static3D, and dynamic conditions were presented..... 48

Figure 3.7. Analysis of the expression levels of EpCAM and CK-18 genes under different conditions by qRT-PCR (GAPDH gene is used as an endogenous control). 50

Figure 4.1. Doxorubicin treatment results for static2D condition are presented. a) The number of live/dead cells for control group and four different doses at the end of the experiment are demonstrated. b) The viability rate is obtained for control group, 0.1 nM, 10 nM, 10^3 nM, and 10^5 nM of doxorubicin. 52

Figure 4.2. Static2D images of control group and cells treated with 0.1 nM, 10 nM, 10^3 nM, and 10^5 nM of doxorubicin under brightfield and fluorescent as a result of live/dead assay. 54

Figure 4.3. Doxorubicin treatment results for static3D condition are presented. a) The live/dead cells number for all experimental groups is shown. b) The viability percentages for control group and each dose are plotted. 55

Figure 4.4. Brightfield images of static3D condition show control group and cells treated with 0.1 nM, 10 nM, 10^3 nM, and 10^5 nM of doxorubicin and fluorescent as a result of live/dead assay..... 56

Figure 4.5. The effects of doxorubicin on dynamic condition are presented. a) The live/dead cells number for all experimental groups is shown. b) The viability percentages for control group and each dose are plotted. 57

Figure 4.6. Brightfield images and live/dead assay result of control group and cells treated with 0.1 nM, 10 nM, 10^3 nM, and 10^5 nM of doxorubicin obtained from dynamic conditions..... 58

Figure 4.7. Combined cell viability rate plot from static2D, static3D and dynamic conditions for doxorubicin treatment. 59

Figure 4.8. Gel images for cDNAs (MDR-1, BCRP and GAPDH genes) collected from static2D, static3D and dynamic conditions. 61

Figure 4.9. The effects of docetaxel on static2D condition are presented. a) The live/dead cells number for all experimental groups is shown. b) The viability percentages for control group and each dose are plotted. 62

Figure 4.10. Images of control group and cells treated with 0.1 nM, 10 nM, 10^3 nM, and 10^5 nM doses of docetaxel are demonstrated under brightfield and fluorescence imaging as a result of live/dead assay for static2D condition..... 63

Figure 4.11. The effects of docetaxel on static3D condition are presented. a) The live/dead cells number for all experimental groups is shown. b) The viability percentages for control group and each dose are plotted. 64

Figure 4.12 Images of control group and cells treated with 0.1 nM, 10 nM, 10^3 nM, and 10^5 nM doses of docetaxel are demonstrated under brightfield and fluorescence imaging as a result of live/dead assay for static3D condition..... 65

Figure 4.13. The effects of docetaxel on dynamic condition are presented. a) The live/dead cells number for all experimental groups is shown. b) The viability percentages for control group and each dose are plotted. 66

Figure 4.14. Images of control group and cells treated with 0.1 nM, 10 nM, 10^3 nM, and 10^5 nM doses of docetaxel are demonstrated under brightfield and fluorescence imaging as a result of live/dead assay for dynamic condition..... 67

Figure 4.15. Combined cell viability rate plot from static2D, static3D and dynamic conditions for docetaxel treatment. 68

Figure 4.16 Gel images for cDNAs (MDR-1, BCRP and GAPDH genes) collected from static2D, static3D and dynamic conditions. 69

Figure 4.17 Gene expression analysis for CK-18, EpCAM, MDR-1, and BCRP is demonstrated on the course of doxorubicin treatment. 72

Figure 4.18 Gene expression analysis for CK-18, EpCAM, MDR-1, and BCRP is demonstrated on the course of docetaxel treatment. 73

Figure 5.1. NTA analysis of EVs isolated from static2D, static3D and dynamic conditions. Evaluating the results of EVs isolated from a-d) static2D, e-f) static3D conditions, and i-l) dynamic conditions (n=4). 77

Figure 5.2. Investigating the effects of different culture conditions (static2D, static3D, and dynamic) on size and concentration of EVs. For statistical assessments, we performed an ordinary one-way ANOVA test ($n=3$, $p<0.05$). Asterisk demonstrates statistical difference between the groups. 78

Figure 5.3 NTA analysis for control non-treated) and doxorubicin (0.1 nM, 10 nM, 10^3 nM and 10^5 nM doses) administered cells under static2D condition (n=3) 80

Figure 5.4. Investigating the effects of doxorubicin on size and concentration of EVs collected from Static2D conditions. a) Mean values, b) mode values, and c) EV concentrations are presented. For statistical assessments, we performed an ordinary one-way ANOVA test, and there was no statistical differences observed between the groups (n=3, p>0.05).. 81

Figure 5.5. Size and concentration of EVs collected from doxorubicin treated Static3D conditions (n=3) 83

Figure 5.6. Investigating the effects of doxorubicin on size and concentration of EVs collected from static3D conditions. a) Mean values, b) mode values, and c) EV concentrations are presented. For statistical assessments, we performed an ordinary one-way ANOVA test (n=3, p<0.05). Asterisk demonstrates statistical difference between the groups. 84

Figure 5.7. NTA analysis for control (non-treated) and doxorubicin (0.1 nM, 10 nM, 10^3 nM and 10^5 nM doses) administered cells under dynamic condition (n=3). 86

Figure 5.8. Investigating the effects of doxorubicin on size and concentration of EVs collected from dynamic conditions. a) Mean values, b) mode values, and c) EV concentrations are presented. For statistical assessments, we performed an ordinary one-way ANOVA test, and there was no statistical differences observed between the groups (n=3, p>0.05). 87

Figure 5.9. Comparing a) mean values, b) mode values, and c) EV concentrations of static2D, static3D and dynamic conditions on the course of doxorubucin. For statistical assessments, we performed two-way ANOVA test (n=3). Statistical differences were

*examined comprehensively in the analysis. * represents p<0.05, ** shows p<0.005, and *** states p<0.0005. ..... 88*

Figure 5.10. NTA analysis for control (non-treated) and docetexal (0.1 nM, 10 nM, 10^3 nM and 10^5 nM doses) administered cells under static2D condition (n=3). 90

Figure 5.11. Investigating the effects of docetaxel on size and concentration of EVs collected from static2D conditions. a) Mean values, b) mode values, and c) EV concentrations are presented. For statistical assessments, we performed an ordinary one-way ANOVA test, and there was no statistical differences observed between the groups (n=3, p>0.05). 91

Figure 5.12. NTA analysis for control (non-treated) and docetexal (0.1 nM, 10 nM, 10^3 nM and 10^5 nM doses) administered cells under static3D condition (n=3) 92

Figure 5.13. Investigating the effects of docetaxel on size and concentration of EVs collected from static3D conditions. a) Mean values, b) mode values, and c) EV concentrations are presented. For statistical assessments, we performed an ordinary one-way ANOVA test, and there was no statistical differences observed between the groups (n=3, p>0.05). 93

Figure 5.14. NTA analysis for control (non-treated) and docetexal (0.1 nM, 10 nM, 10^3 nM and 10^5 nM doses) administered cells under dynamic condition (n=3) 94

Figure 5.15. Investigating the effects of docetaxel size and concentration of EVs collected from dynamic conditions. a) Mean values, b) mode values, and c) EV concentrations are presented. For statistical assessments, we performed an ordinary one-way ANOVA test (n=3, p<0.05). Asterisk demonstrates statistical difference between the groups. 95

Figure 5.16. Comparing a) mean values, b) mode values, and c) EV concentrations of static2D, static3D and dynamic conditions on the course of docetaxel. For statistical assessments, we performed two-way ANOVA test (n=3). Statsitical differences were

*examined comprehensively in the analysis. * represents p<0.05 and ** states p<0.005.* *96*

Figure 5.17. SEM image of EVs isolated from a) static2D, b) static3D, and c) dynamic conditions..... *97*

Figure 5.18. SEM images and size information of EVs from three different conditions treated with varying concentrations of doxorubicin..... *98*

Figure 5.19. SEM images and size information of EVs from three different conditions treated with varying concentrations of docetaxel..... *99*

Figure 5.20. Western Blot analysis of static2D, static3D, and dynamic conditions for a) CD63 protein and b) CD81 protein..... *100*

Figure 5.21 Western Blot analysis of a) CD63 protein and b) CD81 protein for EVs isolated from doxorubicin treated cells from static2D, static3D and dynamic conditions. *101*

Figure 5.22 Western Blot analysis of a) CD63 protein and b) CD81 protein for EVs isolated from docetaxel treated cells from static2D, static3D and dynamic conditions. *101*

List of Tables

Table 1.Comparison between 2D and 3D cell culture 12

Table 2.Cell counts at the beginning and end of the experiment and RNA Mass values of cells grown in static2D, static3D and dynamic conditions. 46

Table 3. cDNA concentrations of Static2D, Static3D and Dynamic conditions were measured by Qubit Fluorometer..... 47

Table 4.RNA concentrations of Doxorubicin (Dox) treated cells. 60

Table 5.RNA concentrations of Docetaxel (Doc) treated cells. 69

CHAPTER 1

1.INTRODUCTION

1.1 Cancer

Cancer is a disease that causes certain cells in body to proliferate in an uncontrolled manner. Cancer, however, is an overwhelming challenge globally. Per the result of a study conducted by the International Agency for Research on Cancer, there would be around 19.3 million new cancer diagnosis and 10 million died from the cancer in 2020, with data from 185 countries [1]. Since cancer can arise from almost every type of cell, there are many more than a dozen different cancer subtypes such as breast, lung, liver, pancreas, and stomach. Particularly, in women, with an estimated 2.3 million new cases (11.7%), female breast cancer had overtaken lung cancer (11.4%) as being the most frequently diagnosed cancer type [1].

There are many different hallmarks of cancer, which are complicated and varied, and scientists and medical researchers continue to study and comprehend them (Figure 1.1.). However, recognizing these features of cancer is crucial for the development of effective treatments and the improvement of cancer patients' survival rates. One of the hallmarks of cancer is uncontrolled cell division [2]. Regarding growth and division, normal cells in the body obey to a rigid set of regulations. They usually divide when the body requires self-repair or the replacement of old or damaged cells [3]. Nonetheless, cancer cells do not obey to these criteria. The capacity of cancer cells to resist the body's inherent defenses is a second defining characteristic of cancer [2]. The immune system is initial defense against foreign intruders and infections. For most instances, immune system is able to identify and eliminate cancer cells before they may cause damage.

Unfortunately, these cells begin to escape the immune system by disguising itself as healthy cells or by establishing a hostile environment enough to prevent the immune system from destroying them. In this trajectory, cancer cells are resistant to apoptosis (programmed cell death), allowing them to survive and continue to grow, and they have the ability to divide indefinitely, allowing them to outcompete normal cells and accumulate mutations that further drive cancer growth [4].

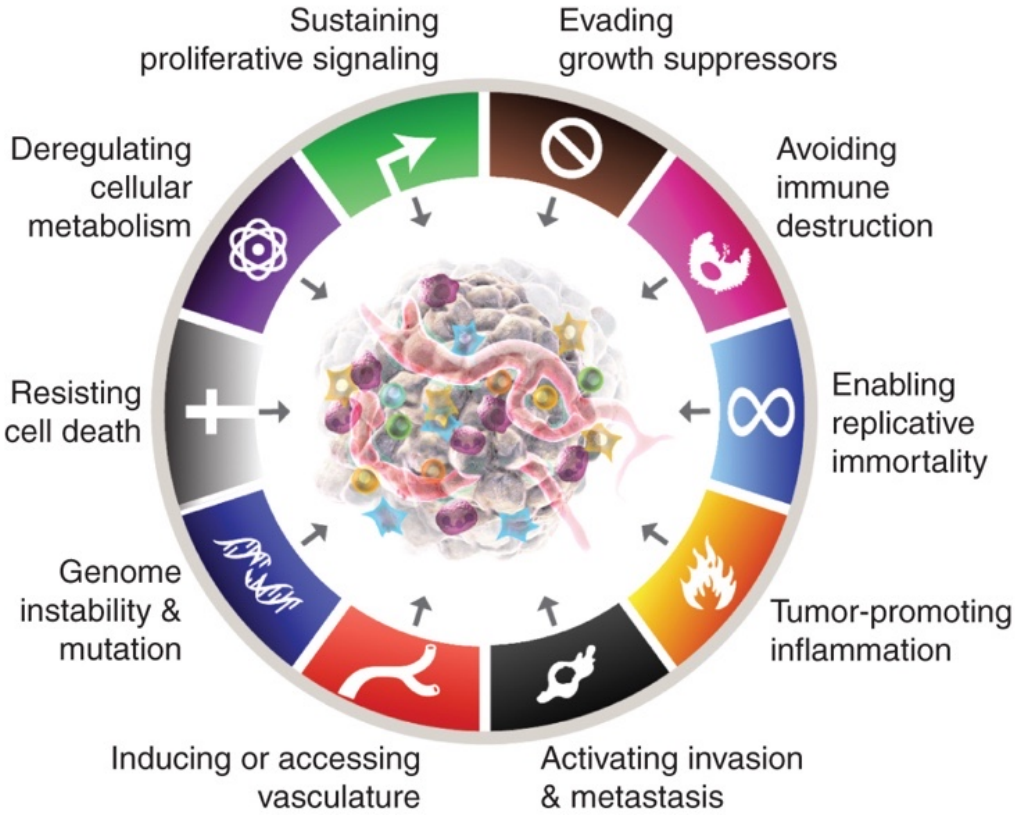


Figure 1.1. This illustration shows ten important hallmarks of cancer cells. Reproduced from [5].

The initial step while diagnosing and treating cancer is to determine whether tumor is benign or malignant [6]. Benign tumors basically do not invade neighboring normal tissues. One of the hallmarks of being cancerous is the ability of cells to penetrate basement membrane surrounding a particular tissue [7]. Since cells in benign tumors cannot penetrate the basement membrane to spread into surrounding tissues, these tumor cells are not cancerous. Usually, benign tumors can be easily eliminated with surgery,

and they may sometimes require additional treatments such as radiation therapy or chemotherapy. Some benign tumors do not require any treatment as they do not pose a health risk. Malignant tumors, on the other hand, refer to tumors that can proliferate quickly and invade nearby tissues through the blood or lymphatic system [8]. This process is called metastasis—another hallmark of cancer. It can be developed in any organ, including the breast, lungs, and lymph nodes [9]. If cancer is not diagnosed and treated early, it might spread to other regions of the body, where secondary tumors can grow [10]. Moreover, malignant tumors may need chemotherapy, radiation therapy, or immunotherapeutic treatments to eridicate any remaining cancer cells or to treat secondary tumors in other parts of the body [9]. In addition, there are differences between benign and malignant tumors, such as growth rate, recurrence, invasion ability, treatment, and morphology [8]. In general, malignant tumors have a higher growth rate than benign tumors. As benign tumors have distinct borders, they are more suitable for surgical removal and less prone to recur [11]. If they do arise again, it is solely in the initial location. However, malignant tumors can metastasize to different areas of the body. Such events are more likely to reoccur.

Considering the reasons behind this, we mostly realize that mutations are crucial driving forces in cancer development. Typically, millions of mutations occur daily in DNA in body cells. Thanks to repair mechanisms during the evolution for 3.5 billion years, DNA repairs itself [12]. However, since human body does not function perfectly, and there is a possibility of statistical errors in biochemical reactions, sometimes these mutations cannot be repaired or they are overlooked by the repair mechanisms [13], and such situations have considerable potential to develop cancer. Although specific causes of cancer are not entirely understood, there have been defined a variety of possible risk factors. These include exposure to smoking, asbestos, radiation, and some infections [14], [15]. A family history of cancer, some inherited genetic abnormalities, and certain lifestyle variables, such as being overweight or obese are additional risk factors for cancer [16].

Chemotherapy is defined as systematic drug treatment applied to stop or slow down the growth of cancer cells [17]. Chemotherapy, which can sometimes be applied together with surgical procedures and radiotherapy, constitutes of different strategies depending on some factors, such as the type of cancer and the purpose of treatment [18].

Some chemotherapy drugs, for instance, directly target the tumor, while the others indirectly aim to eradicate the tumor by strengthening the immune system. The majority of people, who take chemotherapy experience serious side effects. The primary cause of these adverse effects is the failure of supplied medications to selectively target cancer cells. Instead, most medications target quickly replicating cells. Certainly, cancer cells are an example of fast-growing cells; yet, non-target cells such as hair follicles can also be cited [19]. Every day, new research is made to develop chemotherapy treatments that are more efficient and safer. However, neither the paucity of specificity nor negative side effects of these medications are main concerns to be encountered. The resistance of cells to given chemotherapy medications through a variety of processes, known as chemotherapy resistance, decreases the likelihood that treatments will be effective [20]. Therefore, understanding the grounds of resistance is crucial in creating more effective medications (Figure 1.2.).

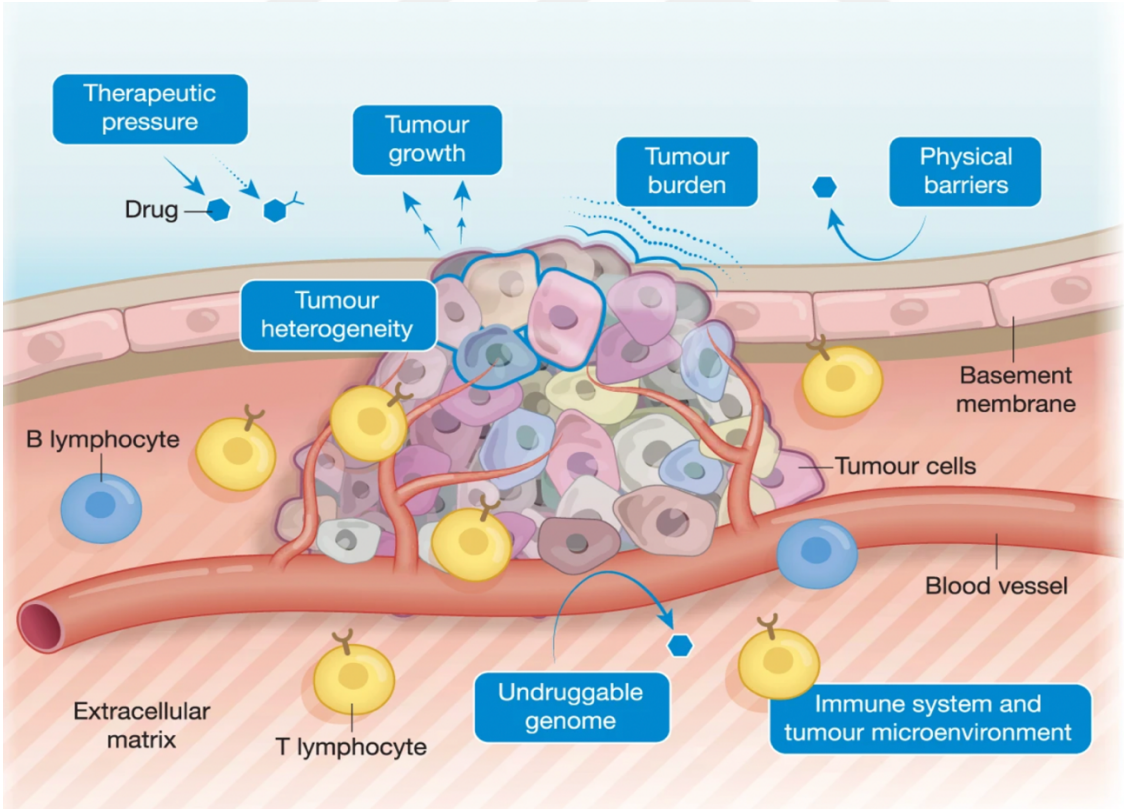


Figure 1.2. A representative image for biological variables that influence drug resistance. Tumors constitute of heterogeneous structure, and they are surrounded by a

microenvironment comprised of membrane, capillaries, immune cells, and cancer ecology. Changes in the physical traits, genetic makeup, and environmental factors of the tumor build drug resistance. Reproduced from [21].

1.2 Microfluidics Chip Approach in Cancer Studies

Microfluidic chips are the devices used to manipulate and control fluids, and they enable to control microliters and smaller volumes of fluid through the movement within micro-scale channels [22]. In microfluidics, volumes on the order of microliters are processed in channels of between 1 μm and 1000 μm in size [23]. The characteristics of laminar flow on these systems allows precise regulation of molecular concentrations [23]. During the early 1990s, microfluidics was first used as a biological device [24]. Since that day, cross-disciplinary technology has progressed significantly, earning a reputation for its ability to manipulate substances inside nanoscale platforms.

The fabrication of microfluidic chips requires an essential attention to be implement into a biological manner. There are numerous ways to produce these chips, each with its own benefits and drawbacks [25]. Soft lithography, for instance, is one of the most used techniques for manufacturing microfluidic chips that uses a flexible substance, such as a polymer, to generate microfluidic channels and structures [26]. The polymer is first shaped with a mold or stencil, then cured with heat or ultraviolet radiation [27]. This approach enables the fabrication of complicated three-dimensional structures, is very affordable, and is simple to employ. Photolithography is another technique for fabricating microfluidic chips. This method involves using light to pattern a photosensitive material, such as a photoresist SU-8, on a substrate [28]. The photoresist is then developed to create a patterned mask, which is used to etch the desired channels and structures into the substrate [29]. Photolithography has several advantages, including high resolution and the ability to create complex structures. However, it can be expensive and time-consuming, and it is not suitable for high-volume production [30]. Micromachining is the third technology for the manufacturing. Using a number of tools and procedures, microfluidic channels and structures are cut, drilled or etched onto a substrate using this method [26], [31]. Using a concentrated ion beam, micromachining may be used, for instance, to form channels in a silicon wafer or to drill holes in a glass

substrate. This method permits the production of extremely tiny and intricate structures, but it can be costly and difficult to regulate. Another commonly used method for fabricating microfluidic chips is micro-molding. This method involves using a mold to create the desired structures in a polymer material, such as PDMS (polydimethylsiloxane). The mold is typically made using photolithography or another method, and it is employed to create channels and structures in a polymeric material. Micro-molding has several advantages, such as low cost and high throughput. It is also relatively easy to scale-up for high-volume production. However, it is not as precise as photolithography, and it can be difficult to create complex structures. Lastly, microfluidics may also be manufactured utilizing 3D printing techniques. This requires the use of a specialized printer capable of printing materials with extremely fine resolution, such as polymers and metals. Typically, the printer is computer-controlled, allowing for the precise fabrication of complicated 3D structures. 3D printing permits the construction of customized structures.

In recent years, microfluidic chips, which were first produced using glass and silicon, have begun to be produced with elastomers that have higher biocompatibility and are inexpensive. In this way, its use in biological studies has increased [23]. In addition, many advantages of microfluidic chips such as low sample volume requirement, flexibility, high sensitivity, low number of cells, parallelization, less reagent consumption, automation, short processing time and real-time analysis make these devices important for biological studies [32] (Figure 1.3.). In this direction, biological applications in which microfluidic chips were first used in studies conducted are polymerase chain reaction (PCR), DNA microarrays, and electrophoresis on-chip [24]. During the last few decades, biosensor platforms, single-cell screenings for disease prognosis and diagnosis, cell culture, point-of-care (POC) systems, drug release studies and other practices have all benefited from microfluidics systems for controlling proteins, RNA, and mammalian cells [33]–[35]. Even the abundance of these systems, integration of microfluidic chips into cancer research can be approached in new ways [36].

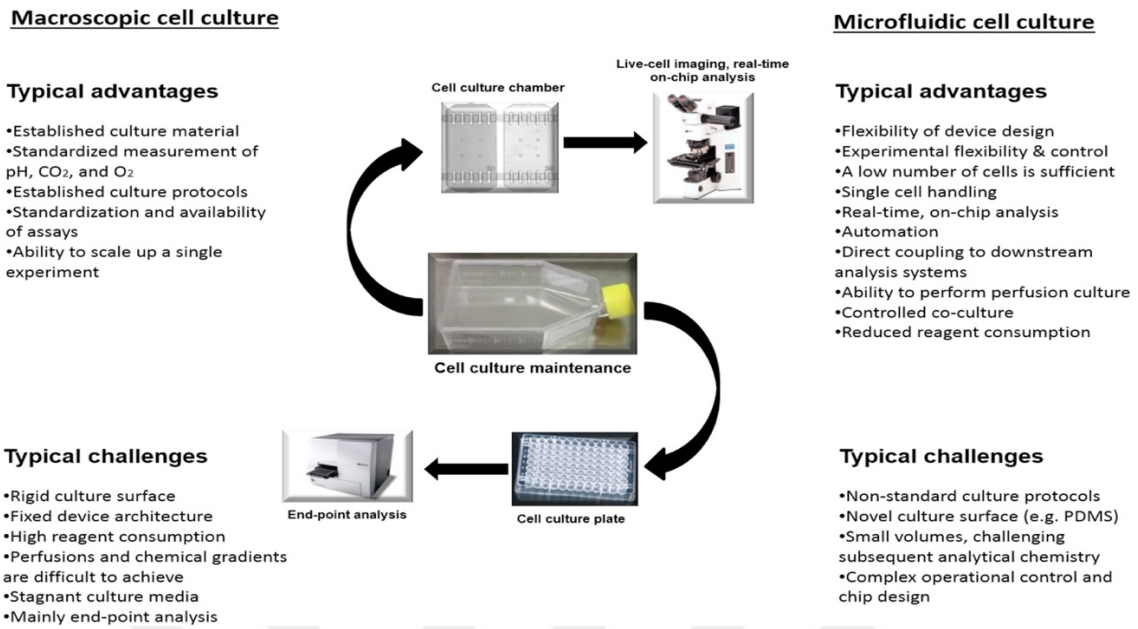


Figure 1.3. Advantages and disadvantages of cell culture methods performed on microfluidic chips and conventional method. Reproduced from [32].

For a long time, cancer research has been among the primary concerns of medical and scientific communities. Cancer has been a prominent and quite well subject of study for decades due to its supposedly incurable characteristics and widespread occurrence in society [36]. In the United States, about 2 million new cancer-related cases and 610.000 from cancer are expected in 2022 [37]. Lung cancer will cost the lives of nearly 350 people every day [37]. A large economy has been utilized on research and development since 2004 in the hopes of finding better ways to fight cancer through the use of technology [38]. Over 15 million Americans have indeed been diagnosed as having cancer, and that number is predicted to rise to more than 19 million by 2024, placing a significant financial strain on the nation of much more than 130 billion dollars annually [39], [40]. In order to increase the number of people, who survive cancer, screening programs, early detection methods, and drugs that are shown to work need to be more widely available and financially feasible. Specimens of tumor tissue or indirect protein measurement have always played a pivotal role in cancer diagnosis. These traditional sampling methods are generally invasive, which results in tissue injury, restricted access, and difficulty in getting accurate samples, as well as significant patient pain [41]. Cancer biomarkers in bodily secretions like blood and saliva have been found

through proteomic and genomic analysis [42],; yet, POC tools for these assays are still insufficient, making it difficult to provide quick, non-invasive diagnoses. Because of its natural capability for evaluating complex fluids *in vitro*, microfluidic chips provide a solution for cancer detection, understanding metastasis, and tumor-on-a-chip studies (Figure 1.4). Circulating tumor cells (CTCs), microRNA, proteins, vesicles, and DNA are all examples of potential biomarkers from blood [43], [44]. The challenge is that cancer biomarkers are typically detectable only at very low levels amidst overwhelming background signals. For instance, in 1 ml of total blood comprising 10^6-10^7 cells [45], there are only 1-10 CTCs, and the proportion of specific proteins to the background is about $1{:}10^5$ [46]. The difficulty of detecting the signal due to enormous background has led researchers to focus on solutions based on MEMs (microelectromechanical systems). Because microfluidic chips can perform high-precision separation in small volumes, they have become frequently utilized in these solutions. Biomarkers can be evaluated quite often with the required sensitivity, and this is becoming one of the potential ways to create personalized treatment due to the low expense and simplicity of production of microfluidic devices [47].

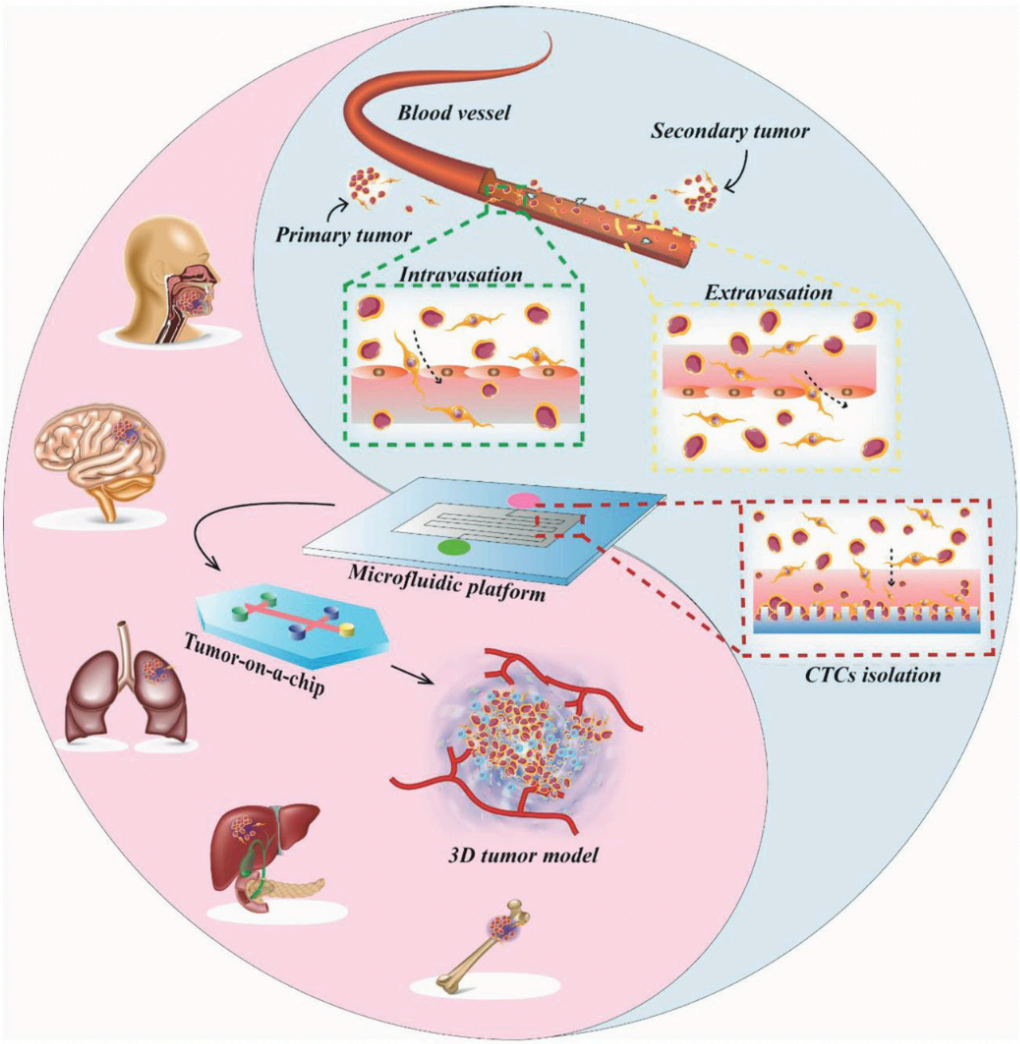


Figure 1.4. The use of microfluidic systems in cancer studies. Microfluidic chips offer pivotal advances in isolating circulating tumor cells (CTCs), understanding metastasis, and generating 3D tumor models and tumor-on-a-chip studies. Reproduced from [48].

Prior to cancer diagnosis, understanding the biology of cancer is essential. The potential for microfluidic chips to improve and leverage our understanding of disease origins and act as therapeutic tools for testing and screening the effectiveness of drugs and treatments is promising [49]. Briefly, in practice, cancer cells are often cultured in standard tissue culture plates or flasks as *in vitro* tests. These simplified models are easy to implement, but they do not accurately reflect biological and mechanochemical intricacy of typical tumor microenvironment (TME). In these experimental models, the response of cells to a specific drug given systemically differs from native condition. After

a plenty of time and resources have been spent on developing a single drug, it may be abandoned. Likewise, *in vivo* testing provides real conditions as a disease model offering the required biological intricacy that is lacking in traditional *in vitro* models; however, it takes huge efforts, time, and expensive instrumentation [50]. For the purpose of making reliable predictions of drug reactions in clinical studies on humans, this is of special interest. Furthermore, exact components and cells of the TME that promote cancer growth and metastasis cannot be identified using this model. Ultimately, more sophisticated *in vitro* models of cancer are required, which more accurately represent both normal and malignant tissue, as well as their interactions with external milieu. This involves simulating fluid flow, biochemical/mechanical signals, and tissue-to-tissue interactions that both healthy and malignant cells encounter in tissue and organs. Microfluidic systems have recently been recognized as potentially useful complements for the study of cancer [51].

1.3 2D and 3D Cell Culture

In vitro cell culture studies consists the major steps in proliferation or differentiation of cells that are obtained from a source under appropriate controlled conditions. Cell cultures were first used in 1907, in the work of Ross Harrison [52]. The basis of these studies is to enable cells with reproductive ability to grow by keeping them in a controlled *in vitro* environment that mimics physiological assets. If cell growth is expanded on a planar surface *in vitro*, this is called 2D cell culture. Cells usually proliferate by adhering to the material from which these containers are produced, thus obtaining a 2D layer-shaped cell assembly. In a 2D culture system, cells are grown in a single layer on a plastic surface, such as a culture flask or petri dish. This method is convenient and cost-effective for maintaining and testing cell cultures; yet, it does not accurately recapitulate complex 3D structure of native tissues or tumors. [53]. This culture technique does not adequately imitate interactions between intracellular and extracellular surroundings that occur within a tumor. [54]. Interactions between intracellular and extracellular environments play a crucial role in regulating various cellular functions, including differentiation, viability, expression, stimuli response,

proliferation, and drug metabolism. However, when cells are grown in a 2D culture system, they are not exposed to the same interactions as they would be in a natural environment, which can alter their behavior and response to processes like apoptosis. This loss of polarity can be caused by cell adherence to a flat surface. [55]. In a 2D culture system, cells are grown in a single layer and have unrestricted access to components of the culture medium, including oxygen, nutrients, signaling molecules, and other metabolic products. This can potentially lead to a distorted representation of the natural environment and limit the accuracy of the results obtained from this method. [56]. Furthermore, 2D culture systems often consist of monocultures, meaning that only one type of cell is present. This can result in a scarcity of the diverse microenvironment or niches that are present within a tumor *in vivo* and are required for cancer-initiating cells. [57]. Due to the numerous drawbacks of 2D systems, there is a requirement for possible alternatives, such as 3D culture systems, that can replicate a natural tumor mass. The term "3D cell culture" refers to an environment that has been intentionally built such that biological cells can develop in all three dimensions. In the 1970s, Hamburg and Salmon created the first earliest 3D cultures in a soft agar medium [58]. Ever since strong parallels between shape and behavior of cells in a primary tumor and cells cultivated under 3D circumstances have been carefully characterized and reported [59]. The 3D cell culture, as opposed to 2D counterparts, demonstrates the development of cells in their natural environment *in vitro* [60]. For years, researchers have utilized 3D cell cultures. In drug development, the capacity of an *in vitro* test to yield biomedically valid data is mainstay [61]. It has been suggested that utilizing of 3D *in vitro* systems in drug research and development, the detection of novel biomarkers, and the comprehension of cancer biology would have great potential to serve as a possible connection, thereby fulfilling the existing gaps between 2D cell culture and animal model experiments [62].

Table 1.Comparison between 2D and 3D cell culture

Cell culture methods	*2D Cell culture*	*3D cell culture*	*Ref.*
Cost	Cost-effective	Expensive	[58], [63], [64]
Cell shape	Alterations in shape and the form of division. The disappearance of phenotypic variation and polarity	Polarity and a wide variety of phenotypes have been maintained along with the preserved morphology and the form of division	[64], [65]
Time required for culture	In minutes to several hours	A few hours to several days.	[66]–[68]
Accessibility to critical substances	Oxygen, metabolites, signaling molecules, and nutrition, are unlimited (unlike *in vivo*)	Oxygen, metabolites, signaling molecules, and nutrients, have varying degrees of accessibility (similar to *in vivo*)	[56], [69]
Level of expression	Relative to *in vivo* models, gene and protein expression levels are different	Expression levels of genes and protein largely match values obtained from *in vivo* models	[55], [60]–[62]
Interaction of cells	Poor cell-cell and cell-extracellular matrix interactions, niches or *in vivo*-like surroundings	Effective cell-cell and cell-extracellular matrix interactions, and proper niches	[57], [70]
Analysis and utility	High performance, repeatability, longevity, interpretability, and simplicity of culture	Poor repeatability, difficult to analyze, and executing cultures are more complex	[58], [71]

There are a variety of biomaterials suitable for 3D cell culturing, including natural and synthetic materials. Natural biomaterials include extracellular matrix proteins such as collagen, silk fibroin, alginate, and hyaluronic acid, which can be extracted from both animal and plant sources and used to create a scaffold for cells to attach and grow [72]. Synthetic biomaterials include polymeric materials such as polyethylene glycol and polycaprolactone, which can be tailored to have specific properties such as biocompatibility and biodegradability. One challenge with using biomaterials for 3D cell culture is ensuring that the material supports attachment and growth of cells without interfering with their function. This requires careful selection and optimization of the biomaterial, as well as the use of techniques such as surface modification to improve the material's biocompatibility.

In particular, natural stemmed materials are crucial elements in constructing 3D cultures. For instance, silk fibroin (SF) is a protein that is extracted from silkworms and has been employed in various applications in the fields of tissue engineering and three-dimensional (3D) cell cultures [73]. It is a biocompatible and biodegradable material that has several attractive properties for use in these applications. One of the key benefits of using SF in 3D cell culture is its ability to form a strong and flexible scaffold or matrix for supporting growth and development of cells [74]. The protein can be processed into a gel-like consistency and then molded into the desired shape, allowing for generating complex, 3D structures that imitate native environment of cells in the body. Additionally, SF has been shown to have a low toxicity profile, making it safe for use in cell culture [75]. It is also highly hydrophilic, and therefore, it can absorb and retain large amounts of water, which is essential for maintaining the cells in a healthy and viable state [76]. Another advantage of SF is its mechanical strength, making it resistant to tearing and other forms of mechanical damage [74]. This is important for supporting the growth of cells and preventing them from being damaged or disrupted during the culturing process. In addition, researchers have realized that SF has ability to promote adhesion and proliferation of several cell types [77], making it a multipurpose material suitable for a number of tissue engineering and 3D cell culture applications. Overall, SF holds an enormous potential material to be utilized in 3D cell culture due to its biocompatibility, mechanical strength, biodegradability, and capacity to facilitate the development of numerous cell types. Although further study is required to fully comprehend its

significance in tissue engineering and other purposes, it has demonstrated considerable promise as a tool for promoting the growth and development of cells in a 3D milieu.

1.4 Extracellular Vesicles (EVs) as a Biomarker for Cancer

Prior to recent years, scientific community primarily considered that extracellular vesicles (EVs) were a kind of cell debris, hence they were named as “cell dust”. By leveraging recent advances and discoveries in cancer research especially, it is now known that EVs serve other vital functions. For instance, intercellular communication is facilitated by extracellular vesicles [78]. EVs also provide tasks such as immune response modulation. According to their intracellular origin, there are three distinct kinds of EV [79]. (i) Apoptotic Bodies include cellular biomolecules such as deoxyribonucleic acid (DNA), ribonucleic acid (RNA), and small proteins, and they are varying in size from 500 nm to 2000 nm [80]. Apoptotic bodies deliver their contents to macrophages, which perform cell engulfment, on the course of apoptosis [81]. (ii) Microvesicles are also referred as ectosomes, microparticles, and vesicles generated from plasma membranes. By budding outward and fragmenting plasma membranes, microvesicles ranging in size from 100 to 1000 nm are generated [82]. Once microvesicles are produced, they transmit certain proteins and lipids to the selected destination cell. (iii) Exosomes are distinguished from other EVs by their intracellular origin and size [83]. The diameters of exosomes vary between 30-150 nm [84] They are small, naturally occurring vesicles that are produced by cells into the extracellular environment. These vesicles, which are enclosed by a double-layered phospholipid membrane, contain many lipids, proteins, and several nucleic acid types and variants, including mRNAs (messenger RNA), miRNAs (micro RNA), circular RNA, lncRNAs (long non-coding RNA), and DNA fragments [85] (Figure 1.5.). They are produced by nearly all bodily cells [86]. Exosomes have a crucial role in several biological activities, including intercellular communication, transfer of genetic material, signal transmission, and control of the immune system [87], [88]. The

ability of exosomes to separate from all body fluids such as blood, urine, sweat, and so on enables the development of non-invasive and effective diagnostic strategy [89].

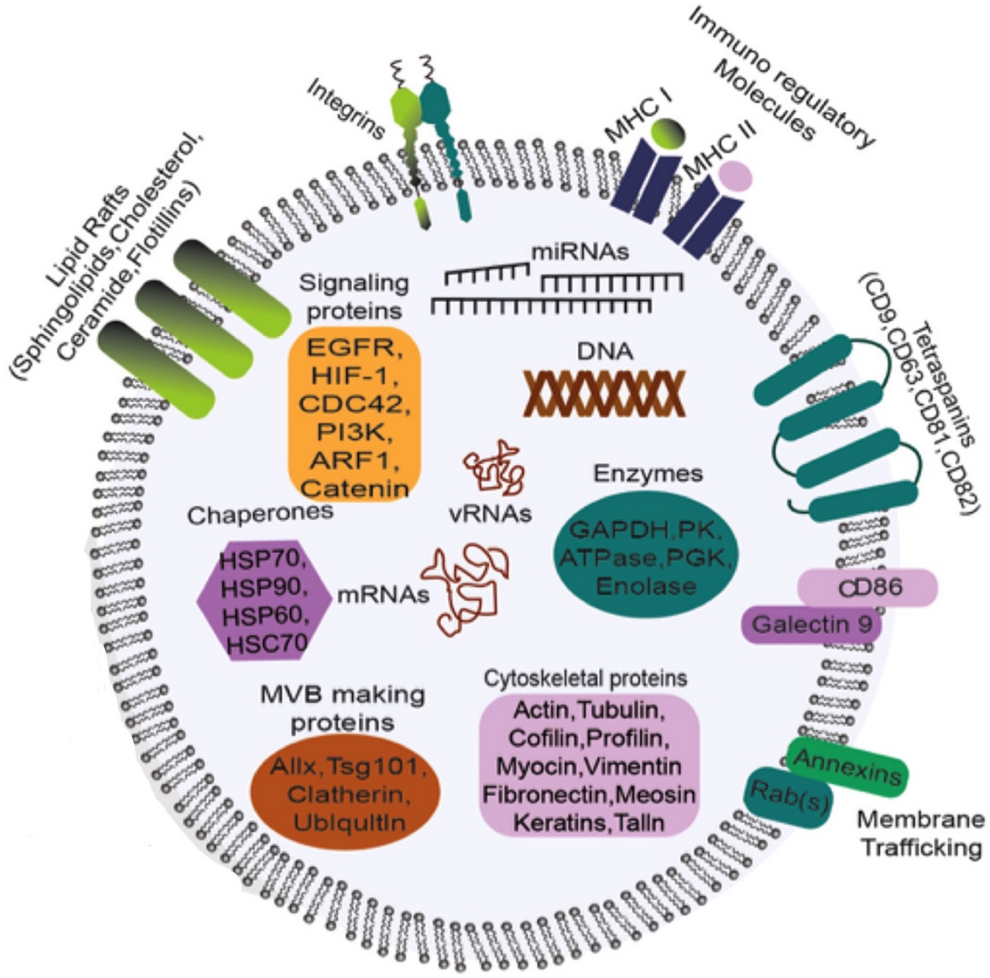


Figure 1.5. Elements of exosomes discovered in various proteome analyses and their distinct cellular material are depicted. Reproduced from [90].

Now scientists know all the different assets that exosomes have roles, they are studying how they could be used as a biomarker to improve current diagnostic strategies in cancer and track its progress. Most of the time, primary cancers can be eradicated with surgery and additional treatment. However, metastatic cancers are difficult to completely get rid of, and they account for roughly 90% of cancer-related deaths. Increasing number of evidence has showed that exosomes and their contents help create the microenvironment before the spreading of cancer [91]. Extracellular vesicles can promote tumor cell metastasis and invasion, promoting the local and distant spread of tumor cells (Figure 1.6.). Prior to the formation of metastatic tumors by actual metastatic cells, these

tissue locations are recognized as metastatic anterior foci by substances secreted by original tumors [92]. Recent research indicates that tumor-derived EVs interact with normal host cells in the metastatic zone, resulting in the development of metastatic foci [91]. This aids to the comprehension of the non-random occurrence of metastatic structures. Angiogenesis—the development of new blood vessel, governs nutrition availability of solid tumors with rapid growth. Exosomes influence cancer metastasis due to their ability to stimulate tumor angiogenesis [93].

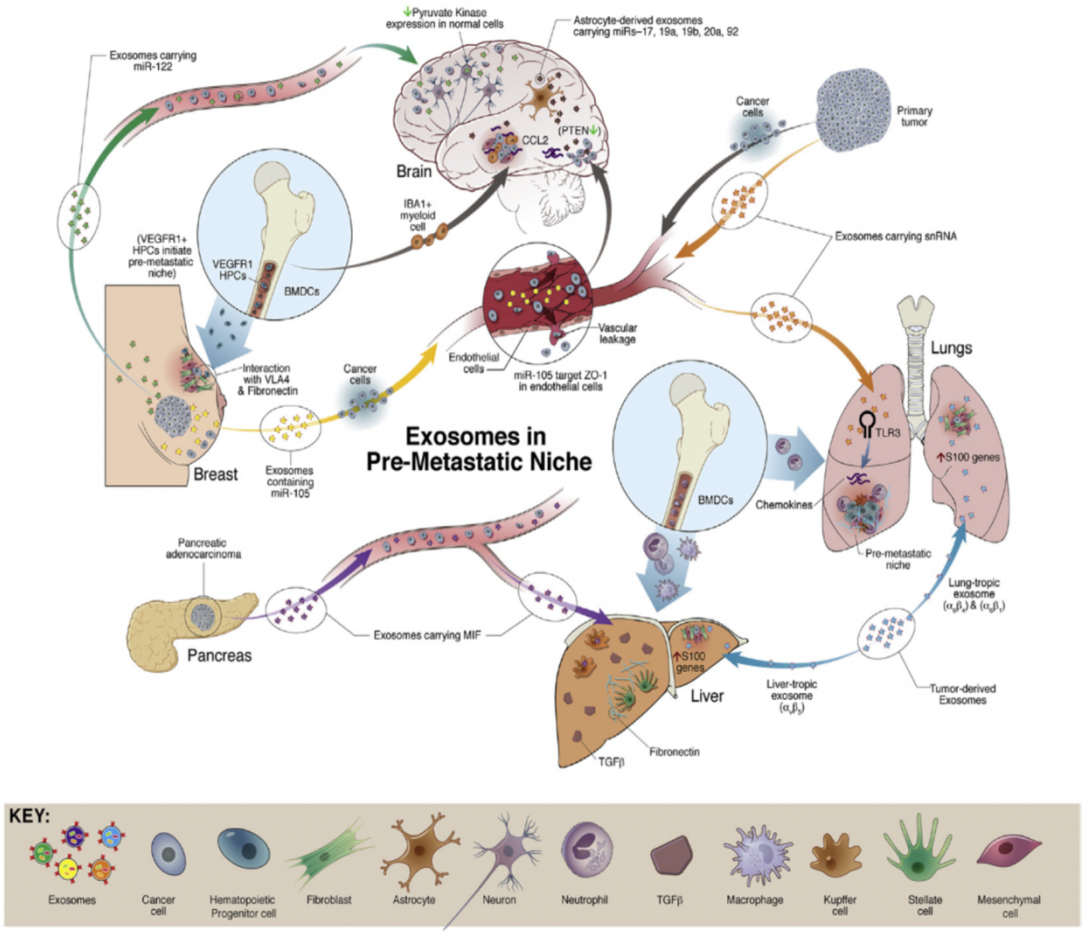


Figure 1.6. Exosomes and the establishment of pre-metastatic niches. The initial cancer cells release exosomes into the extracellular environment. The distribution and targeted organotrophic incorporation of these vesicles carrying oncoproteins or nucleic acids result in the formation of a pre-metastatic niche at the secondary site of cancer spread. Activation of many signaling pathways and stimulation of diverse immune cells at the secondary site aid in the establishment of a cancer-favorable inflammatory environment, which supports the effective metastasis of cancer cells [92].

Proper isolation of EVs holds vital significance for downstream analyses in cancer and many other studies. The isolation techniques include ultracentrifugation, density gradient separation, size exclusion chromatography, and affinity-based techniques [94]. Among them ultracentrifugation is considered as the gold standard method [95]. It includes separating EVs depending on their size and density through centrifugal forces at ultra-high rates [95], [96]. In this process, briefly, the sample is initially filtered to eliminate larger particles before being centrifuged for 1-2 hours at 100,000 x g. The EV-containing pellet is then collected and resuspended in a buffer for further examination. Another frequent technique for isolating EVs is density gradient separation [97]. It includes the isolation of EVs depending on their density using a density gradient, such as a sucrose or iodixanol gradient. The sample is analyzed to eliminate larger particles before being put on the gradient [98]. Likewise, the sample is then centrifuged at high rates, allowing EVs to move to the same-density layer in the gradient. After that, EVs can be collected and purified for further examination. Size exclusion chromatography, on the other hand, is a technique that is used to separate EVs according to their size. First, the sample is filtered to eliminate larger particles, and then it is passed through a column of beads with precise pore diameters [99]. On the basis of their size, EVs are kept on the column, and the eluted fraction containing EVs may be collected and purified for further studies. Affinity-based approaches employ chemicals or proteins that bind to EVs in a specific manner. EVs can be identified, for instance, by employing antibodies against their antigens such as CD9, CD81 or CD63 (tetraspanins) [100]. Briefly, the EVs are captured through antibody-tagged particles such as magnetic beads [101]. After EVs have been purified, they can be collected for further examinations. There are also a variety of techniques for separating EVs from biological fluids, along their pros and cons. It is hence essential to choose a proper approach depending on the specific objectives of the study, as well as the quality and volume of the sample.

In this thesis, breast cancer cells (MCF-7) were used as model system, and they are cultured in SF-coated microfluidic chips to imitate tumor microenvironment along with the addition of dynamic flow condition. In order to comprehend the effect of flow, as a control, traditional static MCF-7 cell culture was also performed concurrently. At the end of cell-culturing procedure, the impacts of FSS on gene expression, specifically the highly expressed EpCAM and CK-18 genes in MCF-7 cells, were evaluated. Moreover,

the development of anti-cancer drug resistance in cancer cells during FSS was examined. Therefore, cells were treated with anti-cancer drugs (i.e., doxorubicin and docetaxel) under dynamic (microfluidic system in 3D) and static (tissue culture flask in 2D and 3D) culture conditions. Once anti-cancer therapy was completed, *Multi-Drug Resistance 1* (*MDR-1*) and *Breast Cancer Resistance Protein* (*BCRP*) gene expression levels were assessed. The final part of this research involved the isolation and analysis of EVs from static and dynamic cultures in presence and absence of anti-cancer drug. This thesis paved the way for the significance of EVs as biomarkers that would enable real-time monitoring of therapy effectiveness in the future.

CHAPTER 2

2.MATERIALS AND METHOD

2.1 Materials

For cell culture studies, Dulbecco's Modified Eagle Medium/Nutrient Mixture F-12 (DMEM/F-12) with L-glutamine and sodium bicarbonate, without HEPES and Fetal Bovine Serum (FBS) was purchased from PAN Biotech. Dulbecco's phosphate-buffered saline (DPBS) was purchased from Biowest. Trypsin-EDTA (0.25%) and 10,000 U/mL Penicillin- 10,000 µg/mL streptomycin were obtained from Gibco. GenElute™ Mammalian Total RNA Miniprep Kit was purchased from Sigma-Aldrich. High-Capacity cDNA Reverse Transcription Kit, Qubit™ RNA BR Assay Kits, Qubit™ dsDNA BR Assay Kits, Qubit™ Protein Broad Range (BR) Assay Kit and SureCast Gel Handcast System were received from ThermoFisher Scientific. GoTaq® 1-Step RT-qPCR was purchased from Promega.

2.2 Conventional Protocols for Cell Culture

2.2.1 Static 2D Cell Culture

All processes during cell culturing were carried out in a sterile laminar flow cabinet. Before cells were cultured, the laminar flow cabinet was exposed to UV for 15 minutes for sterilization. After the UV process was finished, the inside of the cabinet was cleaned with 70% ethanol. All materials required for culturing cells, such as cell culture flasks, centrifuge tubes, and medium bottles, were wiped with 70% of ethanol before

placing them in the cabinet. MCF-7 cells were grown using Dulbecco's Modified Eagle Medium/Nutrient Mixture F-12 (DMEM/F-12) with L-glutamine and sodium bicarbonate, without HEPES medium containing 10% fetal bovine serum (FBS) and penicillin (100 U/mL), and streptomycin (100 µg/mL) [102]. Then, 5 mL of medium was added to the centrifuge tube and heated in a 37 °C water bath. The vial containing MCF-7 cells stored at -80°C was thawed in a 37°C water bath. Thawed cells were later added into a centrifuge tube containing 5 mL of pre-warmed medium, and consequently, centrifuged at 300 x g for 5 minutes. The supernatant was then discarded, and the cell pellet was resuspended with 5 mL of fresh medium and transferred to the T25 cell culture flask. The cultured cells were kept in an incubator with 5% CO_2, 37°C. The cell medium was refreshed every 2 days. Before each medium change, cells were examined with a microscope (Zeiss Inverted Fluorescence Microscope), and accordingly, cell confluency was determined while they covered >85% of the flask surface. In the case of cell passging, trypsin-EDTA (0.25%) and medium were kept at room temperature for a while. Afterwards, they were wiped with 70% ethanol together with all the necessary materials and taken into the laminar flow cabinet. Initially, medium in the flask was discarded *via* a pipettor, and the flask was washed twice with 2 mL of DPBS in order to remove waste, cell debris, and dead cells in the medium. Later on, 1mL of Trypain-EDTA was introduced into the flask and incubated at 37°C for 5 minutes. After the incubation period was over, fresh medium at least twice the amount of Trypsin-EDTA was applied into the flask, hence neutralizing the harsh effects of trypsin-EDTA over the cells. After adding the medium, cells detached from the surface were suspended several times *via* a pipettor. The cells removed from the surface were counted. 115,000 cells were transferred to a new cell culture flask (25 cm^2 of diameter), and 4 mL of fresh medium was added into the flask. After the passage process was completed, the flask was kept in an incubator under 5% of CO_2 and 37°C of temperature.

2.2.2 Static 3D Cell Culture

Silk fibroin (SF)—a naturally derived biomaterial, has been used widely in tissue engineering and regenerative therapy due to its biocompatibility, processibility, controllable biodegradability and mechanical qualities [103]. For a myriad of biomedical

applications, SF has been applied in several forms of 3D matrix, including scaffolds, fiber, hydrogels, and particles. In this thesis, we utilized SF as 3D matrix to create an extracellular environment for cell culturing. First, SF solution (1 mL; 1 mg/mL) was added into a 25 cm^2 of cell culture flask. Then, the flask was shaken slowly with back-and-forth movements until the solution to which SF was added evenly covered the entire surface of the flask. After that, we left it to dry in the hood for 4-5 hours. After the drying process, 70% of methanol (1 mL) was added to reduce its water solubility and later incubated for 20 minutes by closing the lid of the flask. SF-coated flask was washed with sterile DPBS or sterile medium after the incubation. As detailed in section 2.2.1, cells prepared for 2D cell culturing were passaged for this process as well. Later, the cells removed from the surface were counted and 115,000 cells were added to the surface-coated flask and 4 mL of fresh medium was applied, thereby generating a 3D culture condition.

2.3 Cell Counting

After the cells were collected for both conditions with Trypsin-EDTA, 10 µL of the samples were taken and added into the PCR tube. Afterward, 10 µL of Trypan Blue (1:1) dye was added to the tube. At the end of this process, the live/dead cell counts were determined using a hemocytometer and microscope (Zeiss Axio Vert Inverted Fluorescence Microscope, Germany). In this process, a coverslip was placed to the surface of a hemocytometer, and 10 µL of sample was applied to the cell counting area through the channels on the hemocytometer. Accordingly, white cells represented alive cells whereas blue cells showed dead cells due to their porous membranes. As a result of counting, the number of cells was calculated through the following formula:

$$Total\ Number\ of\ Cells = Number\ of\ counted\ cells\ x\ Dilution\ Factor\ x\ Total\ Volume\ x\ 10^4$$

2.4 Fabricating Microfluidic Chips for Dynamic 3D Cell Culture

The microfluidic chip to be used in the cell culture consists of many different layers (Figure 2.1a-2.1b): (i) top PMMA layer (2 mm thickness) with inlet and outlet ports, (ii) five double-sided adhesive (DSA) films (50 μm of thickness for each film; 250 μm of microchannel height in total) for connecting each layer of the chip, (iii) bottom polystyrene layer (2 mm of thickness), where cells were grown after SF is coated, (iv) PMMA clamps for preventing any potential leakages on the course of cell culturing. These materials used for the chip fabrication were cut *via* a laser cutter system (LazerFix, Türkiye). All the design parameters were operated using RDWork V8 Software (China). The tubings were utilized for sampling and introducing medium, and they were simply cut with a razor. Tubings for the inlet port were cut 60 cm-long whereas those for the outlet ports were 20 cm-long. Before constructing all these layers and components, the PMMA layers, tubing, screws, and nuts to hold the clamps, screwdriver and tweezers required to produce the microfluidic chip were cleaned with absolute ethanol and sterilized by UV for 1 hour in the laminar flow cabinet. Since SF was received as sterile, we did not perform any sterilization procedure for it, and therefore, all preparation steps for SF were carried out inside the laminar flow cabinet. On the other hand, SF should not undergo any UV process because a strong and extended UV exposure could have chances to alter the molecular structure of this biomaterial [104]. DSA films were not also sterilized through the UV process because they could lose their structure in connecting process. Therefore, DSA films were cleaned with 100% of ethanol due to their compatibility with organic solvents. Once the sterilization process was finalized, we constructed the microfluidic chips under a laminar flow cabinet. Initially, a DSA film having a microchannel configuration was adhered to a polystyrene layer. Afterwards, the microchannels were modified with SF (150 μL; 1mg/mL) by simply drop-casting the solution and incubating for 2-3 hours in the hood. To ensure proper spread of SF in the entire microchannel, we used a pipette tip for the drop-casting process. After SF dried, 70% of methanol was applied to cover the microchannels and incubated for 20 minutes, and therefore, we aimed to reduce water solubility of SF. During this process, the

microfluidic chip was placed on a petri dish; the lid was closed, and hence methanol did not evaporate. After this period, the microfluidic channels were washed three times with sterile DPBS or a sterile medium. It was important that the channels dried thoroughly after the washing step. Otherwise, the other DSA layers will not completely adhere for the remaining construction. Later, four more layers of DSA and the top PMMA layer were sealed to complete the construction of a microfluidic chip (Figure 2.1c). Finally, the microfluidic chip was placed between the clamps, which were fixed to each other with screws and nuts (Figure 2.1d). The last step was to integrate the tubings into the inlet and outlet ports on the top PMMA layer *via* epoxy (Figure 2.1e).

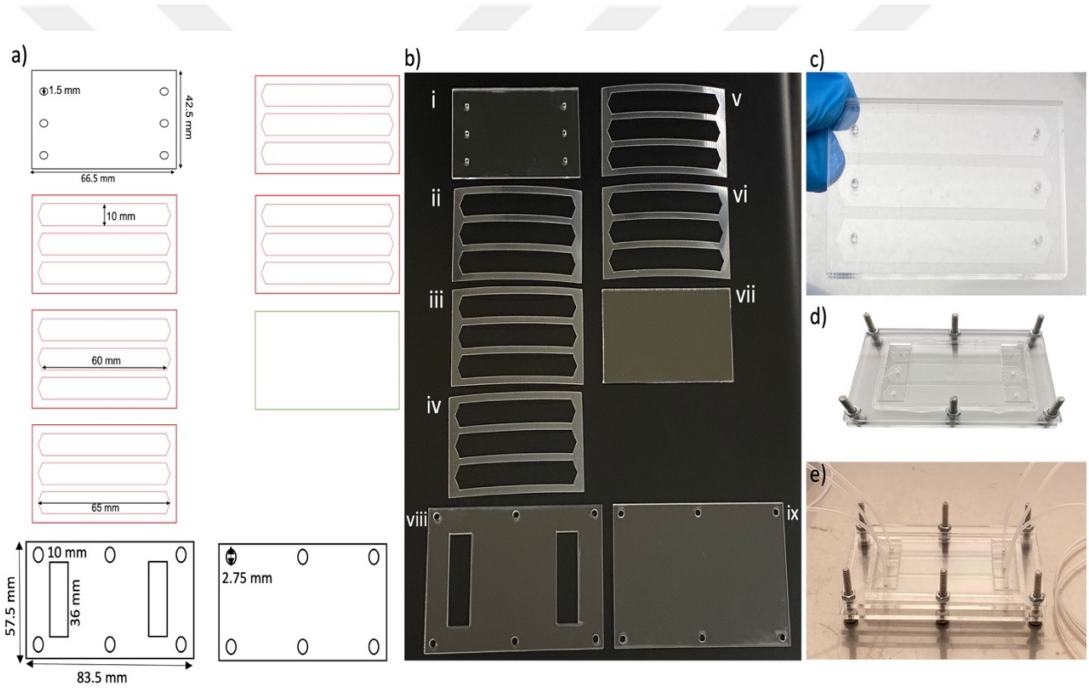


Figure 2.1. a) a) The design parameters of a microfluidic chip are presented. Black color indicates PMMA layers, red color indicates DSA films, and green color represents polystyrene layer. b) A microfluidic chip is constructed with many layers of PMMA, DSA films and polystyrene. The numbers of i-vii numbers indicate these layers from the top to the bottom. The numbers of viii-ix numbers state clamps. c) Top view of a microfluidic chip is exhibited. d) Top view of a microfluidic chip with clamps and screws. e) Through tubings attached to inlet and outlet ports, sampling and collecting cells are utilized

2.5 Cell Culture under Dynamic 3D Condition

The stock cells described in Chapter 2.1 were initially trypsinized and counted accordingly. After calculating the cell number in the stock culture, we adjusted 115,000 cells per microchannels and applied into the chips through tubings. The important point here was to know the volume of tubings, because some cells could remain there during this process. Cells inside the microchannels were incubated for 24 hours in an incubator set as 5% of CO_2 and 37°C. During this period, cells adhered to the surface of the microchannels (Figure 2.2). After the incubation period, the inlet tubing was connected to the syringe pump, which was located outside the incubator. Outlet tubings were placed in the reservoir with fresh medium, and medium was withdrawn into the microchannels at a flow rate of 2 µL/minutes *via* a syringe pump (KF Technology, Roma, Italy).

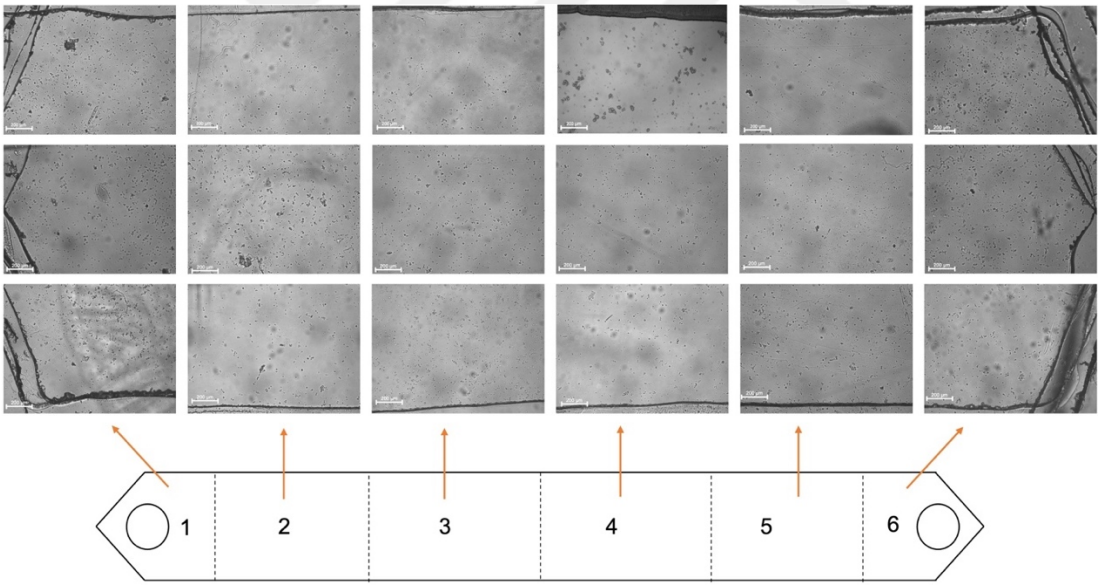


Figure 2.2. Images of cells cultured in a microfluidic chip after 24 hours. Cells are distributed evenly in different regions of the chip.

2.6 Cell Imaging

For cells cultured under static conditions (either 2D or 3D), 1 mL of Hoechst 33342 dye was applied to the cell culture flask. After 10 minutes of incubation in dark, the flask was washed with 1 mL of PBS three times, and cells were visualized with a fluorescence microscope (excitation/emission values of 350 nm/461 nm).

Regarding the cells cultured under dynamic condition (microfluidic chip), 3D structures have begun to appear in the microchannels from the 4^{th} day of culture. To stain their nuclei, 100 µL of Hoechst 33342 dye was introduced into the microchannels and incubated for 10 minutes under dark conditions. Later, the excessive dye was removed from the chip by manually injecting PBS *via* a syringe. Cells stained with Hoechst 33342 were visualized similarly to the static condition.

2.7 Anti-cancer Drug Studies

Doxorubicin and Docetaxel were utilized as anti-cancer drugs for this study. For both drugs, four different drug doses were determined (10^5 nM, 10^3 nM, 10 nM, and 0.1 nM) according to the literature [105], [106]. The drugs were administered to the cells for 72 hours. Cells cultured in both static (2D and 3D) and dynamic (3D) conditions were started to receive drugs on the 4^{th} day of culture. After 72 hours, the experiments were completed, and downstream analyzes were performed.

2.8 Imaging of Anti-cancer Drugs Treated Cells

Cells treated with doxorubicin and docetaxel were visualized at the end of the experiment with the LIVE/DEAD™ Viability/Cytotoxicity Kit for both static and dynamic conditions. Calcein AM in the content of this kit stains alive cells in green, whereas Ethidium Homodimer-1 stains dead cells in red. Per the manufacturer's protocol, a dye solution was prepared by adding 5 µL of Calcein AM and 20 µL of Ethidium

Homodimer-1 into 10 mL of DPBS. For static condition, medium in the flask was discarded, and 1 mL of dye solution was introduced into the flask. For the cells in dynamic condition, 500 µL of dye was introduced into the microchannels *via* tubings. For both cases, 30-minute incubation was performed at 20-25 °C, and we then visualized the cells under a fluorescence microscope (excitation/emission values of 494/517 nm for calcein AM, 528 nm/617 nm for ethidium homodimer-1).

2.9 RNA Isolation

Cells in both static and dynamic conditions were harvested with Tyrpsin-EDTA solution after the 7th day of culture. Regarding the cells in static condition, 1 mL of Trypsin-EDTA was added into the flasks and incubated for 5 minutes. Then, 3 mL of fresh medium was added to the cells and transferred into a falcon tube. For the cells in dynamic condition, the falcon tube containing 3 mL of medium was placed in the outlet tubing. To immediately neutralize trypsin and protect cells from any potential damages caused by a prolonged incubation with Trypsin-EDTA, cells in the microchannels were harvested in a falcon tube containing growth medium. Trypsin-EDTA was delivered to the microchannels with a syringe pump at a flow rate of 200 µL/min for 5 minutes. After collecting the cells in both conditions, they were centrifuged at 300 x g for 5 minutes. The supernatant was discarded, and 500 µL of lysis buffer containing 1% (v/v) 2-mercaptoethanol was added to the pellet. Vortexing or pipetting was performed until clump disappeared. Consequently, the lysed cells were added into a filtration column placed in 2 mL of a collection tube. The filtration tube was centrifuged at 12000 x g for 2 minutes. After this step, 500 µL of 70% ethanol was added to the resultant solution and mixed thoroughly by vortexing or pipetting. The binding column was inserted to a new collection tube. Then, 700 µL of lysate-ethanol mixture was introduced to the column and centrifuged at 12000 x g for 15 seconds. The flow-through solution was discarded, and the same step was repeated for the remaining sample. The waste phase in the collection tube was discarded, and 500 µL of Wash Solution I was added to the binding column that followed a centrifugation step operated at 12000 x g for 15 seconds. After this step, the binding column was taken into a new collection tube and 500 µL of Wash Solution II was

again added and centrifuged at 12000 x g for 15 seconds. Then, the flow-through solution was discarded, and this step was repeated for the second time. Unlike in the first round, the centrifugation was performed at 12000 x g for 2 minutes for the second time. After the washing step was finalized, the binding column was centrifuged at 16000 x g for another minute, and we hence removed the column from ethanol. Finally, the binding column was placed in a new collection tube, and 50 µL of the elution solution was added in the middle of membrane and centrifuged at 12000 x g for a minute. If the expected RNA concentration was higher than 50 µg, another 50 µL of elution solution was added to the column and centrifuged again.

2.10 RNA Quantification

Qubit™ RNA High Sensitivity assay kit was utilized for this procedure. The working solution was prepared by diluting RNA HS reagent in RNA HS buffer at the ratio of 1:200. Then, Qubit 4.0 Fluorometer device was calibrated per the manufacturer's procedure. Briefly, 10 µL of Standard 1 and 10 µL of Standard 2 were added into separate tubes. Then, 190 µL of the working solution was added into tubes and vortex was performed for 5-7 seconds that followed an incubation for 2 minutes under dark condition. For the calibration, Standard 1 was placed on the instrument, and measurement was completed. Then, Standard 2 was applied and the calibration was completed. For the calibration, the values shown on the instrument and the values of the standards needed to be compared. Otherwise, RNA concentration would not be measured accurately. Finally, in order to quantify RNA concentration for each sample, 2 µL of RNA sample and 198 µL of working solution were mixed, and incubated for 2 minutes under dark conditions, and measured on the instrument like the calibration process.

2.11 cDNA Synthesis

High-Capacity cDNA Reverse Transcription Kit was used in this procedure. Briefly, master mix for a single sample was prepared by adding 2 µL of 10× RT buffer solution, 0.8 µL of 25× dNTP mix, 2 µL of 10× RT random primers, 1 µL of Reverse

transcriptase, and 4.2 µL of nuclease-free water into a tube. Later, 10 µL of the master mix was added to the PCR tube, and 10 µL of RNA sample was added to it. Tubes were spined in a microcentrifuge (VWR, Pennsylvania, USA) for 10 seconds, and thereby, no air bubbles remained in the tube. The tubes were placed in the thermal cycler and programmed for 10 minutes at 25°C, 120 minutes at 37°C, 5 minutes at 85°C, and cooling to 4°C.

2.12 Confirming cDNA Synthesis

Synthesized cDNAs were confirmed in two distinct methods: (i) agarose gel electrophoresis and (ii) Qubit fluorometer. For the agarose gel electrophoresis, PCR amplification was performed using the relevant genes from each sample using the A.B.T PCR Premix Kit. Briefly, 1 µL of Forward primer, 1 µL of Reverse primer, 2 µL of cDNA sample, and 16 µL of nuclease-free water were added to the PCR premix in strips. The prepared samples were centrifuged for 15 seconds using a microcentrifuge. After this step, the strips were placed in the thermal cycler device, and the device was set to 95°C for 2 minutes (95°C for 20 seconds, 60°C for 10 seconds, and 72°C for 20 seconds) along with 35 cycles of repeats, 72°C for 5 minutes, 4-12°C for 5 minutes. While PCR was in progress, we prepared 1% of agarose gel by mixing 1 gram of powdered agarose and 100 mL of TAE buffer. To dissolve agarose, the mixture was placed in the microwave oven and heated for 30-40 seconds. The important point here was to check agarose by turning on the microwave every 10 seconds since agarose would not boil. After agarose was dissolved, it was left to warm at room temperature, and 2 µL of SYBR Safe DNA was added to the solution. Then, the solution was poured into an electrophoresis tray. The comb was placed quickly, and then, the gel was allowed to solidify. Afterward, the tray was filled with TAE buffer until it did not overflow, and the comb was slowly removed from the gel. PCR samples were prepared for agarose gel by mixing 1 µL of 5X loading dye with 4 µL of DNA sample, and then, loaded into the wells. The gel was run at 90 V for 30 minutes. It was important to check the gel every 10 minutes because samples could separate quickly and come out of the gel. Finally, the gel was visualized with the ChemiDoc MP UV illumination device (Bio-Rad, California, USA).

Regarding the second method, Qubit™ 1X dsDNA Broad Range assay kit was used to determine cDNA concentrations. In this regard, 1X dsDNA BR reagent was diluted in dsDNA BR buffer at a ratio of 1:200, and therefore the working solution was prepared. Next, Qubit 4.0 Fluorometer was calibrated. For this step, Separate tubes were loaded with 10 µL of Standard 1 and 10 µL of Standard 2. After that, 190 µL of the working solution was introduced into the tubes, and they were vortexed. The tubes were incubated for 2 minutes in the dark. To calibrate the device, Standard 1 was first measured, and then, another measurement was taken with Standard 2, thereby finalizing the calibration process. In order to be able to measure the sample after the calibration, 198 µL of working solution and 2 µL of cDNA sample were added into the microtube and vortex was performed for 5-7 seconds. Samples were incubated for 2 minutes in the dark. After incubation, the samples were placed to the Qubit instrument, and the measurement was performed.

2.13 Quantitative Real-Time Polymerase Chain Reaction (RT-qPCR)

The Promega GoTaq® 1-Step RT-qPCR kit was used for this step. The samples were prepared for the analysis by adding 5 µL of RT-qPCR master mix, 0.4 µL of forward primer, 0.4 µL of reverse primer, 1 µL of cDNA sample, and 3.2 µL of nuclease-free water into the PCR strips. The prepared strips were placed in the real time-qPCR instrument (Bio-Rad CFX96, California, USA) and programmed to 95°C for 5 minutes (95°C for 10 seconds, 60°C for 40 seconds) along with 40 cycles of repeats. The expressions of 5 different genes (*GAPDH, EpCam, CK-18, MDR-1,* and *BCRP*) were examined in the experiments, and according to the literature, their primers were designed as follows:

GAPDH [107]
Forward ; 5'- TCCCTGAGCTGAACGGGAAG-3'
Reverse: 5'- GGAGGAGTGGGTGTCGCTGT-3'

EpCam [108]
Forward : 5′-AATCGTCAATGCCAGTGTACTT-3′
Reverse : 5′-TCTCATCGCAGTCAGGATCATAA-3′

CK-18 [107]
Forward : 5’-ATCTTGGTGATGCCTTGGAC-3’
Reverse : 5’- CCTGCTTCTGCTGGCTTAAT-3’

MDR-1 [109]
Forward : 5’- GCTGTCAAGGAAGCCAATGCCT -3’
Reverse : 5’- TGCAATGGCGATCCTCTGCTTC -3’

BCRP [110]
Forward : 5’- TGGCTGTCATGGCTTCAGTA-3’
Reverse : 5’- GCCACGTGATTCTTCCACAA-3’

2.14 Isolating Extracellular Vesicles using a Microfluidic Device

Similar to the fabrication of microfluidic chip for dynamic 3D cell culture, the materials of microfluidic device for isolating EVs were designed with RDWorks Software and cut *via* a laser cutter. Isolation of EVs was focused on serial ultrafiltration process on a microfluidic device. As reported in the literature [111], this microfluidic device had multiple membranes. Briefly, the first filter had 200 nm of pore size, and enable to remove any large particles, whereas the second filter (50 nm of pore size) allowed to fine-tune the filtrate size that could reach the EV size distribution (especially the category of exosomes). This device combined cross- and dead-end flow at the same time. [82]. In the design of this device, there were five PMMA layers (2 mm of thickness for each layer) and five DSA film (50 μm of thickness for each film) (Figure 2.3a). The assembly order applied for the construction of the microfluidic chip is shown in Figure 2.3b. In the

construction, three PMMA layers were positioned above the filters, and the other layers were placed underneath (Figure 2.3c). Afterward, the tubings were fixed with epoxy to the inlet and outlet ports for sampling and collecting EVs (Figure 2.3d).

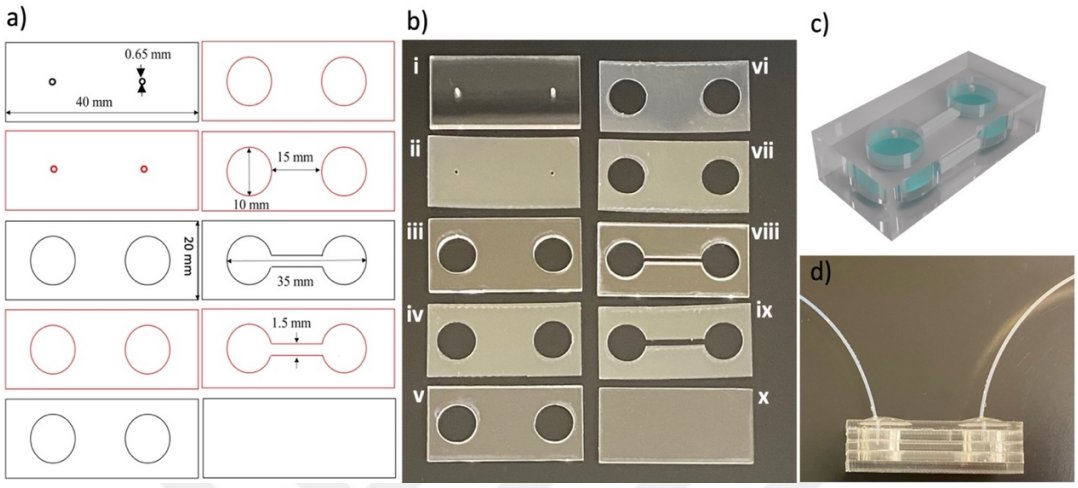


Figure 2.3. a) Design parameters of a microfluidic chip is displayed. Black color state PMMA layers and red color represents DSA films. b) The assembly order of chip components is represented by roman numbers. Moreover, membranes with pore sizes of 200 nm and 50 nm are integrated between layers vi and vii. c) The 3D view of microfluidic chip is denoted. d) Side-view of microfluidic chip is displayed.

2.15 Isolating Extracellular Vesicles

EVs were collected from MCF-7 cells in either the presence or absence of anti-cancer drugs. For drug-free experiments, cells were cultured continuously for 7 days under static and dynamic conditions. At the end of 7 days, medium in the flasks for static culture, whereas, for dynamic culture, medium accumulated in the syringes were collected. The media were divided into 2 mL of Eppendorf tubes and centrifuged at 20000 x g (14000 x rpm) for 15 minutes at room temperature. The purpose of this centrifugation was to remove large molecules, dead cells, and cell debris. After the centrifugation, supernatant containing EVs was transferred into a clean tube. Supernatant was then filtered with 0.22 µm of syringe filters, hence eliminating any potential bacterial contaminations. The samples were transferred to the microfluidic device through a syringe pump at a rate of 40 µL/min. The isolated EVs were collected in an Eppendorf

tubes from the outlet port. For anti-cancer drug studies (detailed in the Chapter 2), cells were cultured in both static and dynamic environments. On the 4th day of culture, the designated doses of anti-cancer drugs were added to cell culture medium. The drug study was finalize at the end of the 7th day, and EVs were isolation as described above.

2.16 Determining Protein Concentration of Isolated Extracellular Vesicles

Prior to Western Blot analysis, protein concentration was determined using Qubit^{TM} Protein Broad Range (BR) Assay Kit. The Qubit instrument was initially calibrated by preparing two standards: (i) 20 µL of Standard 1, 150 µL of Protein BR assay buffer and 30 µL Protein BR reagent, (ii) 20 µL of Standard 2, 150 µL of Protein BR assay buffer and 30 µL Protein BR reagent. After preparing the standard tubes, vortex was performed for 5-7 seconds, and the tubes were incubated for 10 minutes at room temperature. During the incubation, EV and blank samples were prepared by following the same procedure. For sample preparation, 20 µL of sample, 150 µL of buffer and 30 µL of reagent are added into the tubes and vortexed. Moreover, the samples were incubated for 10 minutes at room temperature. After the incubation, calibration was finalized with the standards. Sample measurements were performed on the device that had been calibrated.

2.17 Characterization Methods

Characterization methods were detailed under two groups: (i) Characterization Surface Chemistry on Microfluidic Chips and (ii) Characterizing Extracellular Vesicles (EVs). Contact angle, Fourier Transform Infrared Spectroscopy (FTIR), and X-Ray Photoelectron Spectroscopy (XPS) analyzes were used to select the most appropriate material for constructing the bottom surface of microfluidic chip for immobilizing SF. Nanoparticle Tracking Analysis (NTA) was performed for determining concentration and size characterization of EVs, as well as we confirmed EV size and morphology through

SEM analysis. Western blot was also used to demonstrate the presence of specific EV-related proteins.

2.17.1 Characterization Surface Chemistry on Microfluidic Chips

2.17.1.1 Contact Angle

In order to determine the hydrophilicity of a surface, we performed contact angle measurements for unmodified glass, PMMA, and polystyrene surfaces, along with their SF-coated surfaces. Therefore, we were able to understand whether the coated surface had different characteristics from unmodified surfaces in terms of cellular adhesion. Basically, the contact angle is formed where a liquid meets a solid surface [112]. It also enables the wetting properties of the liquid and can be used to determine the surface tension and interfacial energy between the liquid and the solid. Wherever it is necessary to regulate or assess the degree of phase contact between liquids and solids, the contact angle is one of the mainstay parameters, maybe one of the most facile measurements that can be applied at first. In this study, we employed Contact Angle Measurement System (Dataphysics, OCA 30, Germany) in order to understand hydrophilicity of the surfaces. Samples were placed on the stage, which was raised to 3-4 mm between the needle where the water was dripped. The sessile drop method was selected in the system software, and volume (5 μL) and speed of the drop were adjusted. After all the adjustments, the drop was released on the sample, and at least three images were taken for accurate assessments.

2.17.1.2 Fourier Transform Infrared Spectroscopy (FTIR)

In this study, Fourier Transform Infrared Spectroscopy (FTIR) analysis was employed to understand the binding of SF to three different surfaces, *i.e.,* glass, PMMA,

and polystyrene. The FTIR data for bare surfaces and SF-coated versions were then compared. Basically, FTIR method enables to understand chemical bonds in the structure of molecules [113]. Based on the idea that distinct molecules absorb infrared light at particular wavelengths, it is feasible to identify the molecules present in a sample and establish their composition by measuring the absorption at different wavelengths [114]. FTIR operates by directing an infrared light beam through a sample and measuring the quantity of energy absorbed at various wavelengths. The resultant absorption spectrum is then examined using a mathematical technique called the Fourier transform, enabling the identification of individual compounds present in a sample along with their relative intensities [114]. One of the primary benefits of FTIR is to identify extremely minute concentrations of molecules in a sample. It is also a non-destructive approach, and hence, this enables to broaden the applicability of FTIR method within a wide range of applications, such as the study of biological samples and materials with fragile structures [115].

In this study, analyzes were carried out using the Vertex 70 FTIR Spectroscopy (Bruker, Germany) device. Briefly, the sample was placed on the crystal area on the instrument, and the probe was moved until it touched the surface of the sample to be analyzed. The probe touching the sample was carefully clamped. In the software of the device, firstly, the optical settings are checked. Then the signal is checked and the measurement begins. The results are obtained by taking 32 scans for each sample.

2.17.1.3 X-Ray Photoelectron Spectroscopy (XPS)

In this study, unmodified glass, PMMA, and polystyrene surfaces along with their SF-coated versions were studied using the XPS method in order to analyze the chemical bonding of these materials with SF. Principally, X-Ray Photoelectron Spectroscopy (XPS) identifies chemical elements that are present on the surface of materials and accordingly describes the types of chemical link that occurs between them [116]. Except for hydrogen and helium, XPS method is able to identify all elements. The surface of a material is subjected to high-energy X-ray beams to excite electrons that are confined in particular states. Some of the excited photoelectrons are ejected from the surface [117]. In this thesis, we carried out an analysis through X-Ray Photoelectron Spectroscopy (K-

Alpha XPS, ThermoFisher Scientific, USA). XPS analysis of C1s and N1s scans were performed for the bare version of glass, PMMA and polystyrene surface, along with their SF-coated versions.

2.17.2 Characterizing Extracellular Vesicles

2.17.2.1 Nanoparticle Tracking Analysis (NTA)

Nanoparticle Tracking Analysis (NTA) (NS300, Malvern Instruments Ltd., Malvern, Worcestershire, UK) characterizes concentration and size patterns of nanoparticles such as EVs [118]. In order to track the Brownian motion of a particle in a liquid environment, NTA employs an optical system that is laser-based. Prior beginning the measurement, the tubing was flushed with distilled water to eliminate any contaminants. The laser wavelength for imaging and size profiling of EVs was 488 nm. During the operation of this instrument, EVs were initially introduced into a sample chamber equipped with a CCD camera and 488 nm laser in order to assess concentration and size. The diameter of the particles was measured by using the Stokes-Einstein equation. Before the analyses, capture number (five), capture time (60 seconds), temperature (25 °C), dilution rate and viscosity (0.92 mPa.s) were adjusted in the software for the study.

2.17.2.2 Scanning Electron Microscope (SEM)

Scanning Electron Microscope (SEM) was used to characterize EVs morphologically. In principle, electrons with high energy interact with a sample, releasing electron and photon signals in the SEM method. The images are produced by processing the acquired signals using microscope software after the detector (sensor) has collected electrons scattered at various angles. Relying on atomic number and contrast, secondary electrons, material morphology, and backscattered electrons can be used to estimate an atomic composition [119]. Furthermore, the EDS detector is used to map the

dispersion of the elements using line, point, or regional qualitative and quantitative analysis. SEM can be used to investigate conductive samples, coated insulating samples, powder samples, thin films, biological samples, and polymers [120].

For this regard, silicon wafers were cut into 0.5 x 0.5 mm, and they were utilized as substrates for the analysis. We then sonicated these wafer surfaces in ethanol for 5 minutes, followed by another sonication in distilled water for 5 minutes. The cleaned silicon wafers were dried with compressed air. EVs isolated from both drug and non-drug studies at different conditions (static 2D and 3D, and dynamic 3D conditions) were mixed with 2% of paraformaldehyde (PFA) (1:1 (v:v)), thereby fixing the particles to keep them intact structure as much as possible. Then, 10 µL of PFA-EV solution was dropped onto the silicon wafer. Once the samples dried, they were washed three times with ethanol and allowed to dry again at room temperature. Before the imaging process, 10 nm of gold was coated on the wafer surface in order to make them conductive for accurate imaging. The samples were visualized by Scanning Electron Microscope (SEM) (FEI Quanta 200 FEG, USA), and the images were analyzed on Image J software for calculating EVs diameter (LOCI, University of Wisconsin, USA).

2.17.2.3 Western Blot

Western Blot analysis was employed to characterize the presence of tetraspanins (CD63 and CD81) biomarkers on EVs. Basically, stacking gel and resolving gel are two main forms of polyacrylamide gels that used separate proteins for each sample more effectively. pH, polyacrylamide amount, pore diameter, and function of these two gels are distinct [121]. The lower polyacrylamide amount in stacking gel creates smaller pore diameters in stacking gel [122]. After the samples are loaded into the wells, they are first separated in the stacking gel. The purpose of this gel is to align all samples before passing into the resolving gel so that they all pass into the gel at the same time. The purpose of the resolving gel is to separate proteins according to the molecular weight of proteins. In this work, 10% of resolving gel and 4% of stacking gel were prepared. To prepare the resolving gel, 3900 µL ddH2O, 2000 µL 1.5 M Tris pH 8.8, 2000 µL 40% Acrylamide mix, 80 µL 10% APS and 8 µL TEMED were added falcon tube, respectively. After

adding TEMED into the resolving gel mix, the gel was poured between glasses within a short time. The front and back of glass plates were placed in the gel holding station to form the gel. The resolving gel was then poured up to the fill level on the glass. In order to avoid any bubbles on the gel, isopropanol alcohol was added immediately, and gel was then allowed to solidify for 15 minutes. While the resolving gel dries, a stacking gel was prepared. To prepare stacking gel, 1920 µL ddH2O, 750 µL 1.5 M Tris pH 8.8, 300 µL 40% Acrylamide mix, 30 µL 10% APS and 3 µL TEMED were added in tube, respectively. After the resolving gel dried, isopropanol was poured, and the remaining was completely dried with the help of Whatman paper. To complete gel formation, stacking gel was poured on the dried gel, and the comb was swiftly placed on the gel. As the gel was being allowed to solidify, samples were prepared. This was accomplished by combining 10 µL of sample with 9 µL of loading dye and 1 µL of 1M DTT. The sample mixture was boiled to 95˚C for 10 minutes. Then, the gel was placed into the gel tank, which was then filled with 1X running buffer (25 mM Tris, 192 mM glycine, 10% SDS, and ddH2O). While the gel was in the tank, the comb was removed with care and the samples were loaded into the wells. The samples are separated in the stacking gel for 30 minutes at 90 V. This value is increased to 120 V while the samples are transferred to the resolving gel and the samples are separated for another 45 minutes. The Power Blotter XL System (ThermoFisher Scientific, USA) was used to transfer the separated proteins on the gel to the membrane. This system utilized a transfer kit containing a PVDF membrane. A gel was then placed on the PVDF membrane and other layers such as sponge and Whatman paper in the kit were covered on the gel. With the help of a roller, the bubbles between the gel and the membrane were removed. The transfer device was adjusted to 25 V and 1.3 A, and the transfer process was initiated. Once it was completed, the membranes were blocked for an hour at room temperature in 5% milk-TBST buffer (non-fat milk powder, 10 mM Tris pH 7.6, 15.4 mM NaCl, and 0.1% Tween 20). At the end of the blocking procedure, the membranes were washed with TBST buffer. While the membranes were being blocked, primary anti-CD81 antibodies (Invitrogen MA5-33123, ThermoFisher) (1.2 mg/mL) and primary anti-CD63 antibodies (Invitrogen MA5-30187, ThermoFisher) (1 mg/mL) were prepared at a ratio of 1:1000 in 5% milk-TBST. Following blocking, the membranes were incubated overnight at 4°C with primary antibodies. During this incubation time, it was crucial that the membranes be gently

shaken on a shaker. The membranes were then rinsed three times for 10 minutes with TBST. Finally, the membranes were incubated for an hour at room temperature with secondary antibodies. Anti-CD81 antibodies and anti-CD63 antibodies utilized goat anti-rabbit Horseradish Peroxidase (HRP) secondary antibody. Finally, the membranes were washed three times for 10 minutes with TBST. To visualize the membranes, 100 µL of mixture of Luminol/Enhancer and Stable Peroxide Buffer (1:1 (v:v)), was added to the membranes and incubated for 5 minutes under dark environment. After the incubation, membranes were visualized with the ChemiDoc MP instrument (Bio-Rad, California, USA)

CHAPTER 3

3.GENE EXPRESSION AND FLUID SHEAR STRESS RELATIONSHIP

3.1 Completion of the microfluidic chip

In this section, it is aimed to investigate whether fluid shear stress has an effect on gene expression. Cells were cultured with three different cell culturing methods (static 2D, static 3D and dynamic). Culturing of cells in Static 2D, Static 3D and Dynamic conditions are described in detail in sections 2.2.1.- 2.2.2. and 2.5. In summary, in static 2D culture, cells are grown in a monolayer in a cell culture flask. In static 3D cell culture, cells are grown in a cell culture flask covered with SF. Finally, in dynamic culture, cells are cultured in SF-coated microfluidic systems. The cell culture flask used for static 2D and static 3D cell culture consists of polystyrene. In the microfluidic chip that will form the dynamic culture system, the usability of glass, PMMA and polystyrene materials for the bottom layer to be covered with SF, where cells will grow, was investigated. First of all, contact angle analysis, FTIR analysis and XPS analysis were performed to select the most suitable bottom surface. After selection of bottom layer. cells were cultured with three different methods and downstream analysis were performed.

Bare glass surface had a hydrophilic characteristic, and its contact angle measurement was calculated 72.2° ± 2.4° (Figure 3.1 a-i). After SF coating, the surface hydrophilicity increased to contact angle of 70.4° ± 3.08° (Figure 3.1 a-ii). Like bare glass surface, bare PMMA surface possessed a hydrophilic quality along with a contact angle of 76.1° ± 2.95°(Figure 3.1 b-i). The contact angle value measured after the PMMA surface is covered with SF is 69.5° ± 1.61° (Figure 3.1 b-ii). Hydrophilicity increased for this surface as well. Finally, contact angle measurements were made on bare polystyrene and silk-coated polystyrene surfaces, and the results are 81.4° ± 0.89° and 78.6° 1.37°,

respectively (Figure 3.1c). After coating with SF on three surfaces, contact angles decreased and hydrophilicity increased (Figure 3.1d). Hydrophilic surfaces are very important for better attachment of cells [123].

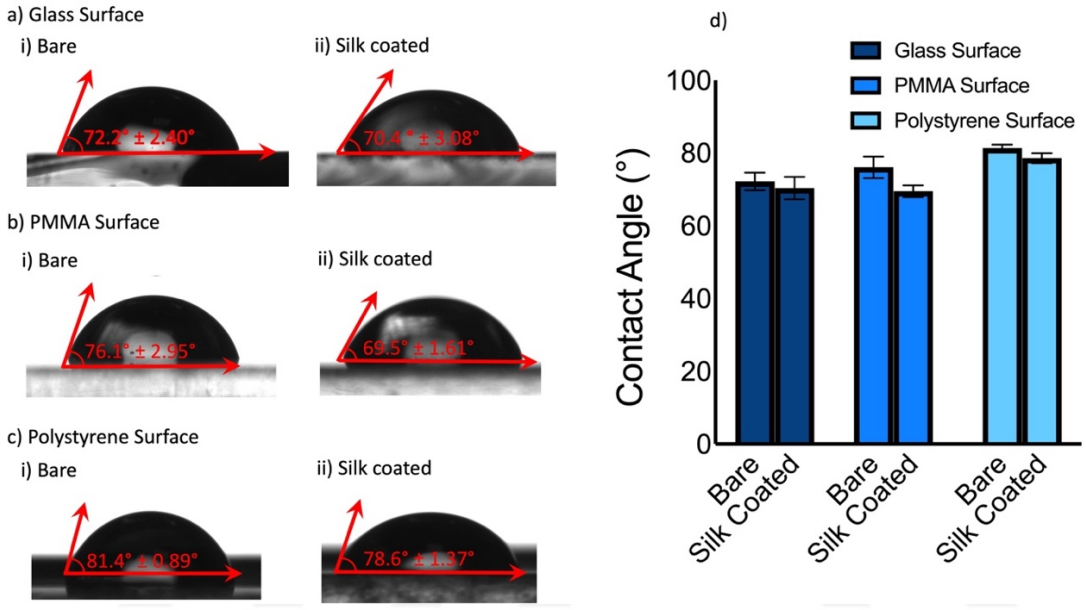
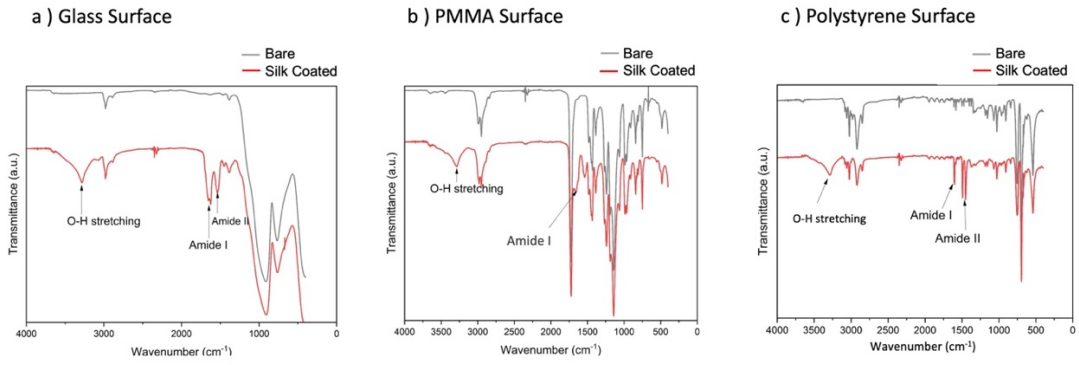


Figure 3.1. Contact angle analysis for before (bare versions) and after silk coating to a) glass, b) PMMA, and c) polystyrene surfaces. d) Contact angle changes are presented quantitatively for each surface.

Another analysis for blank surfaces and SF-coated states is FTIR analysis. The aim here is to understand the surface binding of SF. With Amide I and Amide II bonds on the first fibroin binding surfaces. The transmittance of the Amide I bond is at wavenumber 1620-1700 [124]. On the other hand, Amide II bonds' transmittance is at the wavenumber range of 1515-1550 [124]. As seen in Figure 3.2a, there is no peak between 1500-1700 values on the bare glass surface. After the glass surface is covered with SF, both Amide I and Amide II peaks are seen (Figure 3.2a). This proves the presence of SF on the glass surface. On the other hand, when looking at the PMMA surface, the difference between the SF-coated surface and the empty surface is the Amide I peak (Figure 3.2b). This may be because PMMA material has many coatings. Therefore,

the Amide II peak may not have appeared. Another reason is the inability of SF to bond adequately with PMMA. Finally, Amide I and Amide II bonds are seen on the polystyrene surface covered with silk (Figure 3.2c). According to these results, the use of glass and polystyrene is quite suitable for bonding SF.



Conformation	Amides and Wavelengths (cm^{-1})	
	I (CO stretch)	II (NH bending)
Silk Fibroin	1620-1700	1515-1550

Figure 3.2. FTIR analysis for before (bare versions) and after silk coating to a) glass, b) PMMA, and c) polystyrene surfaces.

Finally, XPS analysis was performed to determine the base material for constructing a microfluidic chip. Since nitrogen and carbon are abundant in the structure of SF, N1s and C1s analyzes were carried out for this characterization. While evaluating the bonds at the bare glass surface, we observed C-C/C-H bonds at 284.07 eV, C-O bonds at 284.56 eV and C=O bonds at 285.11 eV for C1s analysis (Figure 3.3a). In the C1s analysis of SF-coated glass surface, there were C-C/C-H bonds at 284.04 eV, C-O bonds at 284.9 eV and C=O bonds at 286.7 eV (Figure 3.3b). The bond types between two versions were preserved; yet the number of bonds increased on the SF-coated surfaces in all three carbon bonds. N1s scan of the bare glass revealed no nitrogen-atom-associated peak as expected (Figure 3.3c). Due to nitrogen presence of the SF, the N1s scan was associated with amide bonds appeared at 398.60 eV when the surface was coated with SF (Figure 3.3d). Similar to the bare glass surface, C-C/C-H bonds at 284.00 eV, C-O bonds

at 284.7 eV and C=O bonds at 287.2 eV were observed on the bare PMMA surface for C1s analysis (Figure 3.3e). After the PMMA surface was covered with SF, C-C/C-H, C-O and C=O bonds were observed at 283.4 eV, 284.8 eV and 286.6 eV, respectively (Figure 3.3f). After coating, the bond types remained the same and their numbers amplified. While the paucity of nitrogen bonds on the bare PMMA surface, an amide peak of 398.46 eV was observed on the SF-coated PMMA surface (Figure 3.3g-h). Finally, when assessing the bonds at the polystyrene surfaces, unlike the bare glass and bare PMMA, only C-C/C-H bond was seen at 284.9 eV for the bare version of polystyrene surface (Figure 3.3i). After the polystyrene surface was coated with SF, C-C/C-H , C-O and C=O peaks were observed at 284.75 eV, 286.17 eV and 287.90 eV, respectively (Figure 3.3j). As observed for the other surfaces, we did not see any nitrogen bonds on the bare polystyrene surface in N1s analysis; yet, after coating with SF, amide bond was obvious at the binding energy of 399.79 eV (Figure 3.3k-l).

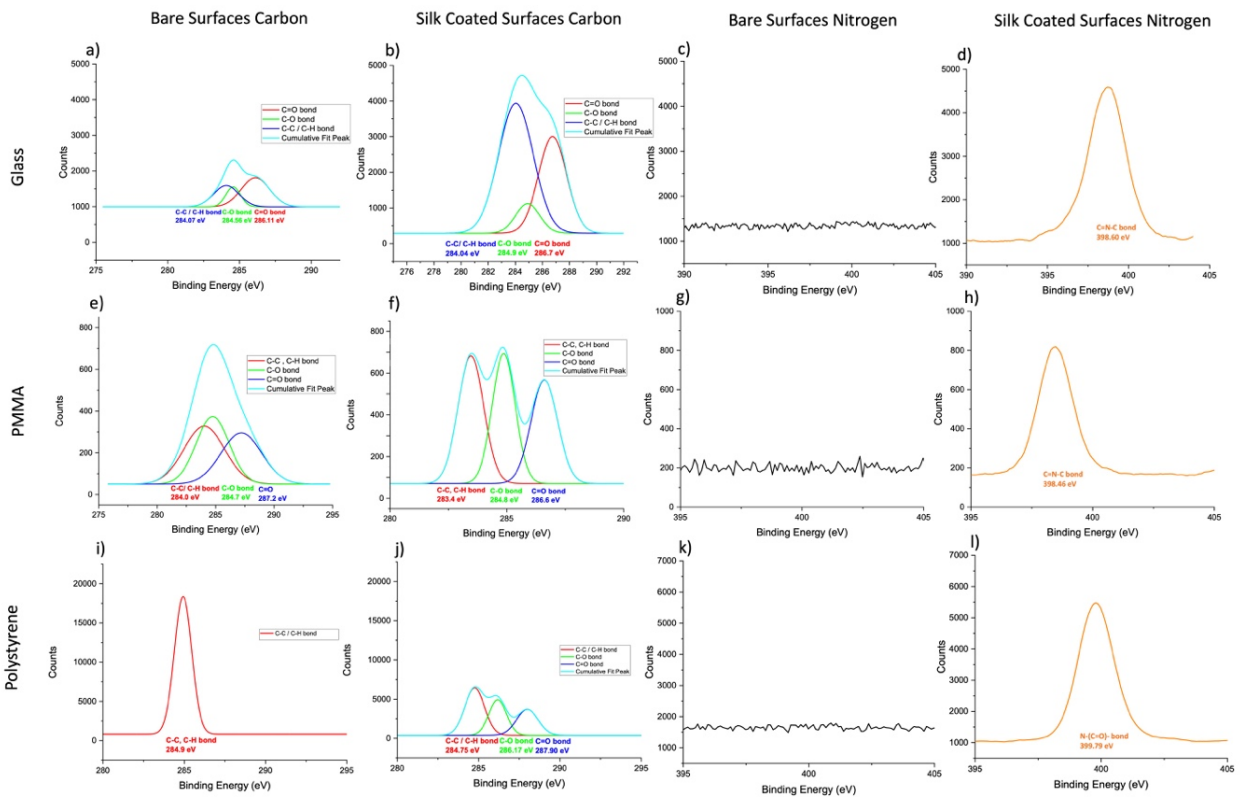


Figure 3.3. XPS characterization. C1s scans are presented for a) bare and b) SF-coated glass surface. N1s scan are shown for c) bare and d) SF-coated glass surface. For PMMA surfaces, C1s scans are represented for e) bare and f) SF-coated PMMA surfaces. N1s scans are shown for g) bare and h) SF-coated PMMA surfaces. For bare and SF coated PMMA surfaces. For polystyrene surfaces, C1s scans are presented for i) bare and j) SF-coated glass surface. N1s scan are shown for k) bare and l) SF-coated glass surface.

Although glass, PMMA and polystyrene showed similar trends as a result of the analysis, it was decided that polystyrene would be the suitable material and started to be used as the bottom layer of the microfluidic chip. One of the most important factors in this choice is that the glass has a very fragile structure. Another factor is that the main material of flasks and petri dishes used in traditional cell culture is polystyrene. One advantage of using polystyrene in cell culture is that it is non-toxic and does not interfere with cell growth or function. It also has a smooth surface that allows for the easy removal of cells and tissues, and it is resistant to most chemicals and solvents.

3.2 Cell Culturing

Cells are cultured in Static2D, Static3D, and Dynamic conditions and the culturing process continues for 7 days. During the culturing period, morphological differences of the cells were observed (Figure 3.4). Static 2D cells grow as a monolayer, while cells growing under Static 3D and Dynamic conditions are clearly visible.

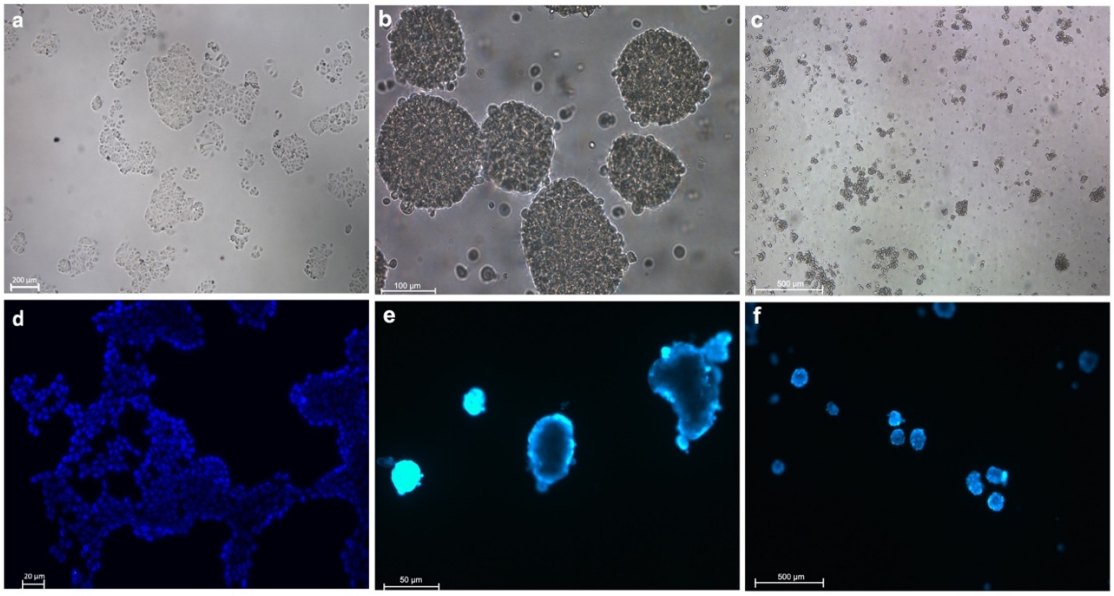


Figure 3.4. Microscopic images of MCF-7 cells cultured in static2D, static3D, and dynamic conditions. Brightfield images show monolayer of MCF-7 cells growing in (a) static2D conditions (Scale bar: 200 μm). (b) Cell images are taken under static3D

conditions (Scale bar: 100 μm). (c) Cell images are collected under dynamic conditions (Scale bar: 500 μm). Hoechst 33342-stained cells are presented in d) static2D conditions (Scale bar: 20 μm). (e) Likewise, cells are imaged under static3D conditions (Scale bar: 50 μm). (c) Cell images are collected for dynamic conditions (Scale bar: 500 μm).

At the end of 7 days, cells were disassociated from the culture flask with trypsin, and subsequently, they were counted by statining with trypan blue. As a result of counting, the final numbers of cells were noted and compared with the starting number. RNA was also isolated from these cells and its concentration was measured. After this measurement, the amount of RNA mass per cell was calculated. Table 1 summarizes the start numbers of cells, finish numbers of cells, RNA concentrations, RNA mass value, RNA mass/cell value, and how many folds they increased from beginning to the end. For cells cultured in three different conditions, the RNA mass per cell was quite close to each other (Figure 3.5a) On average, this value was 0.37, 0.33 and 0.33 for static2D, static3D and dynamic conditions, respectively (Figure 3.5b).

Table 2.Cell counts at the beginning and end of the experiment and RNA Mass values of cells grown in static2D, static3D and dynamic conditions.

	Static2D_1	Static2D_2	Static2D_3	Static2D_4	Static3D_1	Static3D_2	Static3D_3	Static3D_4	Dynamic_1	Dynamic_2	Dynamic_3	Dynamic_4
Start (Cell Number)	115000	115000	115000	115000	115000	115000	115000	115000	115000	115000	115000	115000
Finish (Cell Number)	3520000	3600000	3560000	3480000	4100000	4300000	4080000	4020000	785000	786000	758000	777000
RNA Conc (ng/ µl)	379	381	361	357	396,54	403	391,83	385,62	73,4	76,4	73,6	69,5
RNA Mass. (Cell Number x Total Volume)	1326500	1333500	1263500	1249500	1387890	1410500	1371405	1349670	256900	267400	257600	243250
RNA Mass/Cell Number	0,38	0,37	0,3549157	0,36	0,34	0,33	0,3361287	0,34	0,33	0,3402036	0,34	0,31
Final / Start	30,60869	31,304348	30,956522	30,260869	35,652173	37,391304	35,478261	34,956521	6,8260869	6,8347826	6,5913043	6,7565217

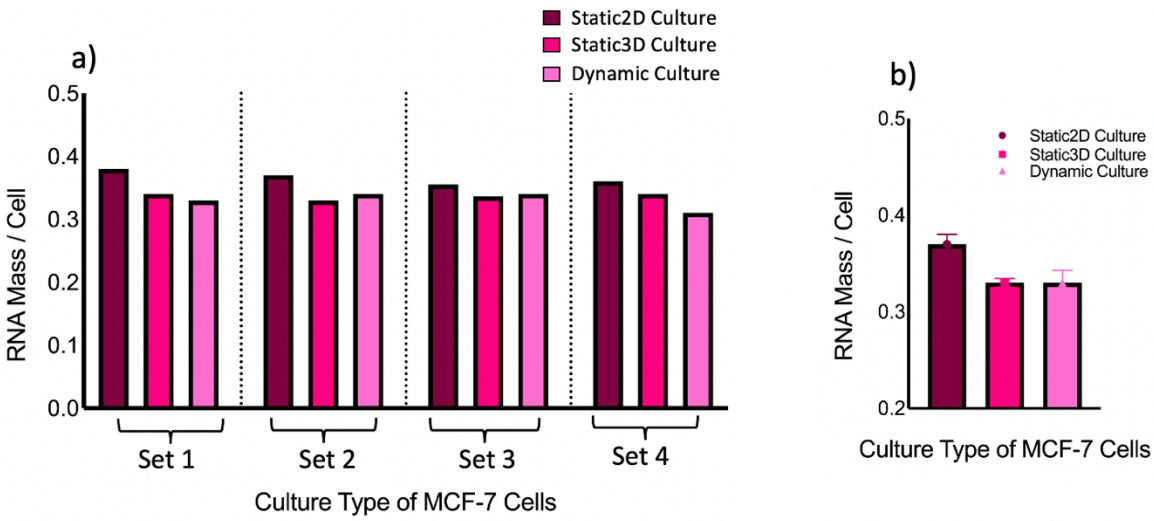


Figure 3.5. a) RNA mass/cell plot was obtained from cells cultured under three different conditions. b) Average of RNA mass/cell values were presented for static2D, static3D, and dynamic conditions.

In order to perform gene expression analysis, cDNA synthesis was carried out using RNA samples. Agarose gel electrophoresis was performed to confirm cDNA synthesis and primers. In the results, there was no problem faced in the primers, and that cDNA was synthesized successfully from the samples derived from three different culturing groups (Figure 3.6).

Table 3.cDNA concentrations of Static2D, Static3D and Dynamic conditions were measured by Qubit Fluorometer.

	1st Set (ng/µL)	**2nd Set (ng/µL)**	**3rd Set (ng/µL)**	**4th Set (ng/µL)**
Static2D	1332.8	1368.6	1338.1	1343.6
Static3D	1392.2	1388.5	1360.9	1355.7
Dynamic	1300.8	1312.0	1370.2	1330.8

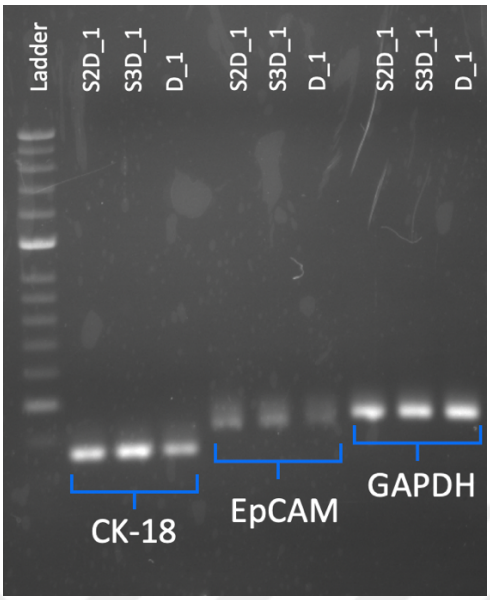


Figure 3.6. Gel images for cDNAs (*CK-18, EpCAM,* and *GAPDH* genes) collected from static2D, static3D, and dynamic conditions were presented.

3.3 Gene Expression Analysis

Finally, we performed the qRT-PCR analysis in order to evaluate whether there was a change in gene expression of the cells under different conditions. The genes investigated in this section were *EpCAM* and *CK-18* genes. EpCAM (epithelial cell adhesion molecule) is a transmembrane protein that plays a key role in the development and maintenance of epithelial tissue [125]. It is expressed on the surface of many types of cancer cells and is used as a marker for cancer diagnosis and treatment. EpCAM has also been implicated in the regulation of cancer stem cells (CSCs) and CSCs with a greater expression of *EpCAM* are considered to be more prone to metastasis [126]. *CK-18* gene produces cytokeratin-18 protein, which is found in various tissues and organs throughout the body. It is crucial for maintaining the structure and function of these tissues [127]. Abnormalities in the *CK-18* gene possibly lead to a range of health problems, including cancer and other diseases [128]. *CK-18* has been shown to be involved in the regulation of the E-cadherin protein, which helps to maintain the integrity of epithelial tissues. Changes in the expression of *CK-18* is thought to contribute to the ability of cancer cells to invade and spread throughout the body [129]. These two genes are highly expressed in

MCF-7 cancer cells and play an important role in the epithelial-mesenchymal transition (EMT). Epithelial-mesenchymal transition (EMT) is a developmental process that takes place throughout embryogenesis is characterized by the loss of epithelial cell features and the development of mesenchymal cell properties [126]. During EMT, cells lose their polarity and their ability to adhere to neighboring cells, and gain the ability to migrate and differentiate into various cell types. EMT has been shown to play a role in tissue repair, wound healing, and cancer metastasis [130]. In cancer, EMT can enable EMT can facilitate the detachment of cancer cells from the primary tumor and their migration to different areas of the body, leading to the development of metastases [131]. Researchers are working to better understand the signaling pathways and transcriptional regulators that drive EMT in order to develop therapies that target EMT in cancer and other diseases.

The results of qRT-PCR analysis through RNAs collected from cells cultured in static2D, static3D, and dynamic conditions were statistically analyzed using two-way ANOVA test, and there was no significant difference observed per the analysis. Although it was not significant, *EpCAM* expression was higher in cells grown in dynamic culture compared to the other counterparts (Figure 3.7). When assessing the levels of CK-18 gene expression, we did not observe any statistically difference per two-way ANOVA test. On the other hand, *CK-18* expression results from dynamic culture were lower than those derived from static conditions (Figure 3.7). Compared to static conditions, *CK-18* expression decreased while *EpCAM* expression increased in dynamic conditions. In a report in the literature, *CK-18* downregulation causes *EpCAM* upregulation in breast cancer, which induces EMT and stemness [126], and we herein observed the similar trend as reported.

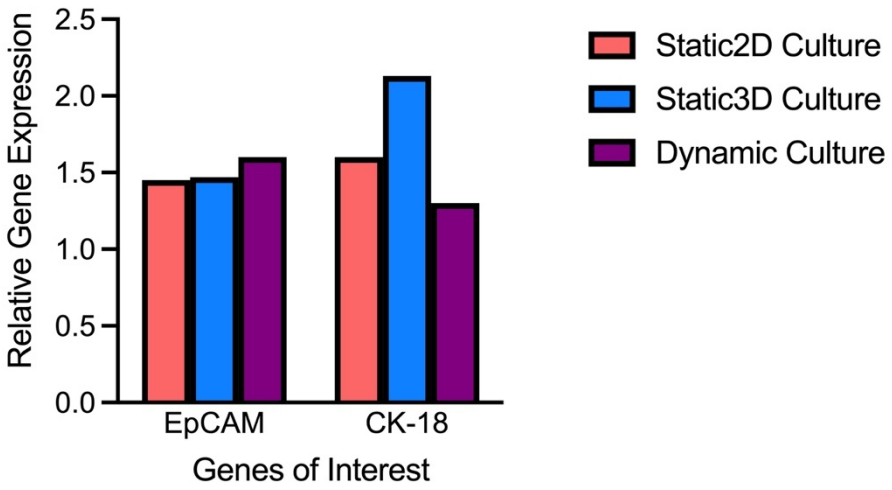


Figure 3.7. Analysis of the expression levels of *EpCAM* and *CK-18* genes under different conditions by qRT-PCR (*GAPDH* gene is used as an endogenous control).

CHAPTER 4

4.CHEMORESISTANCE STUDIES

It was desired to investigate whether MCF-7 cells would acquire resistance to anti-cancer drugs in the face of fluid shear stress and under 3D environment. For this reason, anti-cancer drugs, i.e., doxorubicin and docetaxel, were chosen for this study. Briefly, doxorubicin is a member of anthracyclines drugs, and it is frequently used to treat several cancers including breast, ovarian, lung, and thyroid [132]. Doxorubicin plays vital roles in two distinct pathways on cancer cells: (i) DNA intercalation, which prevents topoisomerase-II from carrying out DNA repair, and (ii) production of free radicals, which leads to destruct cellular membranes, proteins, and DNA [132]. Docetaxel, on the other hand, is a member of taxane neoplastic drugs, having cytotoxic effect and significant therapeutic performance against a variety of cancers, including ovarian cancer, breast cancer, and lung cancer [133]. Docetaxel is able to stimulate tubulin molecule polymerization and block depolymerization, resulting in mitotic cell arrest of the cell cycle and consequently, inducing apoptosis. Additionally, it can cause cell death through apoptosis by promoting the phosphorylation of BCL-2 [134].

In this section, cells were cultured in three different conditions as detailed in the previous section, i.e., static2D, static3D, and dynamic conditions. On the fourth day after culturing, four different doses (10^5 nM, 10^3 nM, 10 nM, and 0.1 nM) of two different anti-cancer drugs (doxorubicin and docetaxel) were introduced to cells. The experiment was finalized at 72 hours after drug administration and cells were counted by staining with trypan blue. Cell viability ratio was determined by calculating alive and dead cell numbers. At the same time, RNA was isolated from the cultured cells, and subsequently, cDNA synthesis was performed.

4.1 Doxorubicin Studies for Static2D, Static3D and Dynamic Conditions

In this section, cells cultured in static2D, static3D and dynamic conditions were treated with four different doses (10^5 nM, 10^3 nM, 10 nM, and 0.1 nM) of doxorubicin on the 4th day after culturing. After the drug experiment that lasted for 72 hours, the experiment was terminated. The cells were removed from the surface, and then, the viable/dead numbers were calculated with trypan blue. According to the results, the cell number and viability graph for different doses are depicted in Figure 4.1 for the static2D condition. No drug was applied to the control group. Per the results, the number of viable cells decreased in proportional to the dose increments. At the highest dose of 10^5 nM, the number of live cells was almost equal to the number of dead cells (Figure 4.1a). Moreover, there was an average of 83% viability in the control group, while this rate decreased to 80%, 73%, 62% and 52% for the drug doses of 10^5 nM, 10^3 nM, 10 nM, and 0.1 nM, respectively (Figure 4.1b).

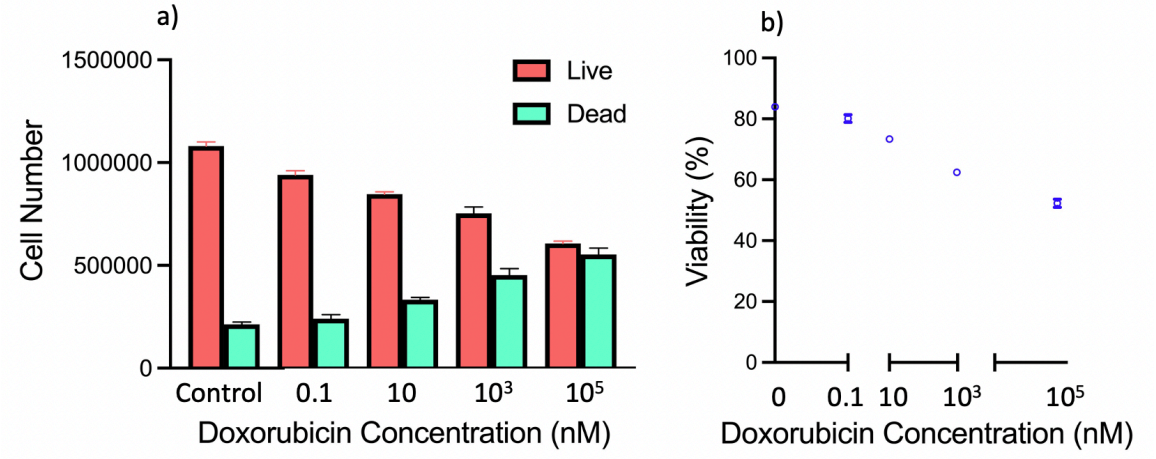


Figure 4.1. Doxorubicin treatment results for static2D condition are presented. a) The number of live/dead cells for control group and four different doses at the end of the experiment are demonstrated. b) The viability rate is obtained for control group, 0.1 nM, 10 nM, 10^3 nM, and 10^5 nM of doxorubicin.

When the cells in this experimental group were examined under the microscope, it was observed that the 0.1 nM and 10 nM doses were not structurally different from the

control group (Figure 4.2). On the other hand, it was easy to observe that the monolayer structures of cells treated with the 10^3 nM dose were disrupted shown in Figure 4.2. At the highest dose of 10^5 nM, dead cells could be distinguished from normal cells by differences in morphological structure. In addition, live cells were stained green with calcein A, whereas dead cells were stained red with ethidium homodimer-1 per the assay of live/dead. In these results, while the cells in the control group were mostly stained with green, the cells treated with 10^5 nM doxorubicin had a higher density of cells stained with red, pointing out high number of dead cells.

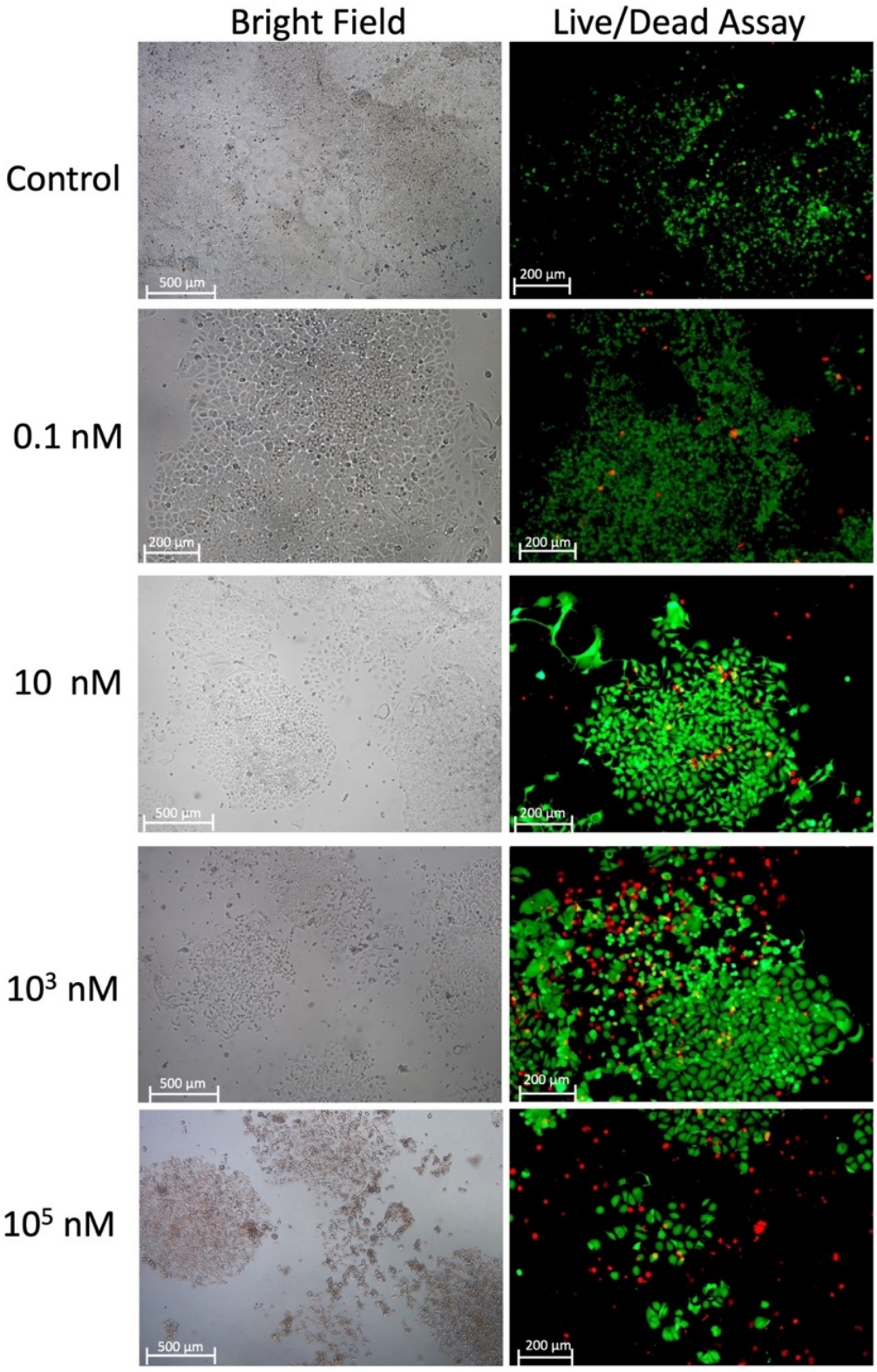


Figure 4.2. Static2D images of control group and cells treated with 0.1 nM, 10 nM, 10^3 nM, and 10^5 nM of doxorubicin under brightfield and fluorescent as a result of live/dead assay.

Evaluating the results from the doxorubicin applied to cells grown in static3D environment, we observed that the number of live cells decreased and the number of dead increased, similar to static2D condition (Figure 4.3a). In this experimental group, the viability rate starts with 85% for the control group, decreases to 82% for 0.1 nM, 75% for 10 nM, 65% for 10^3 nM, and finally to 61% for 10^5 nM of doxorubicin (Figure 4.3b).

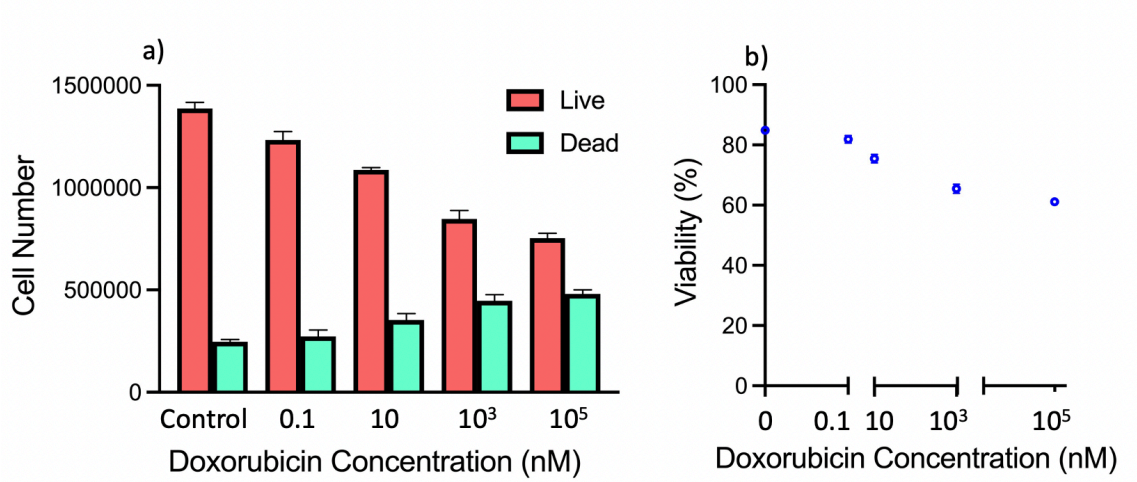


Figure 4.3. Doxorubicin treatment results for static3D condition are presented. a) The live/dead cells number for all experimental groups is shown. b) The viability percentages for control group and each dose are plotted.

As the drug dose was increased in cells cultured under static3D conditions, deterioration in the 3D structure was observed (Figure 4.4). While these deteriorations occurred mostly in the outer layer of the cells in 3D state, the cells that remained intact (seen in yellow color) on the inner side were less affected by the drugs.

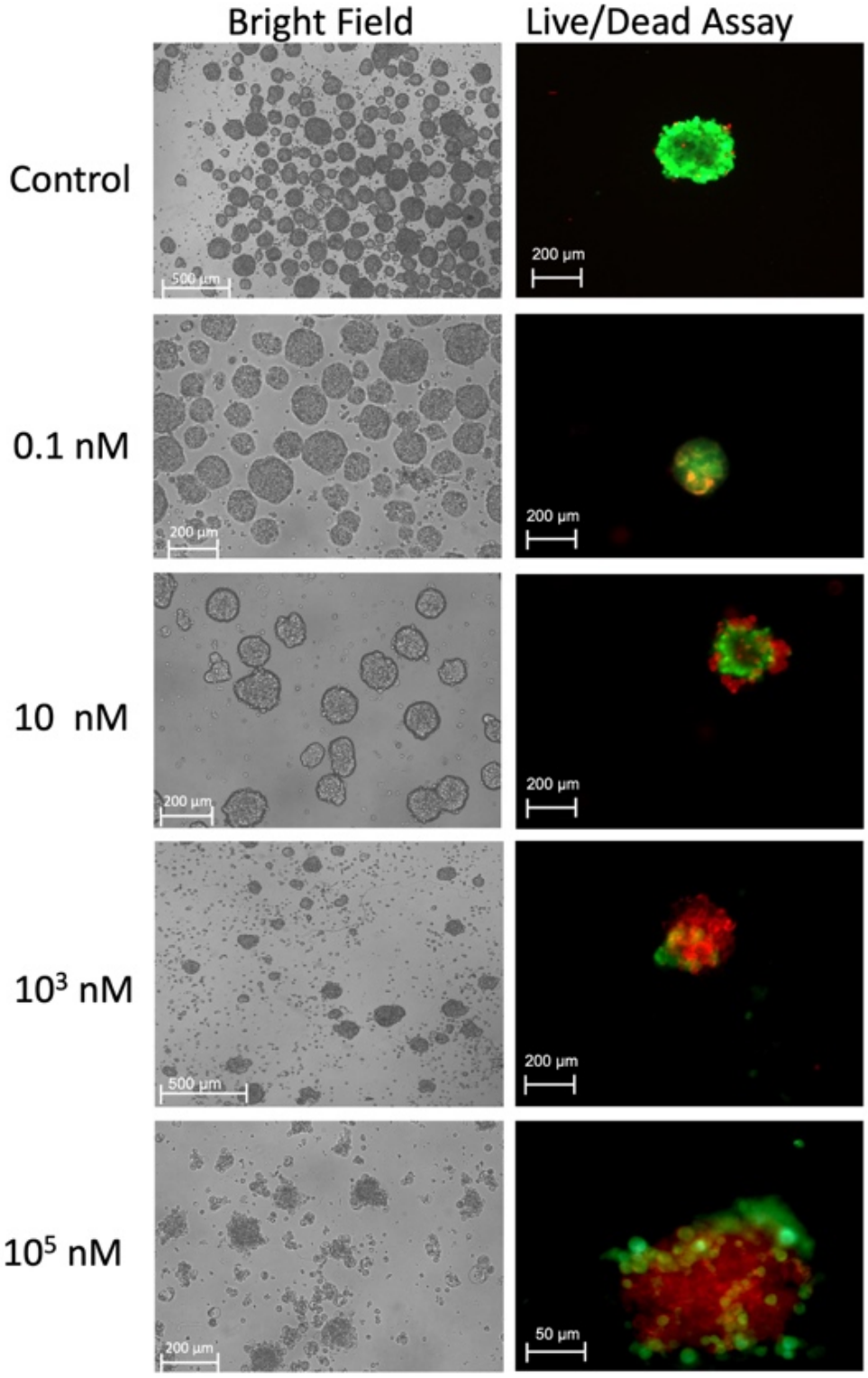


Figure 4.4. Brightfield images of static3D condition show control group and cells treated with 0.1 nM, 10 nM, 10^3 nM, and 10^5 nM of doxorubicin and fluorescent as a result of live/dead assay

On the other hand, MCF-7 cells cultured in dynamic condition in microfluidic chips were collected for live/dead count at the end of the 7-day experiment period. Unlike static conditions, the number of cells obtained in dynamic conditions was approximately 3-4 times less (Figure 4.5a). This was because cells cultured under static conditions had an area of 25 cm^2, while cells cultured under dynamic conditions had an area of 6 cm^2 (4 times less surface area). Similar to the viability results in static2D and static3D conditions, the number of live cells in dynamic conditions decreased in proportional to the increments of drug doses (Figure 4.5a). In fact, unlike static conditions, when the highest dose of 10^5 nM of doxorubicin was applied to the cells, the viability rate in dynamic conditions decreased down to ~ 40% (Figure 4.5b).

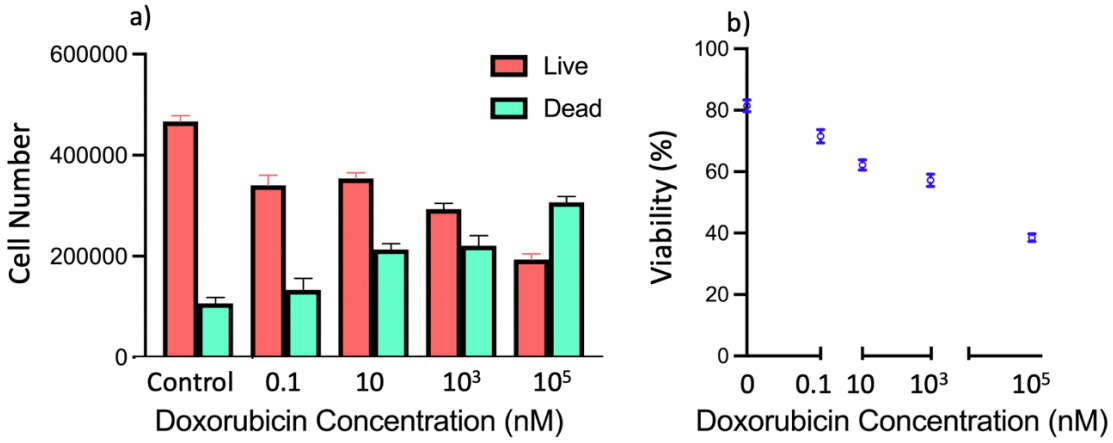


Figure 4.5. The effects of doxorubicin on dynamic condition are presented. a) The live/dead cells number for all experimental groups is shown. b) The viability percentages for control group and each dose are plotted.

In the cells cultured under dynamic conditions in microfluidic chips, shrinkage in the 3D structure was observed as the drug dose increased (Figure 4.6). Structural disruption observed in static3D cells was not realized in the dynamic environment. Cells that died on the 3D surface were removed by flow, and consequently, the cells kept their shape and shrunk. This observation was crucial to understand the shear effect in drug experiments. Through these systems, the drug was able to penetrate more cells and have a higher mortality rate.

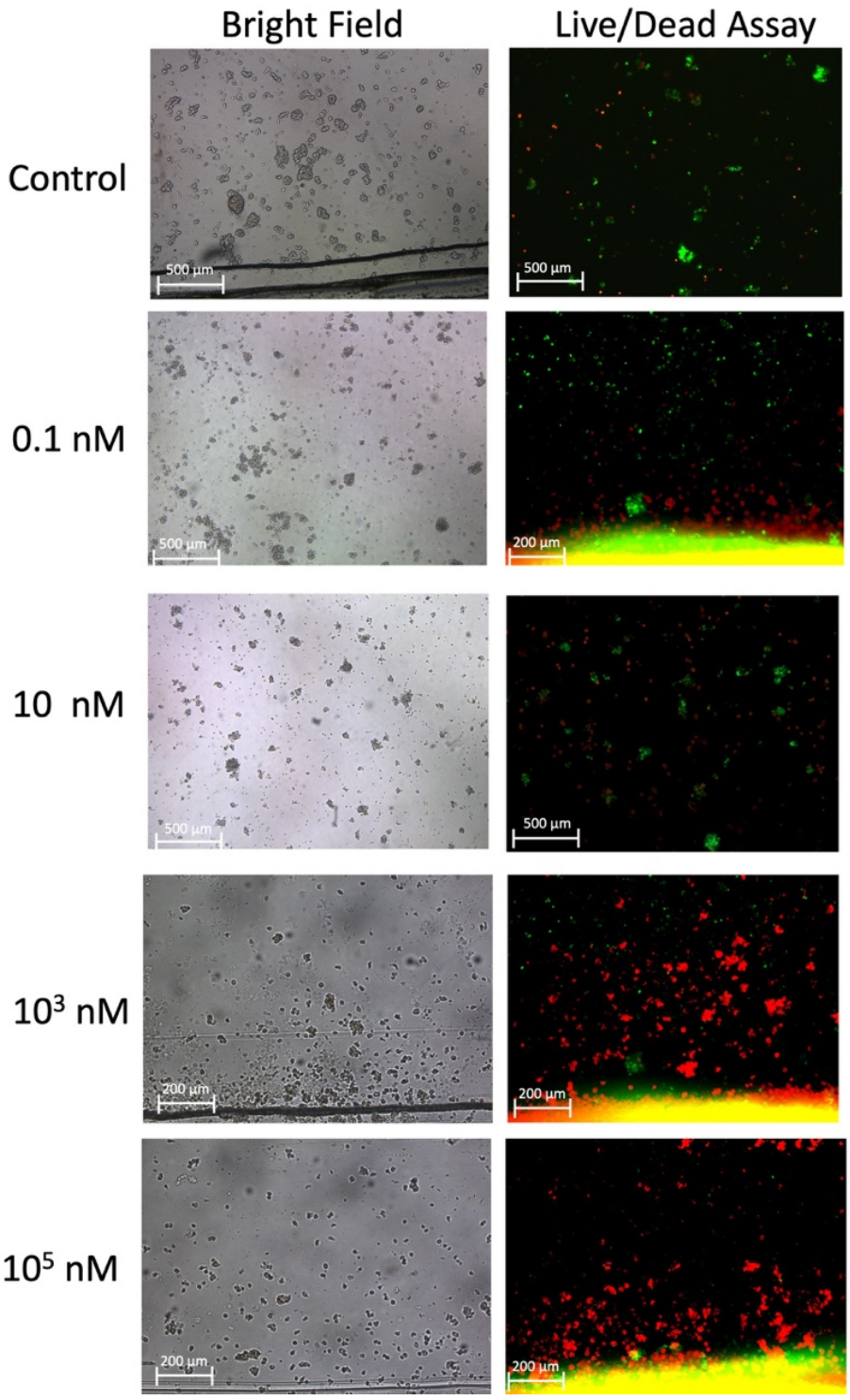


Figure 4.6. Brightfield images and live/dead assay result of control group and cells treated with 0.1 nM, 10 nM, 10^3 nM, and 10^5 nM of doxorubicin obtained from dynamic conditions

While comparing the viability results in three different conditions, the most effective system in reducing cell viability in proportional the increments of drug doses was the dynamic condition, possibly due to the flow condition on this platform (Figure 4.7). The cells in the outermost layer of the cells in the 3D structure interacted with anti-cancer drugs applied through flow, and lost their vitality. Dead cells were continuously removed from the microchannels by the flow, and the other living cells on the surface of the 3D structure were also affected by the drug in the flow. Second,, the viability rate of cells grown in static2D condition was lower than those cultured in static3D condition. Cells in a monolayer state in a static2D environment lost their vitality by interacting with the drug applied to them. Finally, the viability of cells in static3D conditions decreased as the drug dose increased; however, according to ordinary one-way ANOVA test, this decrease was not significant in static2D and dynamic environments. In addition, the cells in the outer layer of the cells in the 3D structure in the static environment were affected by the drug, while the cells in the compact form on the inside did not receive the drug significantly. Therefore, alive cells remaining in the 3D structure would possibly lead to a high rate of viability.

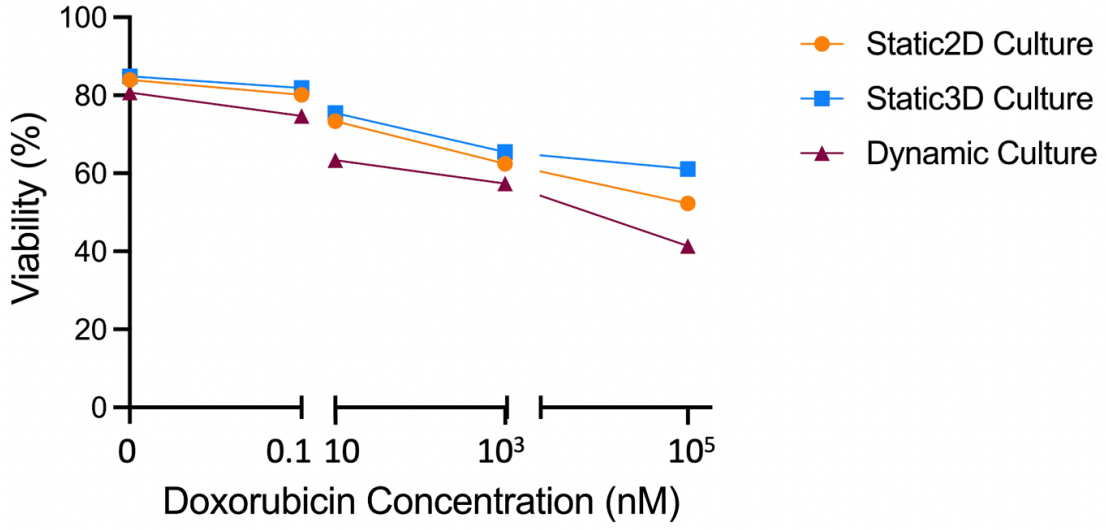


Figure 4.7. Combined cell viability rate plot from static2D, static3D and dynamic conditions for doxorubicin treatment.

Subsequently, RNA was isolated from the cells from these drug experiments. The RNA concentrations were measured using the Qubit Fluorometer instrument, and the

resulst were stated in Table 3. To perform gene expression analysis, the isolated RNA needs to be translated into cDNA. In this experiment, cDNA synthesis was performed using 100 ng of RNA from each sample. To confirm cDNA synthesis, PCR was performed using *MDR-1, BCRP and GAPDH* genes, resulting in cDNA bands visualized on agarose gel (Figure 4.8).

Table 4.RNA concentrations of Doxorubicin (Dox) treated cells.

		1st Set (ng/µL)	**2nd Set (ng/µL)**	**3rd Set (ng/µL)**
Static2D	Control Group	361	386	358
	0.1 nM Dox	327	343	310
	10 nM Dox	294	292	285
	10^3 nM Dox	244	236	232
	10^5 nM Dox	185	197	190
Static3D	Control Group	408	419	394
	0.1 nM Dox	388	396	383
	10 nM Dox	324	315	320
	10^3 nM Dox	273	281	264
	10^5 nM Dox	206	213	218
Dynamic	Control Group	96	94	93
	0.1 nM Dox	85	85	88
	10 nM Dox	71	76	70
	10^3 nM Dox	62	70	67
	10^5 nM Dox	52	58	54

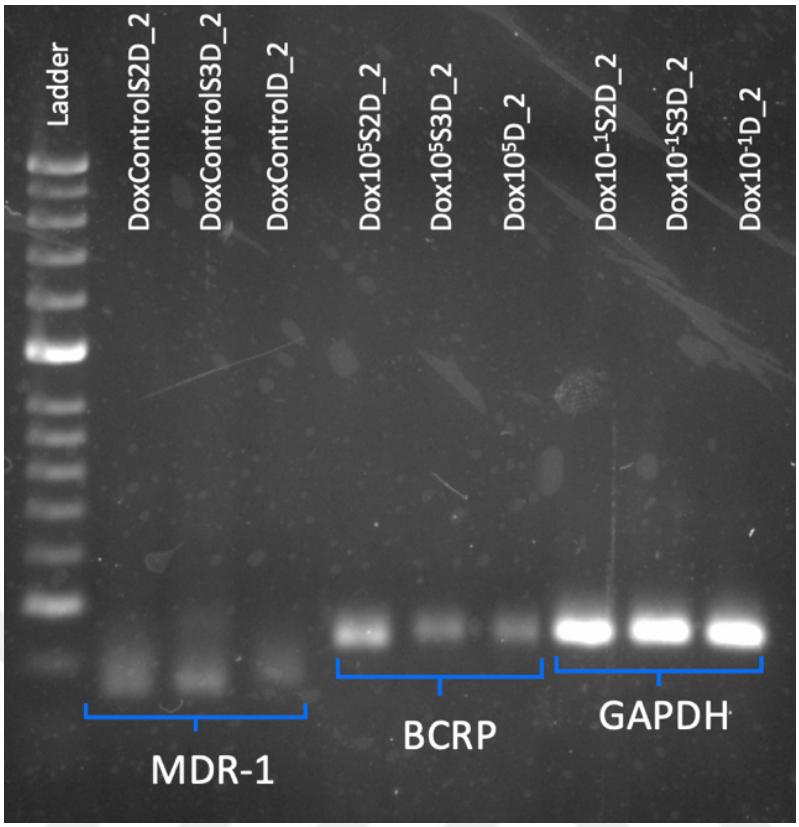


Figure 4.8. Gel images for cDNAs (*MDR-1, BCRP* and *GAPDH* genes) collected from static2D, static3D and dynamic conditions.

4.2 Docetaxel Studies for Static2D, Static3D and Dynamic Conditions

Herein, instead of doxorubicin, docetaxel was used as the anti-cancer. The cells were cultured in staticc2D, static3D, and dynamic conditions, and drug administration was started on the 4th day. Likewise in doxorubicin, there was a control group (no drug applied), and drug groups (0.1 nM, 10 nM, 10^3 nM, and 10^5 nM doses of docetaxel). In cells growing under static 2D conditions, the reduction in alive cell count with increasing docetaxel doses had a similar trend with doxorubicin (Figure 4.9a). The viability rate of the experimental group, which started with 84%, and then, decreased to 55% when the highest dose of drug was applied (Figure 4.9b).

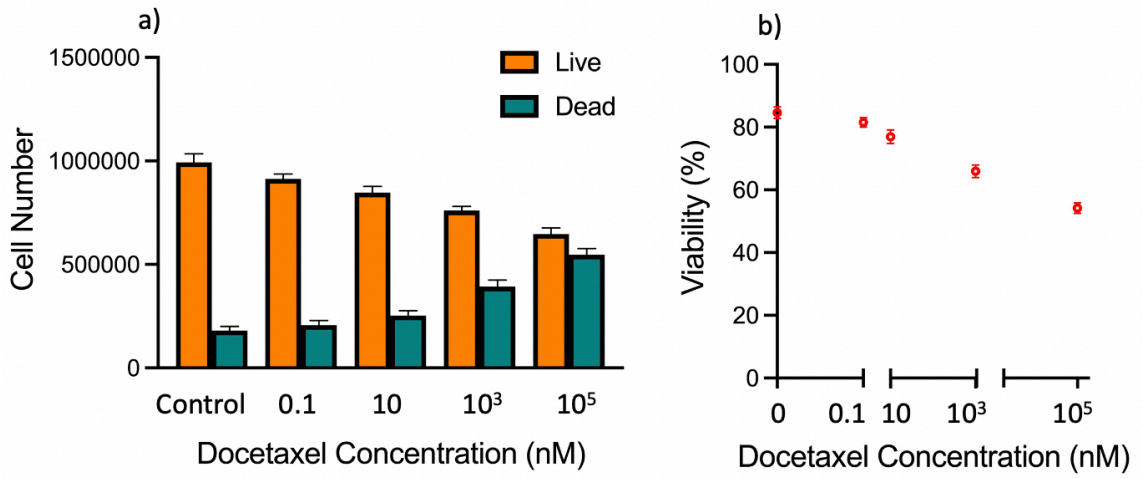


Figure 4.9. The effects of docetaxel on static2D condition are presented. a) The live/dead cells number for all experimental groups is shown. b) The viability percentages for control group and each dose are plotted.

When the cells were examined with the microscope, it was observed that the structure of the 0.1 and 10 nM doses was similar to the control group (Figure 4.10). After administration of 10^3 nM of docetaxel, the cells started to die to a large extent, and at the 10^5 nM of drug dose, almost all cells were dead (Figure 4.10). Contrary to the monolayer structure, the cells were in a clumped state at 10^3 and 10^5 nM of doses and the intercellular interaction was reduced greatly.

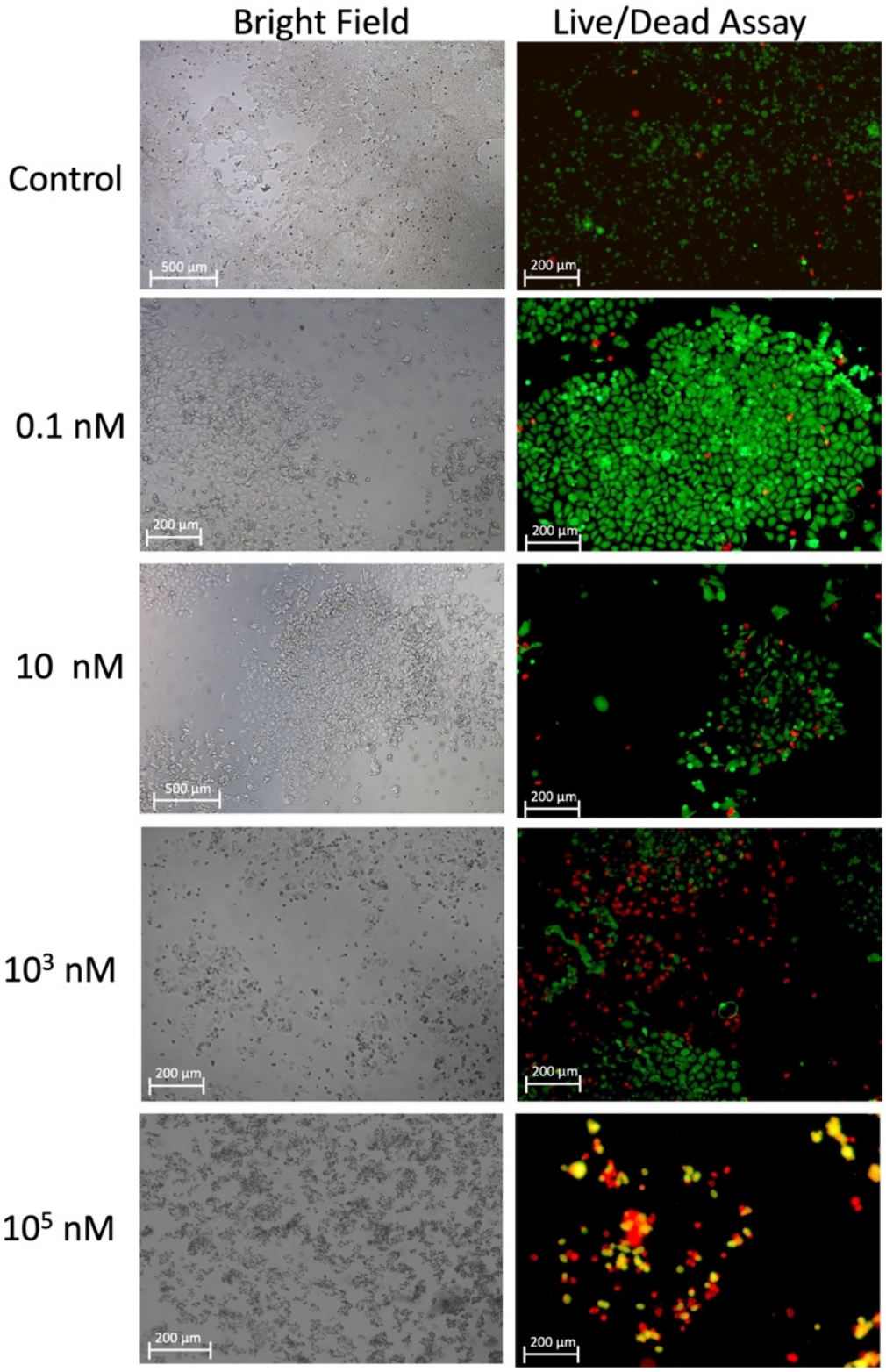


Figure 4.10. Images of control group and cells treated with 0.1 nM, 10 nM, 10^3 nM, and 10^5 nM doses of docetaxel are demonstrated under brightfield and fluorescence imaging as a result of live/dead assay for static2D condition.

Cells grown in static3D conditions showed a decrease in viability against increasing drug dose, as in static2D (Figure 4.11a). The viability rate, which started with 83% in the control group that was not given the drug, decreased to 62% when the highest dose of docetaxel was given (Figure 4.11b).

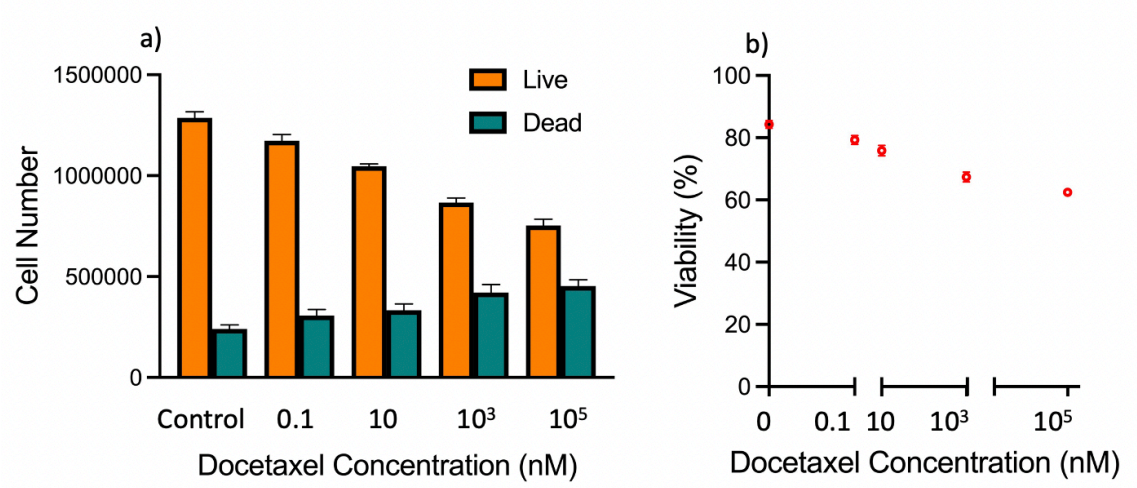


Figure 4.11. The effects of docetaxel on static3D condition are presented. a) The live/dead cells number for all experimental groups is shown. b) The viability percentages for control group and each dose are plotted.

In the cell groups cultured in Static 3D conditions treated with docetaxel, the 3D structure deteriorated as the drug dose increased. These deteriorations have occurred especially due to dead cells in the outer layer (Figure 4.12).

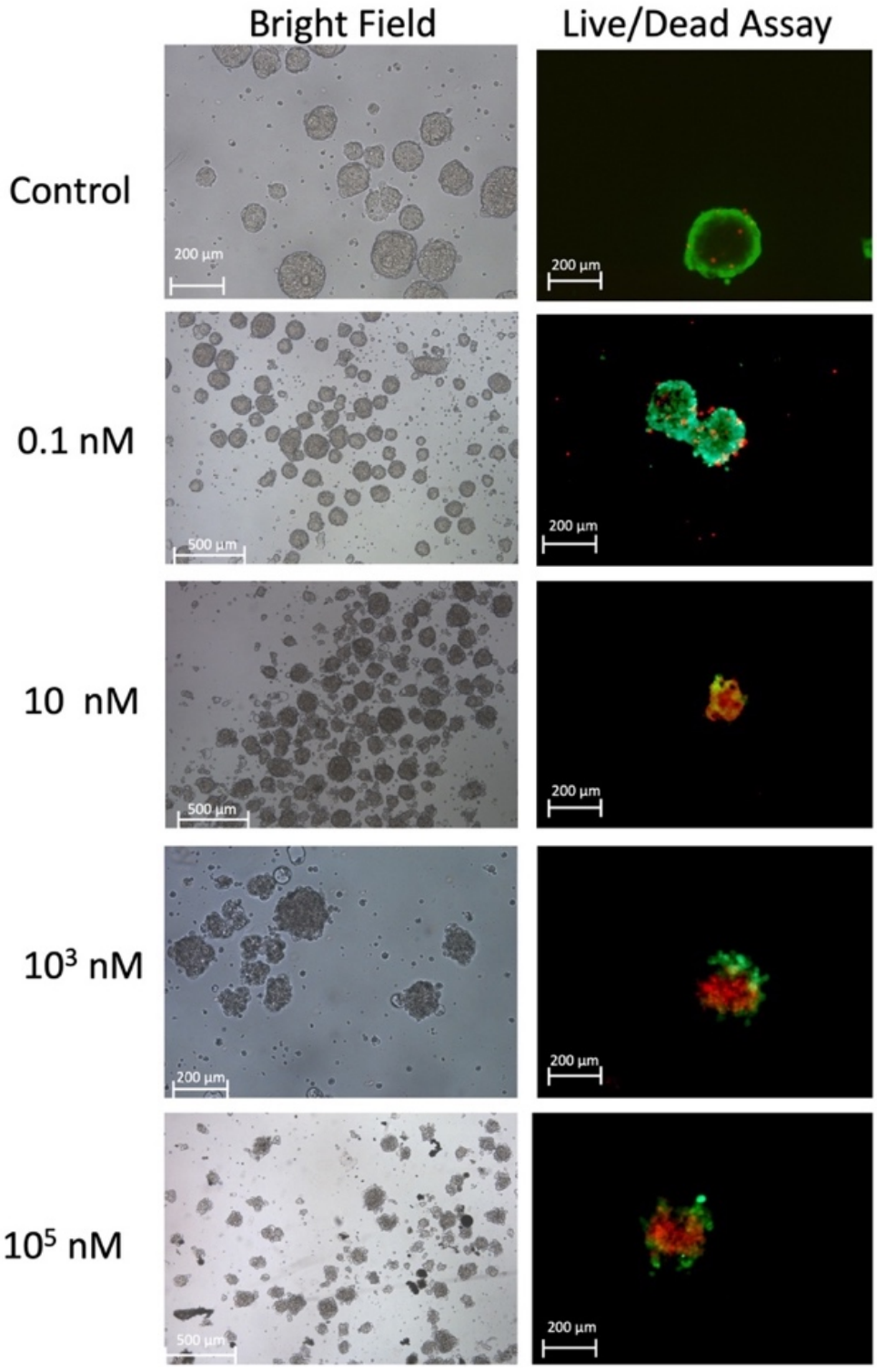


Figure 4.12 Images of control group and cells treated with 0.1 nM, 10 nM, 10^3 nM, and 10^5 nM doses of docetaxel are demonstrated under brightfield and fluorescence imaging as a result of live/dead assay for static3D condition.

Evaluating the result of docetaxel experiment performed under dynamic conditions, there was no significant difference between the control group and the 0.1 nM of the drug dose in terms of the number of live/dead cells (Figure 4.13a). The trend of increasing dead cell count as the dose increments was similar to these conditions. Unlike static conditions, the viability rate obtained at the highest dose was ~43% (Figure 4.13b). As stated in the section of doxorubicin experiments, the flow in microfluidic chips increased the number of dead, potentially enabling the drug to interact more cells.

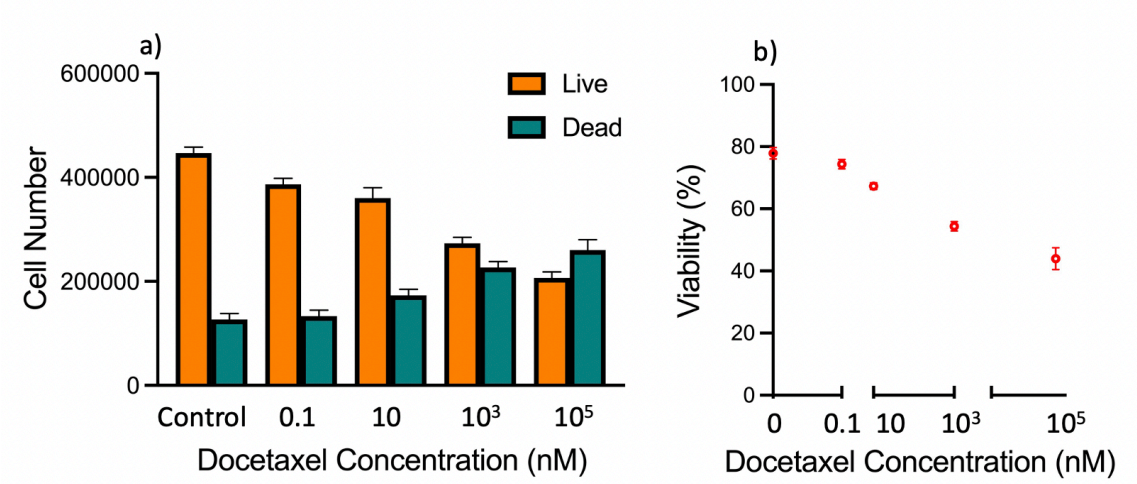


Figure 4.13. The effects of docetaxel on dynamic condition are presented. a) The live/dead cells number for all experimental groups is shown. b) The viability percentages for control group and each dose are plotted.

When the cells obtained from the dynamic condition treated with docetaxel were examined under the microscope, similar trend in doxorubicin was observed here as well. When the drug dose was increased, shrinkage was realized in these 3D structures (Figure 4.14).

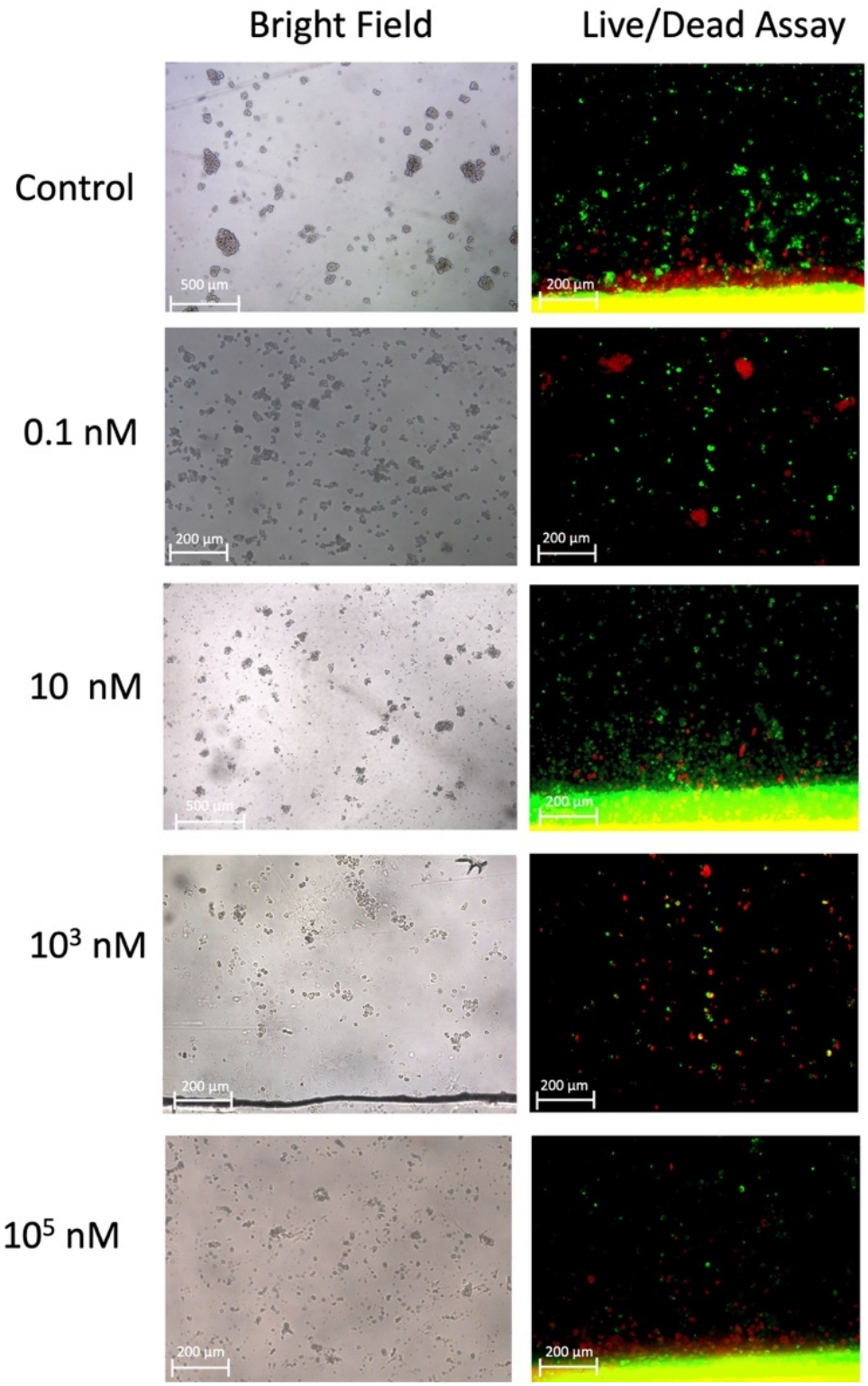


Figure 4.14. Images of control group and cells treated with 0.1 nM, 10 nM, 10^3 nM, and 10^5 nM doses of docetaxel are demonstrated under brightfield and fluorescence imaging as a result of live/dead assay for dynamic condition.

When the viability rates obtained as a result of each condition were combined in a single plot, it was clear that the viability rate of the cells grown in dynamic culture was lower as the drug dose increased (Figure 4.15). As noted earlier, the flow in dynamic conditioning was the main reason of the significantly reduced vitality rate. The response of cells grown in static3D condition to drugs was lower than in other situations.

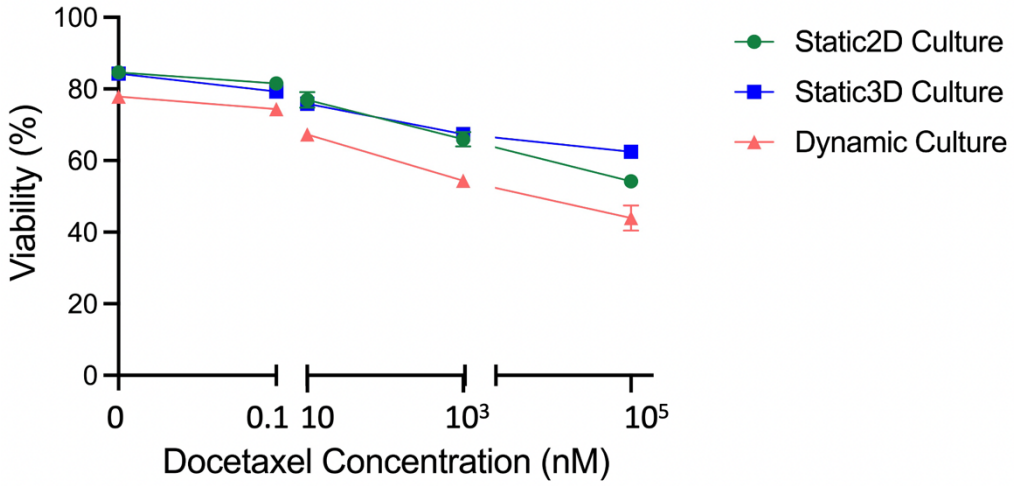


Figure 4.15. Combined cell viability rate plot from static2D, static3D and dynamic conditions for docetaxel treatment.

Likewise, at the end of the docetaxel experiments, RNA isolation was performed from the cells (Table 4.). This step was followed by cDNA synthesis, and cDNAs were amplified by PCR using primers suitable for *MDR-1, BCRP* and *GAPDH* genes. The PCR products were analyzed on agarose gel, and there was no problem in cDNA synthesis (Figure 4.16).

Table 5.RNA concentrations of Docetaxel (Doc) treated cells.

		1st Set (ng/µL)	2nd Set (ng/µL)	3rd Set (ng/µL)
Static2D	Control Group	383	380	367
	0.1 nM Doc	346	352	338
	10 nM Doc	305	314	307
	10^3 nM Doc	250	249	255
	10^5 nM Doc	196	202	211
Static3D	Control Group	417	406	421
	0.1 nM Doc	394	385	379
	10 nM Doc	322	327	334
	10^3 nM Doc	286	292	271
	10^5 nM Doc	238	243	232
Dynamic	Control Group	102	97	105
	0.1 nM Doc	88	91	90
	10 nM Doc	78	78	82
	10^3 nM Doc	63	72	70
	10^5 nM Doc	54	52	55

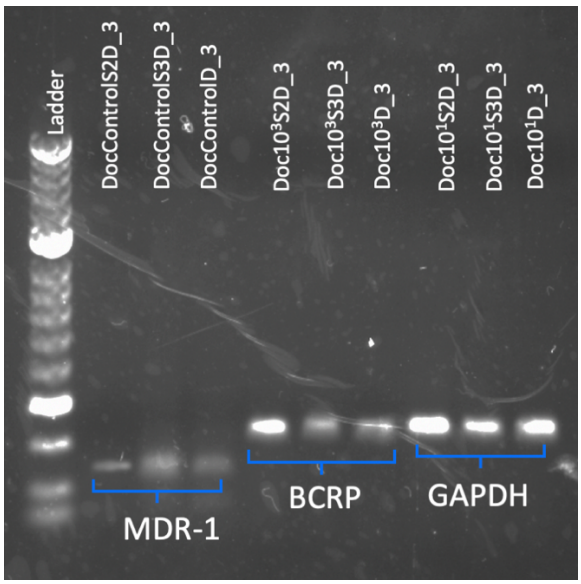


Figure 4.16 Gel images for cDNAs (*MDR-1, BCRP* and *GAPDH* genes) collected from static2D, static3D and dynamic conditions.

4.3 Gene Expression Analysis

The effects of flow on gene expression in microfluidic chip systems were investigated in the Chapter 3. In this section, we investigated whether cells cultured in microfluidic systems developed any resistance to anti-cancer drugs after the drug experiments. In addition to the *EpCAM* and CK-18 genes, the expression levels of *MDR-1* and *BCRP* genes were analyzed in this section. Briefly, *MDR1* gene encodes a protein called P-glycoprotein that is responsible for transporting a variety of substances across cell membranes [135]. This protein plays a key role in the body's defense against toxins and drugs, and variations in *MDR1* gene can affect an individual's susceptibility to certain medications. Individuals with certain MDR1 gene variations may be at high risk for adverse drug reactions, while other individuals without MDR1 gene variations may experience reduced efficacy of certain drugs, means that they may acquire drug resistance [136]. The *MDR1* gene has also been linked to certain diseases, including cancer [137]. Research into *MDR1* gene and its role in drug metabolism and disease is ongoing and understanding *MDR1* gene effect on an individual's response to medications and diseases may help improve treatment and prevention strategies. On the other hand, *BCRP* gene encodes a protein called breast cancer resistance protein, and it has a role as ATP-binding cassette (ABC) transporter which is established a cause of multi-drug resistance in cancer [138]. BCRP plays a role in the body's defense system by helping to remove toxins and harmful substances from the gut, bile, blood-brain barrier, placental barrier, and possibly the blood-testis barrier [138]. It also helps to eliminate certain cancer drugs from the body, which can make cancer cells resistant to treatment. In addition, BCRP is present in stem cells, and may be related to the ability of cancer cells to resist treatment, regenerate, and become more aggressive [139]. Therefore, targeting *BCRP* may be a useful strategy for improving cancer treatment outcomes.

4.3.1 Doxorubicin Gene Expression

After doxorubicin assays were finalized for static2D, static3D and dynamic conditions, cells were used for gene expression analysis. In this section, *CK-18, EpCAM, MDR-1* and *BCRP* gene expressions were analyzed (Figure 4.17). *GAPDH* was used as

the endogenous gene. Figure 4.17a shows the *CK-18* gene expression of the control group and four different doses of doxorubicin treated groups. No specific trend was observed for gene expression analysis performed for static2D conditions. Expression level decreased when 0.1 nM doxorubicin was given, but increased at 10 nM doxorubicin dose. In addition, *CK-18* gene expression decreased as the drug dose increased after 0.1 nM of drug dose for the dynamic condition. We observed the same trend in the static3D condition (Figure 4.17a). For *EpCAM* gene expression analysis, no change was observed in the control and doxorubicin-treated groups for the static2D condition (Figure 4.17b). On the other hand, in the static 3D condition, no difference was observed up to the 10 nM of doxorubicin, while *EpCAM* expression increased gradually in the 10^3 nM and 10^5 nM dose of doxorubicin. Finally, when the dynamic conditions were examined, there was no gene expression level difference in the control group and 0.1 nM doxorubicin group, but a gradual increase in *EpCAM* expression was found from 10 nM dose of doxorubicin to 10^3 nM and 10^5 nM doses (Figure 4.17b). The genes that would show whether cells had acquired resistance to anti-cancer drugs were *MDR-1* and *BCRP* genes. While there was no obvious difference in *MDR-1* gene expression for static2D and static3D conditions, gene expression started to increase in the group given 0.1 nM dose of doxorubicin for dynamic conditions. This increase continued at the 10 nM dose. At 10^3 nM and 10^5 nM doses, approximately 2 times more *MDR-1* was expressed compared to the control group (Figure 4.17c). Finally, Figure 4.17d shows the *BCRP* gene expression results. When 0.1 nM dose of doxorubicin was given under static2D conditions, an increase in gene expression was observed compared to the control. On the other hand, there was a stable trend for static3D conditions up to 10^3 nM dose of doxorubicin, whereas *BCRP* gene expression increased when 10^3 nM dose of doxorubicin was given. However, when the 10^5 nM doxorubicin was examined, it was observed that the expression level decreased. Lastly, there was an increase in *BCRP* gene expression of dynamic conditions after 10 nM dose of doxorubicin was introduced.

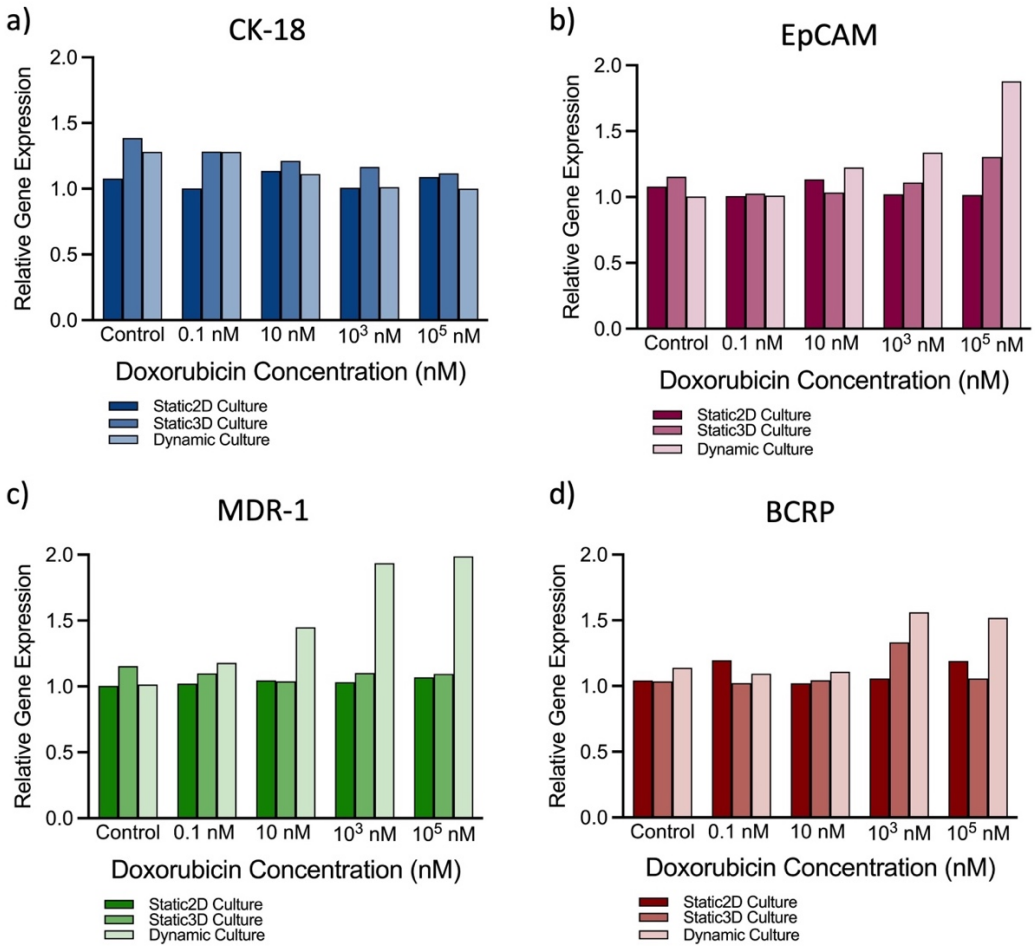


Figure 4.17 Gene expression analysis for *CK-18, EpCAM, MDR-1,* and *BCRP* is demonstrated on the course of doxorubicin treatment.

4.3.2 Docetaxel Gene Expression

Docetaxel was used as the second anti-cancer drug in the study. Likewise, the expression of four genes under different conditions was examined in docetaxel treatment (Figure 4.18). Firstly, *CK-18* gene expression was analyzed (Figure 4.18a). Cells grown in static2D conditions exhibited no changes in the expression of *CK-18* gene in spite of increasing drug dose. On the other hand, while there was no difference in cells in static 3D conditions, reductions in gene expression occurred as the drug dose started to increase in dynamic conditions. For *EpCAM* expression while the static2D condition followed a stable trend, the static3D condition showed an increase in the levels of *EpCAM* gene

expression when 10^5 nM drug was administered (Figure 4.18b). Unlike static conditions, in cells cultured in dynamic conditions, gene expression increased from the beginning of 0.1 nM of drug administration. Finally, when assessing *MDR-1* and *BCRP* genes, guiding us for chemoresistance, the expression of both genes increased with the drug for dynamic conditions (Figure 4.18c-d). On the other hand, the expressions of these genes were stable at static conditions.

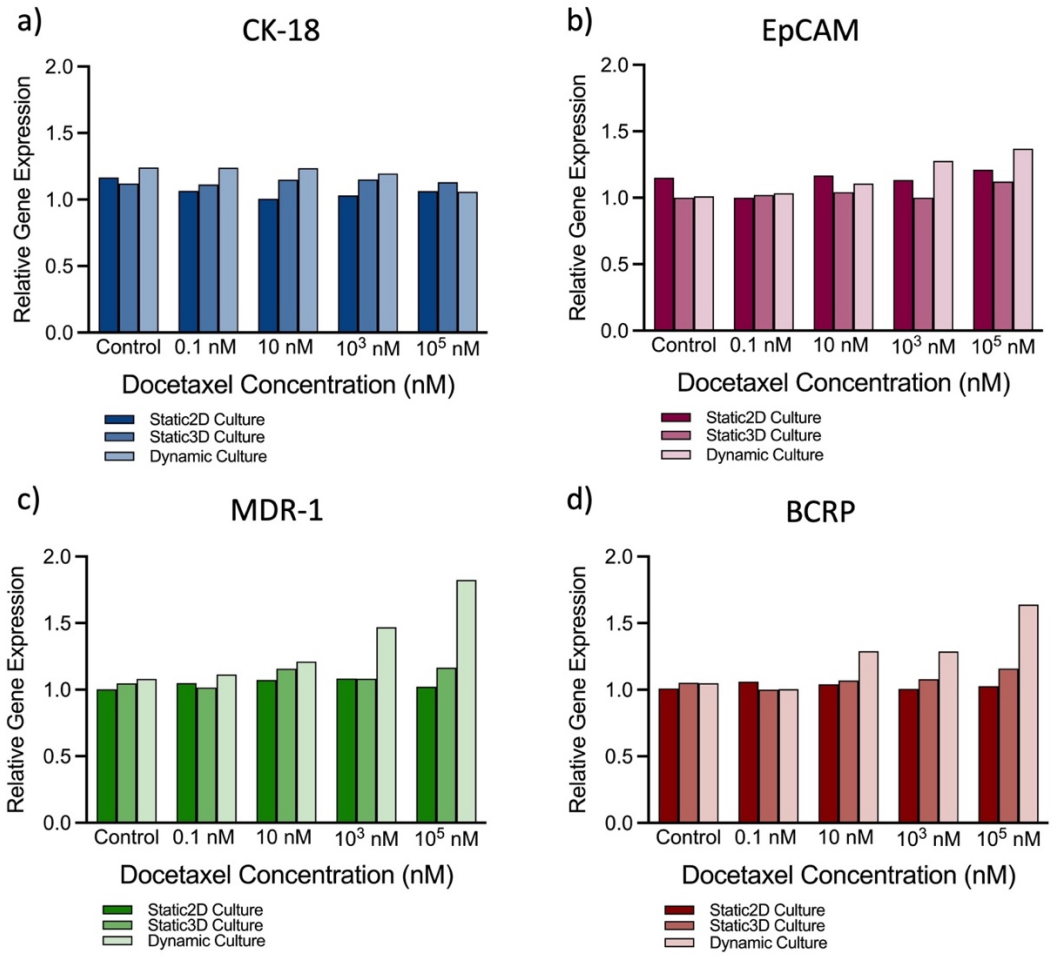


Figure 4.18 Gene expression analysis for *CK-18, EpCAM, MDR-1,* and *BCRP* is demonstrated on the course of docetaxel treatment.

CHAPTER 5

5.EXTRACELLULAR VESICLES (EVs) STUDIES

In this section, medium in the presence and absence of anti-cancer drugs were collected from cell cultures under three different conditions. Accordingly, EV isolation was performed from these medium. As noted, isolation and analysis would be challenging due to a number of factors. One of major difficulties in the isolation is low abundance of EVs in biological fluids [140]. Another challenge in EVs isolation is the presence of other vesicles or debris, and these artifacts may interfere with the isolation process [142]. Many biological fluids, such as blood, urine, and cerebrospinal fluid, contain other types of vesicles, that may be present in similar sizes and densities to EVs [142]. These vesicles can be difficult to distinguish from EVs and may interfere with their isolation. Other challenge is the potential for sample contamination during the isolation process [143]. Contamination possibly occurs from a variety of sources, including reagents, equipment, and handling, and can lead to misleading results. It is important to follow strict protocols and use high-quality reagents and equipment to minimize the risk of contamination [143]. Overall, the difficulties of EV isolation can make it challenging to obtain sufficient amounts of pure sample for analysis. Careful sample preparation and the use of appropriate isolation methods are critical to ensure the quality and purity of EVs. To overcome all these difficulties, we herein employed two filter-integrated microfluidic chips in our study [111]. Nanoparticle tracking analysis (NTA) of the isolated EVs was then performed to obtain information about EV size and concentration. Afterwards, EVs were imaged with Scanning Electron Microscopy (SEM) to evaluate any morphological changes. Finally, CD63 and CD81 (two of tetraspanins) proteins on the membranes of EVs were confirmed by western blot analysis.

5.1 Nanoparticle Tracking Analysis (NTA) Results

This section was conducted with Chapter 3 and Chapter 4 simultaneously. In Chapter 3, the media of cells cultured in static2D, static3D, and dynamic environments for 7 days were collected. In Chapter 4, the media were collected at the end of the culturing period of the cells treated with different doses of doxorubicin and docetaxel. These media were then centrifuged at 20000 x g to remove dead cells and large debris. The resulting supernatant was filtered with a 0.22 μm of syringe filter, and introduced into the EVs isolation microfluidic chip. NTA analyzes were utilized by diluting the samples at a certain ratio (1:100).

5.1.1 NTA analysis of Static2D, Static3D and Dynamic conditions without anti-cancer drug

While analyzing EV numbers, we considered crude EV collection from each condition, and we did not perform any normalization per the cell numbers. Therefore, EV number were plotted according to concentration results obtained from the NTA analysis. Briefly, 115,000 cells/flask were seeded for static2D, static3D and dynamic conditions at the beginning of the experiments. However, at the end of 7 days, cell numbers obtained from each condition were different. EV numbers would be proportional to cell numbers obtained at the end of the experiment. However, we did not perform any cell number normalization according to cell numbers at the end of the experiment since we initially seeded each condition with same cell numbers. As a note, while cells die, there would be more vesicles in both 2D and 3D static conditions due to apoptosis process, and this would be missed in dynamic conditions although collecting all the media in the syringes. In dynamic condition, there is a continuous flow to refresh the environment simultaneously, and the release of dead cells or debris during the flow was not at the same environment as those of 2D and 3D conditions.

Briefly, based on the average of four measurements, static2D conditions produced $2.15 \times 10^{10} \pm 6.1 \times 10^{9}$ particles/mL along with mean and mode values of 145.5 ± 16.4

nm and 105.5 ± 10.0 nm, respectively (Figure 5.1 a-d). On the other hand, when the static3D conditions results were examined, 4.8 x 10^{10} ± 6.1 x 10^{9} particles/mL was produced, and their mean values were 151.7 ± 21.2 nm. Moreover, their mode values were 127.5 ± 17.4 nm (Figure 5.1 e-h). Lastly, the average of dynamic conditions enabled to produce 2.7 x 10^{10} ± 2.72 x 10^{9} particles/mL along with mean and mode values of 132.3 ± 1.8 nm and 100.8 ± 10.5 nm, respectively (Figure 5.1 i-l). Looking at the mean values, static 3D conditions resulted in the highest mean value. After static3D, static2D had the highest mean while the lowest mean value was obtained for dynamic conditions.

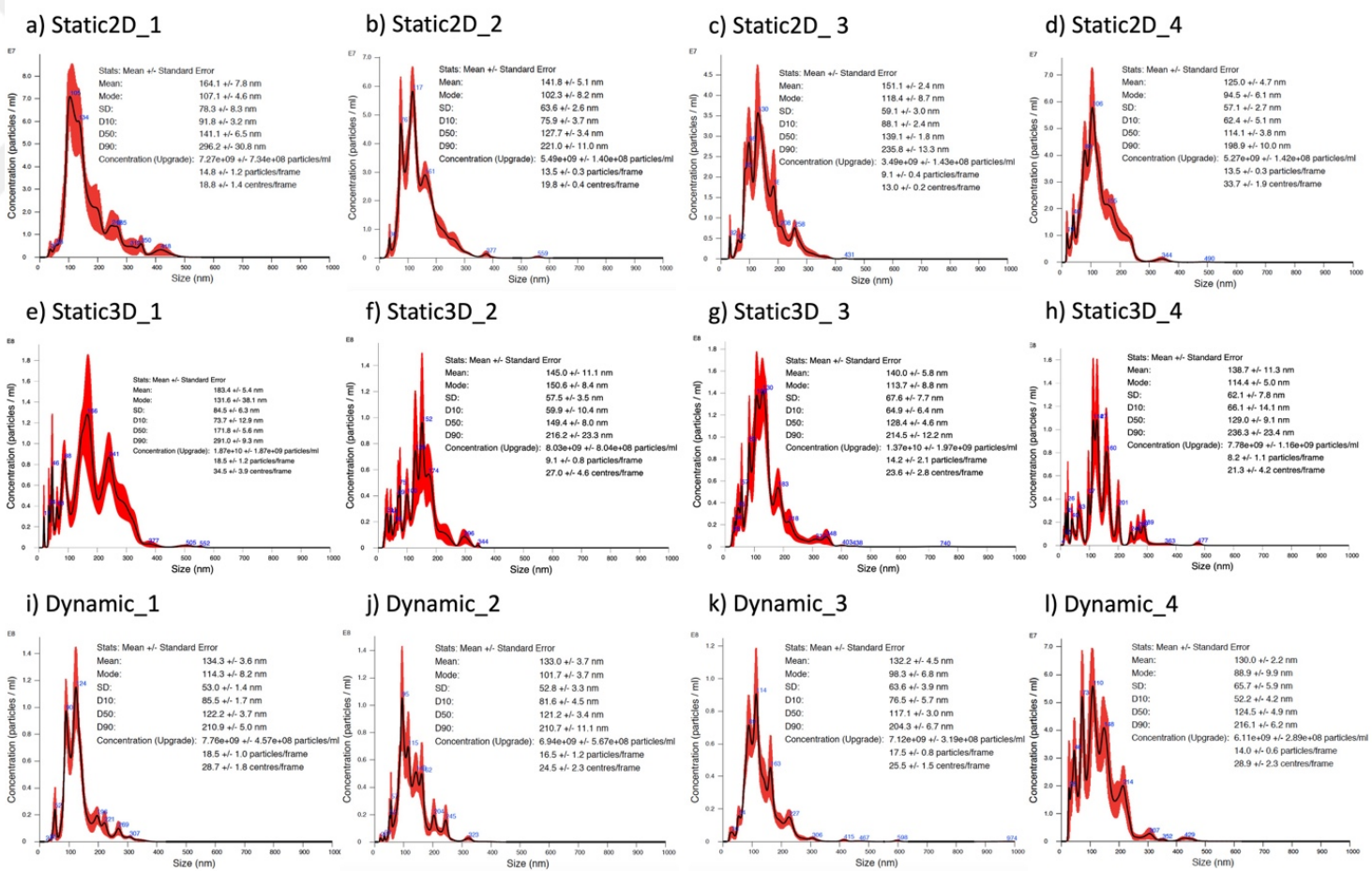


Figure 5.1. NTA analysis of EVs isolated from static2D, static3D and dynamic conditions. Evaluating the results of EVs isolated from a-d) static2D, e-f) static3D conditions, and i-l) dynamic conditions (n=4).

To understand any statistical differences between three culturing conditions, the size and concentration of EVs were analyzed. Here, a violin graph was plotted by considering the mean and mode values of three measurements obtained from EVs isolated from static2D, static3D and dynamic conditions. An ordinary one-way ANOVA test was employed for statistical analysis, and as a result of multiple comparisons, there was no significant difference observed between the mean size value of EVs for each condition ($n=3$, $p>0.05$) (Figure 5.2a). Although there was no statistical difference, the variance of EVs mean values obtained from dynamic conditions was lower than that of static conditions (Figure 5.2a). The sizes of EVs obtained from dynamic conditions were similar to each other. The size range in static conditions was quite wide. Again, an ordinary one-way ANOVA test was employed for statistical analysis, and as a result of multiple comparisons, there was the significant difference was observed between the mode size value of EVs for static3D and dynamic conditions ($n=4$, $p<0.05$). Lastly, a column graph was plotted by calculating the number of EVs per mL volume (concentration) from the data of three different conditions (Figure 5.2b). An ordinary one-way ANOVA test was applied, and there was a significant difference observed between the number of particles per volume of EVs obtained from the static2D and static3D conditions (Figure 5.2c) ($n=4$, $p<0.05$).

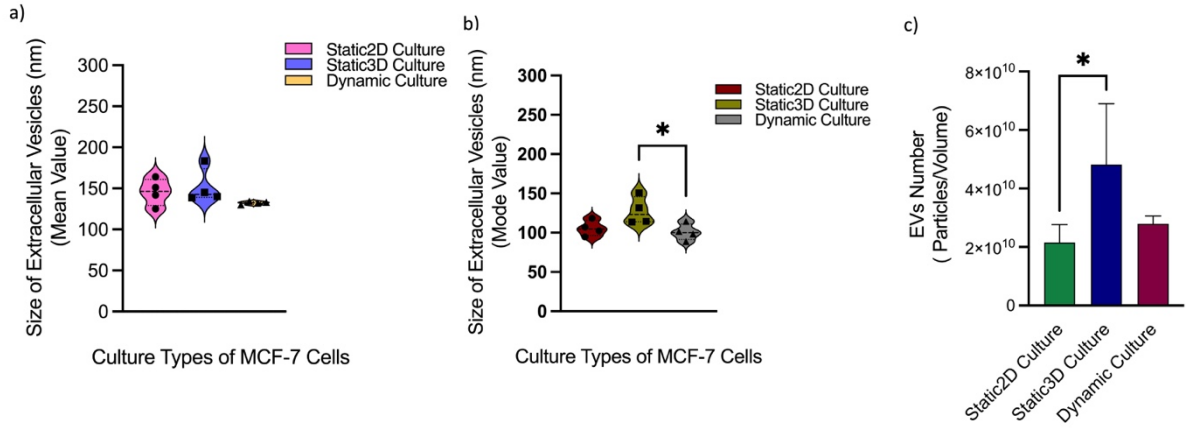


Figure 5.2. Investigating the effects of different culture conditions (static2D, static3D, and dynamic) on size and concentration of EVs. For statistical assessments, we performed an ordinary one-way ANOVA test ($n=3$, $p<0.05$). Asterisk demonstrates statistical difference between the groups.

5.1.2 Doxorubicin NTA Results

Fort he regard of drug experiments, the EV isolation assay was performed in the cells cultured in static2D, static3D, and dynamic conditions that were treated with doxorubicin. In this experiment, control group was determined as the cells that were not treated with the drug. Other groups were trated with doxorubicin at doses of 0.1 nM , 10 nM, 10^3 nM, and 10^5 nM, and EVs were isolated by collecting the media at the end of the experiment period. NTA analyzes of isolated EVs were made (Figure 5.3) and violin graphs were plotted using the mean, mode and concentration values derived from these data.

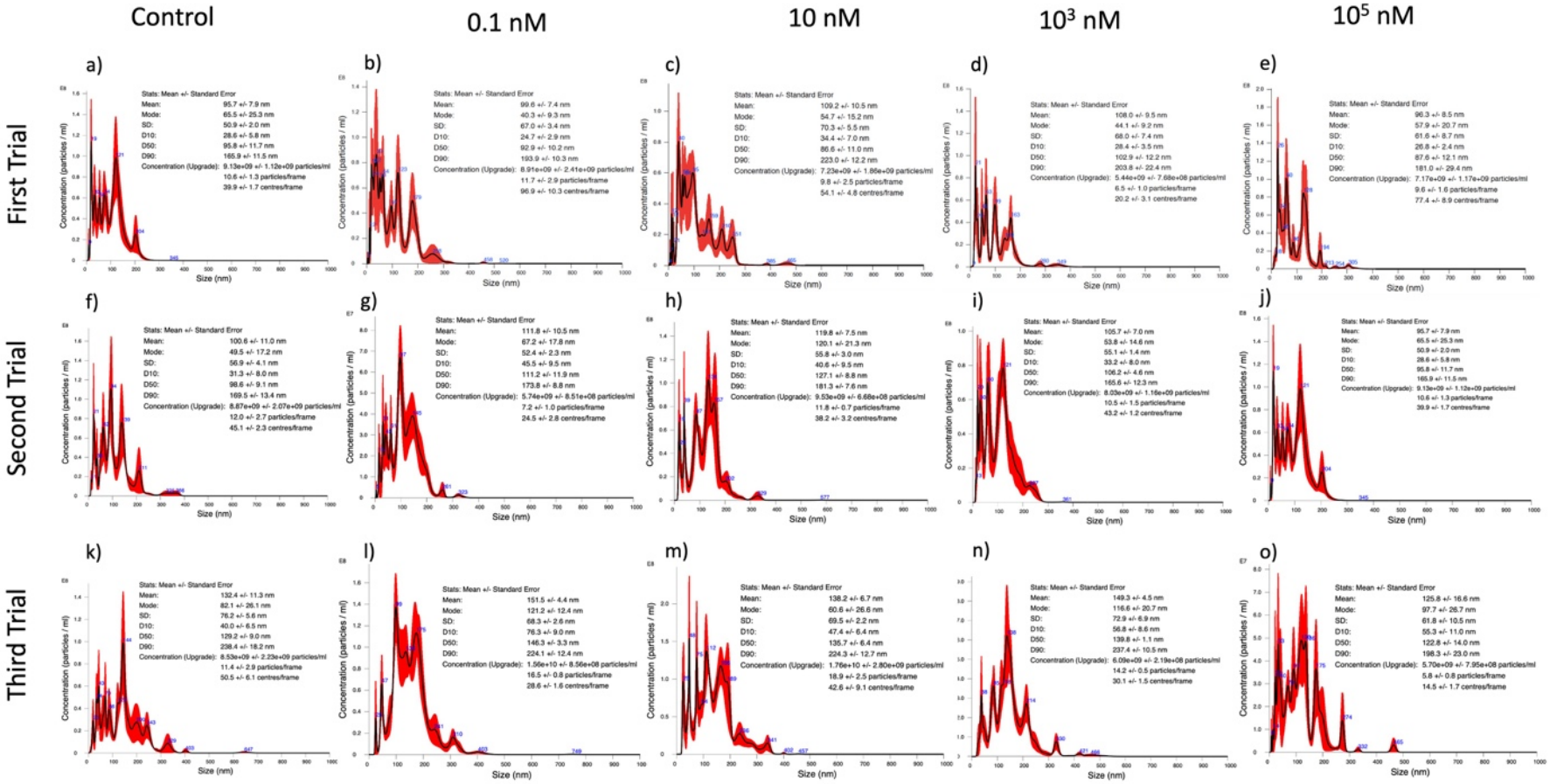


Figure 5.3 NTA analysis for control non-treated and doxorubicin (0.1 nM, 10 nM, 10^3 nM and 10^5 nM doses) administered cells under static2D condition (n=3)

In order to assess statistical meaning, an ordinary one-way ANOVA test was applied to the experimental groups, and no significant difference was observed in the mean scores of the EVs as a result of multiple comparison (n=3, p>0.05). (Figure 5.4a). Furthermore, there was no statistically difference for the mode values of EVs per an ordinary one-way ANOVA test (n=3, p>0.05) (Figure 5.4b). Finally, the EVs number was calculated in this section, and an increase was observed in the number of EVs until 10 nM drug administration, while a decrease was observed after 10^3 nM and 10^5 nM doses were provided. This might be because the cells were more affected by high dose, forming apoptotic bodies in EVs species. Since the sizes of apoptotic bodies were between 500-2000 nm [80], our system was not able to isolate them due to their large sizes.

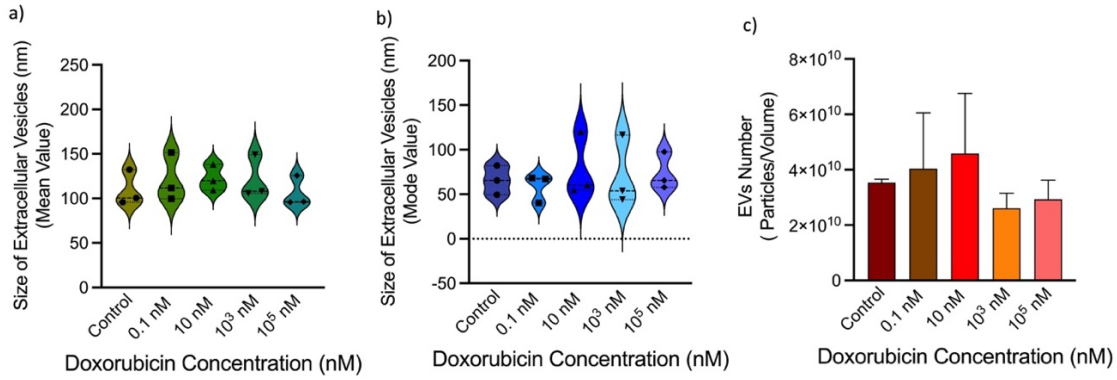


Figure 5.4. Investigating the effects of doxorubicin on size and concentration of EVs collected from Static2D conditions. a) Mean values, b) mode values, and c) EV concentrations are presented. For statistical assessments, we performed an ordinary one-way ANOVA test, and there was no statistical differences observed between the groups (n=3, p>0.05).

NTA analyses were performed for the EVs collected from static3D condition. As a representative example in this experiment, we investigated the results of the first trial. According to the NTA results of static3D conditions, control group produced 1.64 x 10^{10} ± 2.9 x 10^9 particles/mL (Figure 5.5a) along with mean and mode values of 182.3 ± 19.6 nm and 131.6 ± 30.7 nm, respectively. In contrast, the particles collected from 0.1 nM of doxorubicin treated group produced 1.08 x 10^{10} ± 9.52 x 10^8 particles/mL and mean and

mode sizes of 137.3 ± 7.9 nm and 114.6 ± 12.8 nm, respectively (Figure 5.5b). When the results of the 10 nM of doxorubicin originated EVs were examined, 2.40 x 10^{10} ± 2.85 x 10^{9} particles/mL (Figure 5.5c) was produced along with mean and mode values of 160.7 ± 9.3 nm and 115.8 ± 5.1 nm, respectively. On the other hand, 10^{3} nM drug produced 1.46 x 10^{10} ± 2.12 x 10^{9} particles/mL (Figure 5.5d) along with the mean value of of 153.1 ± 7.2 nm and the mode value of 135.8 ± 12.1 nm. Finally, when the concentration of EVs collected from the highest dose of 10^{5} nM was considered, its concentration was 1.78 x 10^{10} ± 8.66 x 10^{8} particles/mL (Figure 5.5e) along with mean and mode values of 144.4 ± 4.9 nm and 131.6 ± 11.2 nm, respectively. When the concentration values were examined, there was no noteworthy difference between the groups.

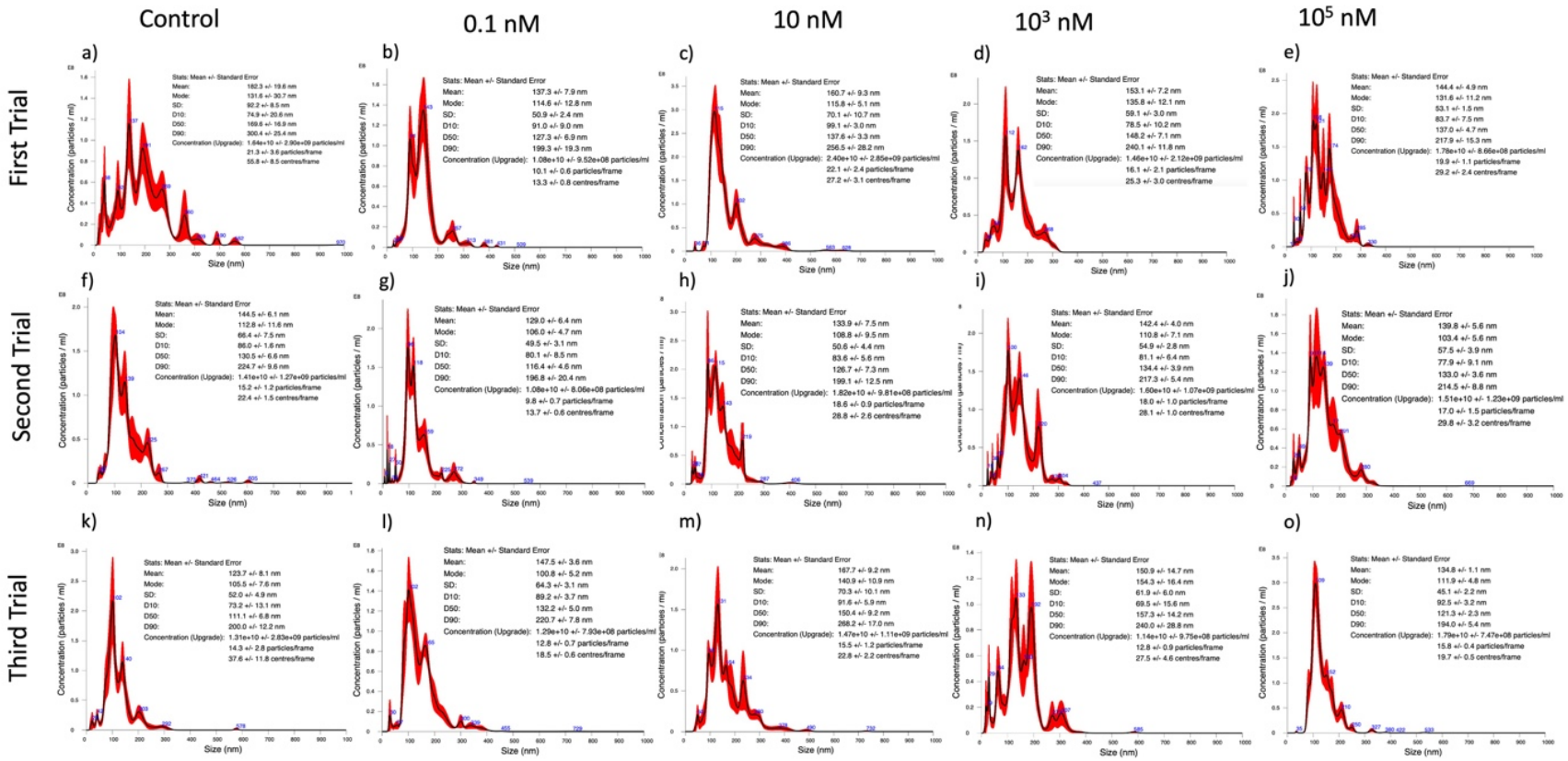


Figure 5.5. Size and concentration of EVs collected from doxorubicin treated Static3D conditions (n=3)

An ordinary one-way ANOVA test was employed to investigate any statistical differences between control group and the groups treated with four different doses of drugs, and no significant difference was observed as a result of multiple comparisons (n=3, p>0.05) (Figure 5.6a). The variance of the mean for the static3D condition, on the other hand, was lower while applying 10^3 nM and 10^5 nM of drug doses. A modest variance signified that the data points were often near to both the mean and to one another. The same statistical analysis method was applied for the mode values, and there was no significant difference (n=3, p>0.05) according to an ordinary one-way ANOVA test (Figure 5.6b). Finally, as depicted in Figure 5.6c, an ordinary one-way ANOVA was applied for EV numbers, and a significance difference was observed between the values obtained at 0.1 nM and 10 nM (n=3, p<0.05). The reason for this might be that 0.1 nM of the drug was not enough for the cells to turn into apoptosis. In such a situation, the production of EVs in cancer cells might be increased when 100 times more drug doses were applied [144].

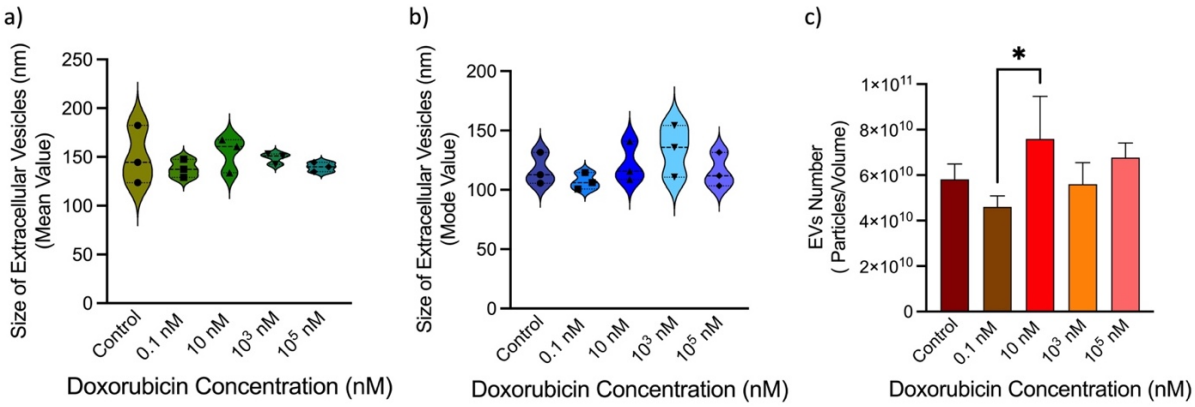


Figure 5.6. Investigating the effects of doxorubicin on size and concentration of EVs collected from static3D conditions. a) Mean values, b) mode values, and c) EV concentrations are presented. For statistical assessments, we performed an ordinary one-way ANOVA test (n=3, p<0.05). Asterisk demonstrates statistical difference between the groups.

Finally, for doxorubicin, the same strategy was performed for EVs obtained from dynamic conditions. The NTA analysis of isolated particles were performed as depicted in Figure 5.7. When the mean and mode values were analyzed statistically, there was no significant difference observed per the ordinary one-way ANOVA and multiple comparison results ($n=3$, $p>0.05$) (Figure 5.8 a-b). Still, under dynamic conditions, the variance in mean and mode values of the control cell group was smaller than that of the drug-administered groups. EV numbers were stated in Figure 5.8c. According to these results, the number of EVs in the control group was the least for dynamic conditions. As the drug was administered, the cells begun to produce more EVs, which would potentially explain the large variance in the mean and mode values.

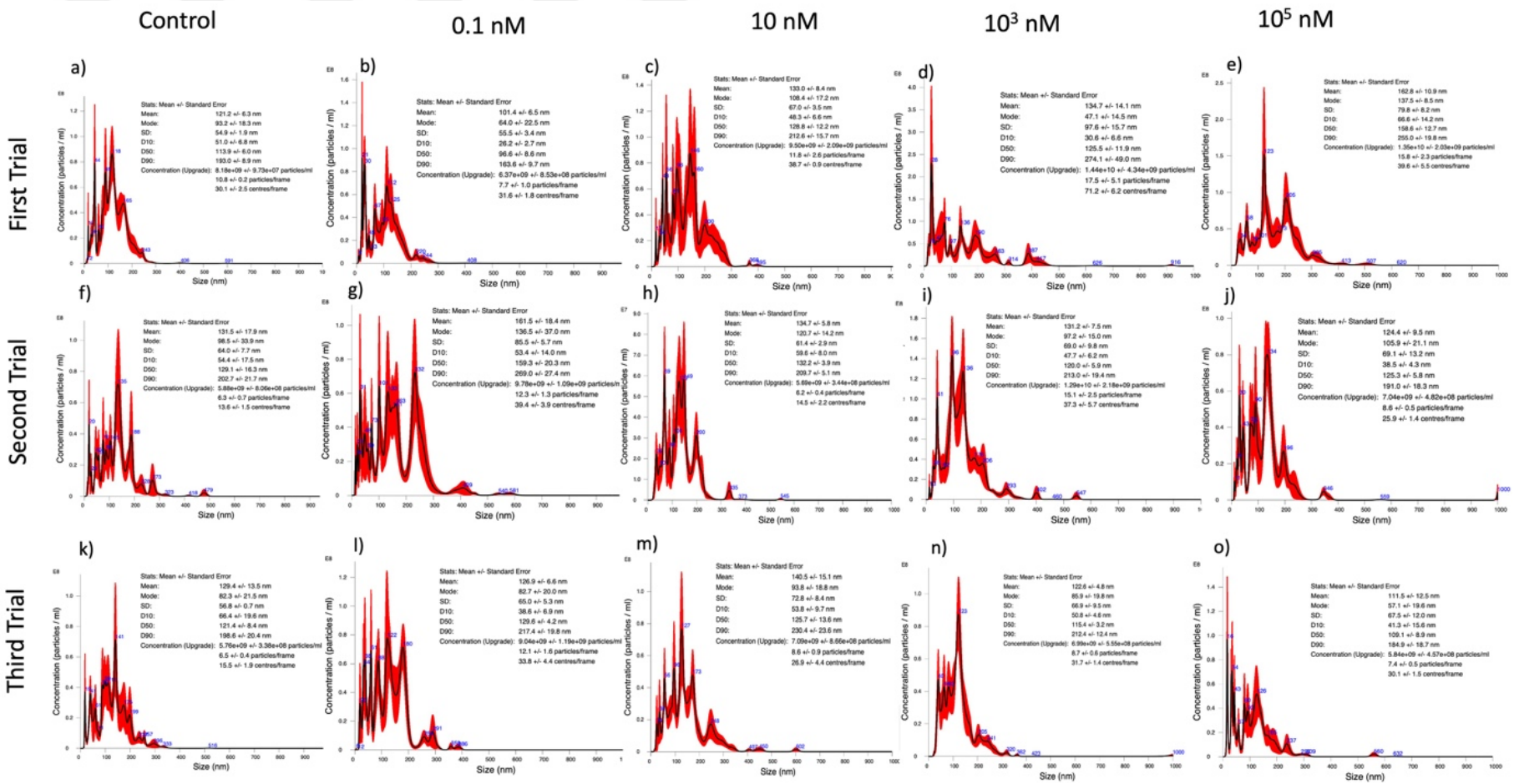


Figure 5.7. NTA analysis for control (non-treated) and doxorubicin (0.1 nM, 10 nM, 10^3 nM and 10^5 nM doses) administered cells under dynamic condition (n=3).

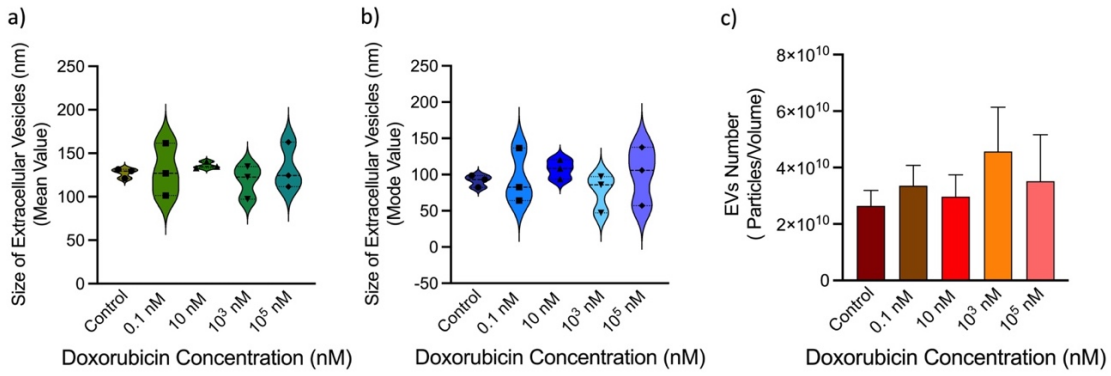


Figure 5.8. Investigating the effects of doxorubicin on size and concentration of EVs collected from dynamic conditions. a) Mean values, b) mode values, and c) EV concentrations are presented. For statistical assessments, we performed an ordinary one-way ANOVA test, and there was no statistical differences observed between the groups ($n=3$, $p>0.05$).

In addition, no significant differences were observed when the EV size and concentration values of the static2D, static3D, and dynamic conditions were evaluated among themselves ($n=3$, $p>0.05$) according to two-way ANOVA test (Figure 5.9). When we assessed the mean values for control group, a significant difference was observed between static2D and static3D according to two-way ANOVA test (Figure 5.9a) ($n=3$, $p<0.05$). EVs mode values were stated in the Figure 5.9b. When comparing the three groups, according to the results of two-way ANOVA test, there was a significant difference between static2D and static3D in the control group and 10^3 nM of doxorubicin ($n=3$, $p<0.05$). In addition, for EV numbers, there was a difference between static3D and dynamic in the control group ($n=3$, $p<0.005$). Also, there was a statistically difference between static2D and static3D in 10 nM ($n=3$, $p<0.05$), 10^3 nM ($n=3$, $p<0.05$), and 10^5 nM ($n=3$, $p<0.005$) of doxorubucin (Figure 5.9c). In addition, a significant difference was observed between static3D and dynamic at both 10 nM ($n=3$, $p<0.0005$) and 10^5 nM ($n=3$, $p<0.005$) of doses.

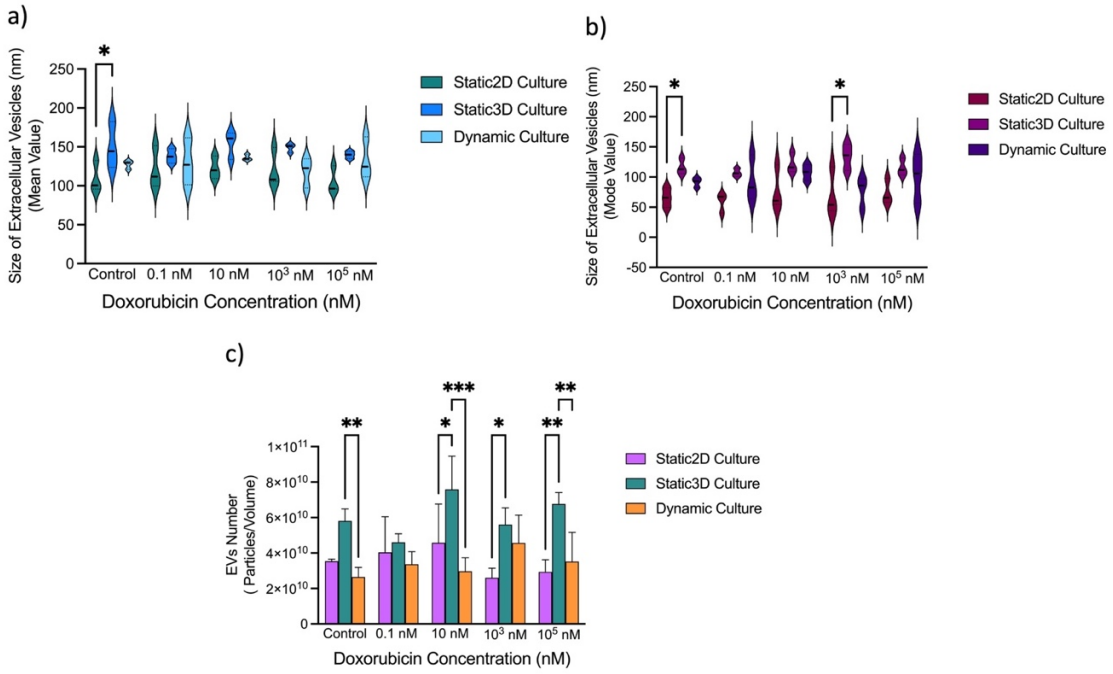


Figure 5.9. Comparing a) mean values, b) mode values, and c) EV concentrations of static2D, static3D and dynamic conditions on the course of doxorubucin. For statistical assessments, we performed two-way ANOVA test (n=3). Statistical differences were examined comprehensively in the analysis. * represents $p<0.05$, ** shows $p<0.005$, and *** states $p<0.0005$.

5.1.3 Docetaxel NTA Results

Likewise, we herein performed NTA for EVs collected from static2D, static3D, and dynamic conditions treated with docetaxel, as another anti-cancer drug. In this section, we initially evaluated the EV results from non-treated control group and four different doses of docetaxel were examined for static2D conditions, and three measurements were made for each group. An average of three measurements of the control group produced $3.15 \times 10^{10} \pm 8.25 \times 10^{9}$ particles/mL (Figure 5.10 a-f-k). The mean values of these particles are 114.4 ± 20.10 nm, while the mode values were 95.3 ± 12.5 nm (Figure 5.10 a-f-k). When 0.1 nM of docetaxel drug was administered, the number of particles obtained from the three measurements was $4.71 \times 10^{10} \pm 1.13 \times 10^{10}$ particles/mL along with mean and mode values of 131.6 ± 20.9 nm and 80.7 ± 39.7 nm,

respectively. (Figure 5.10 b-g-l). The number of EVs in the case of 10 nM of drug dose was $3.58 \times 10^{10} \pm 2.40 \times 10^{10}$ particles/mL. The mean values of these particles were 146.3 ± 45.8 nm, while the mode values were 96.53 ± 59.61 nm (Figure 5.10 c-h-m). The EVs produced in the case of 10^3 nM and 10^5 nM of drug doses were $3.89 \times 10^{10} \pm 1.83 \times 10^{10}$ particles/mL (Figure 5.10 d-i-n) and $2.81 \times 10^{10} \pm 4.37 \times 10^{10}$ particles/mL (Figure 5.10 e-j-o), respectively. The mean values were 154.9 ± 9.9 nm and 131.4 ± 26.22 nm, and the mode values were 113.4 ± 23.0 nm and 90.2 ± 23.5 nm for 10^3 nM and 10^5 nM of docetaxel, respectively.

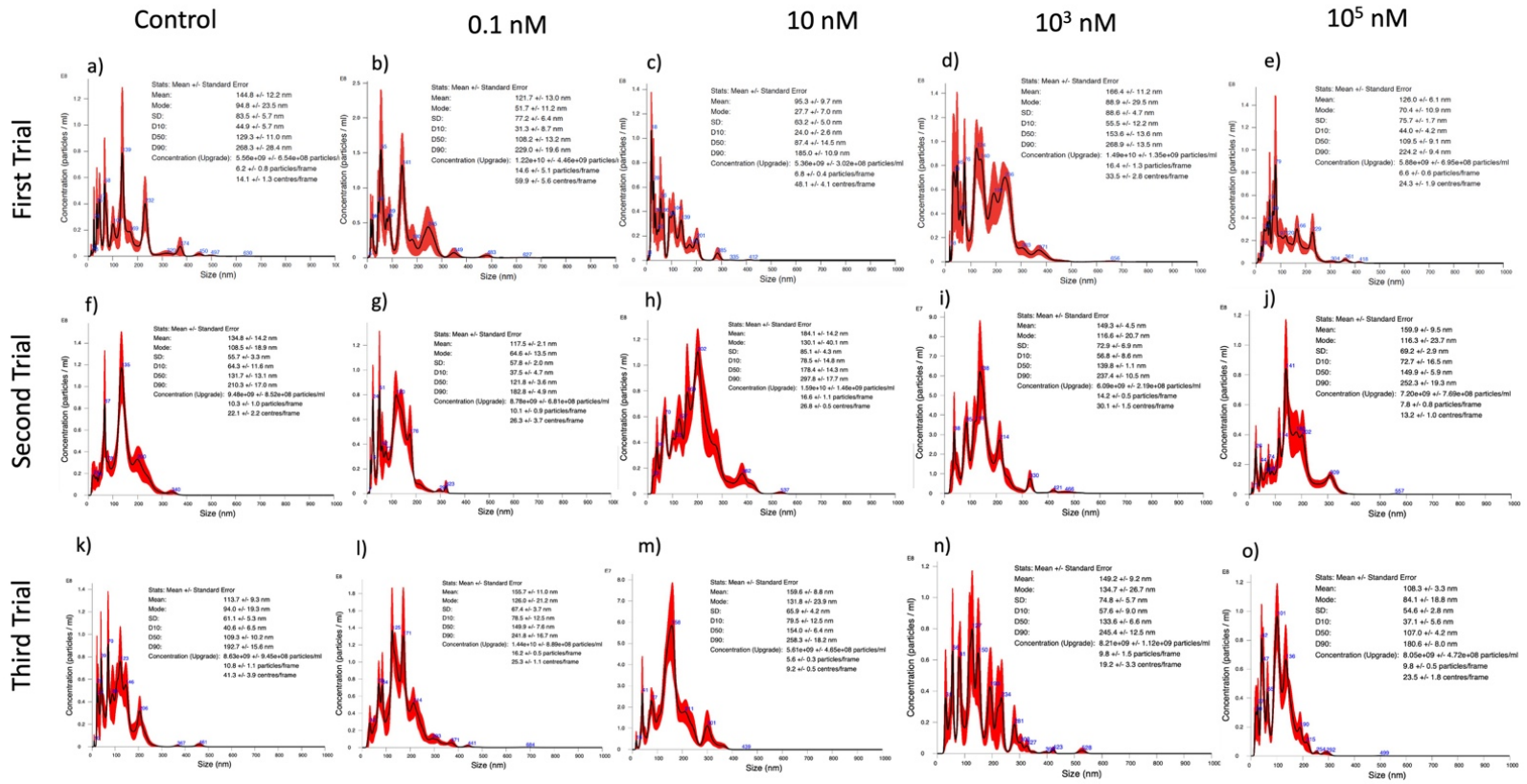


Figure 5.10. NTA analysis for control (non-treated) and docetexal (0.1 nM, 10 nM, 10^3 nM and 10^5 nM doses) administered cells under static2D condition (n=3).

The mean, mode and number values of EVs from docetaxel-treated static2D condition were plotted with the results from NTA analysis (Figure 5.11). According to an ordinary one-way ANOVA test, there was no statistical significance observed for mean and mode values (n=3, p>0.05). Evaluating the mode value graph, the variance of the values in the control group was smaller, that is, most of the EVs have the same size. Mode variances increased after administration of docetaxel (Figure 5.11b). The drug had potentially caused some changes in the size of the EVs. In addition, no statistical difference was observed in the number of EVs according to an ordinary one-way ANOVA test (n=3, p>0.05) (Figure 5.11c).

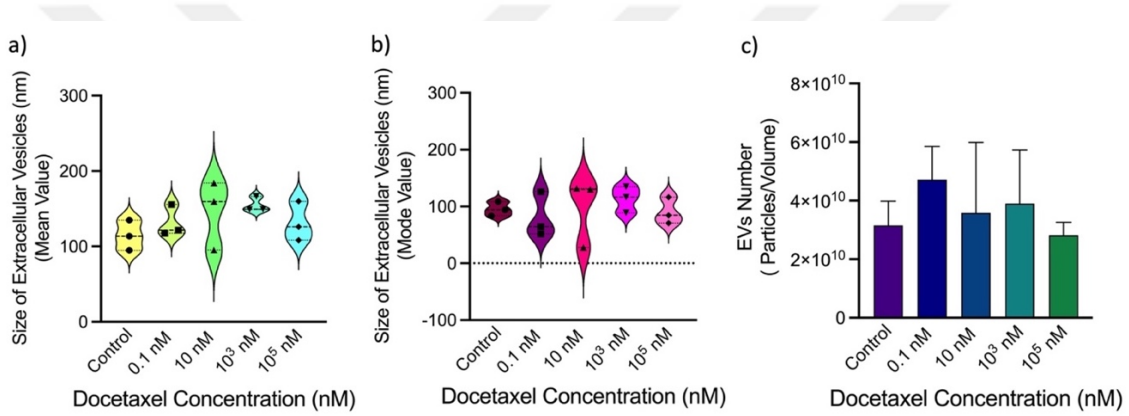


Figure 5.11. Investigating the effects of docetaxel on size and concentration of EVs collected from static2D conditions. a) Mean values, b) mode values, and c) EV concentrations are presented. For statistical assessments, we performed an ordinary one-way ANOVA test, and there was no statistical differences observed between the groups (n=3, p>0.05).

EVs obtained from non-treated control group and 0.1 nM, 10 nM, 10^3 nM, 10^5 nM of docetaxel treated groups were isolated and analyzed accordingly. Figure 5.12 shows the EV analysis of static3D condition treated with docetaxel. The mean, mode, and concentration values were indicated in Figure 5.13.

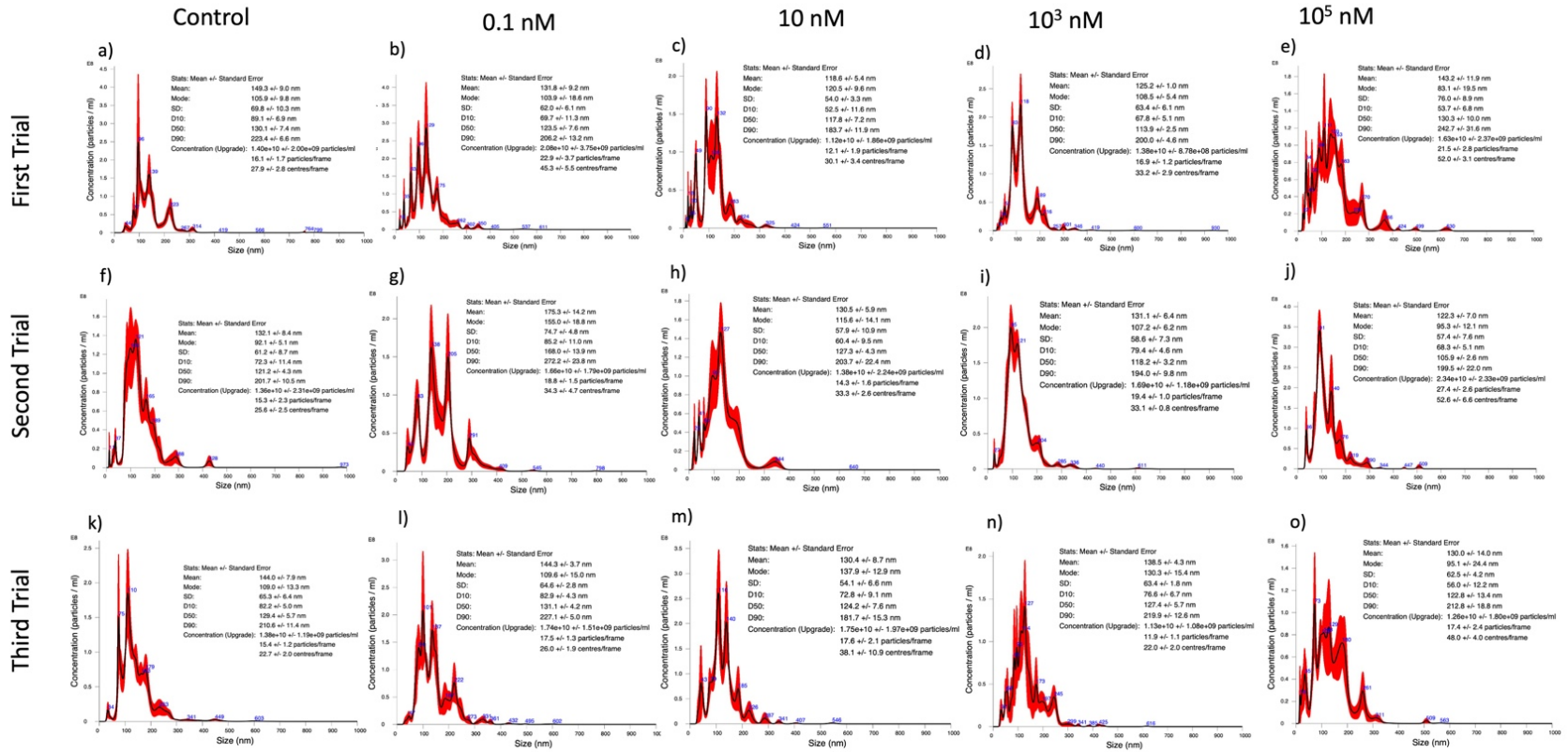


Figure 5.12. NTA analysis for control (non-treated) and docetexal (0.1 nM, 10 nM, 10^3 nM and 10^5 nM doses) administered cells under static3D condition (n=3)

The mean, mode, and EV numbers of static3D condition were shown in Figure 5.12. An ordinary one-way ANOVA test and multiple comparisons were applied to the results in the violin plot including mean values; yet, no statistically significant difference was observed (n=3, p>0.05). Moreover, mean variance was very narrow in the groups except for 0.1 nM of docetaxel. The values obtained from the measurements were quite close to each other (Figure 5.13a). Assessing the mode plot in Figure 5.13b, there was no significant difference found as a result of the ordinary one-way ANOVA (n=3, p>0.05). On the other hand, this graph was quite similar to the mean plot. The variance was smaller in groups other than 0.1 nM of drug dose. Finally, no significant difference was found in the EV numbers per an ordinary one-way ANOVA test and multiple comparisons (n=3, p>0.05) (Figure 5.13c). In addition, the number of EVs obtained from the control group was lower than that of the docetaxel-treated groups.

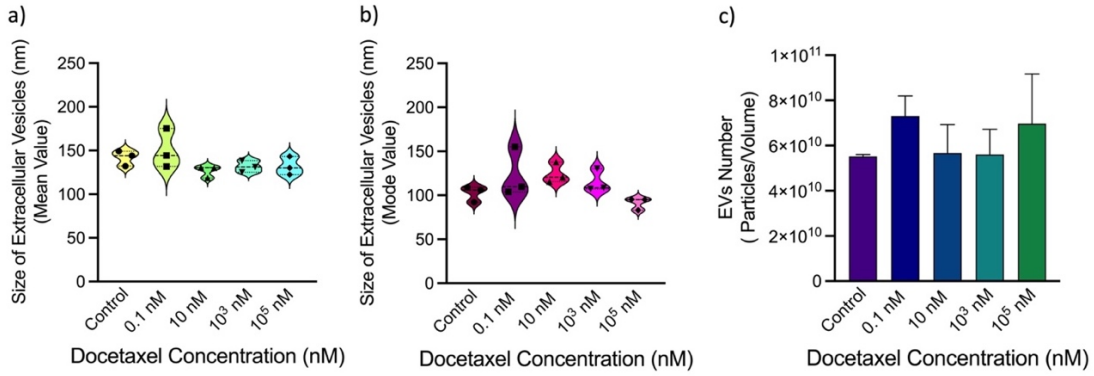


Figure 5.13. Investigating the effects of docetaxel on size and concentration of EVs collected from static3D conditions. a) Mean values, b) mode values, and c) EV concentrations are presented. For statistical assessments, we performed an ordinary one-way ANOVA test, and there was no statistical differences observed between the groups (n=3, p>0.05).

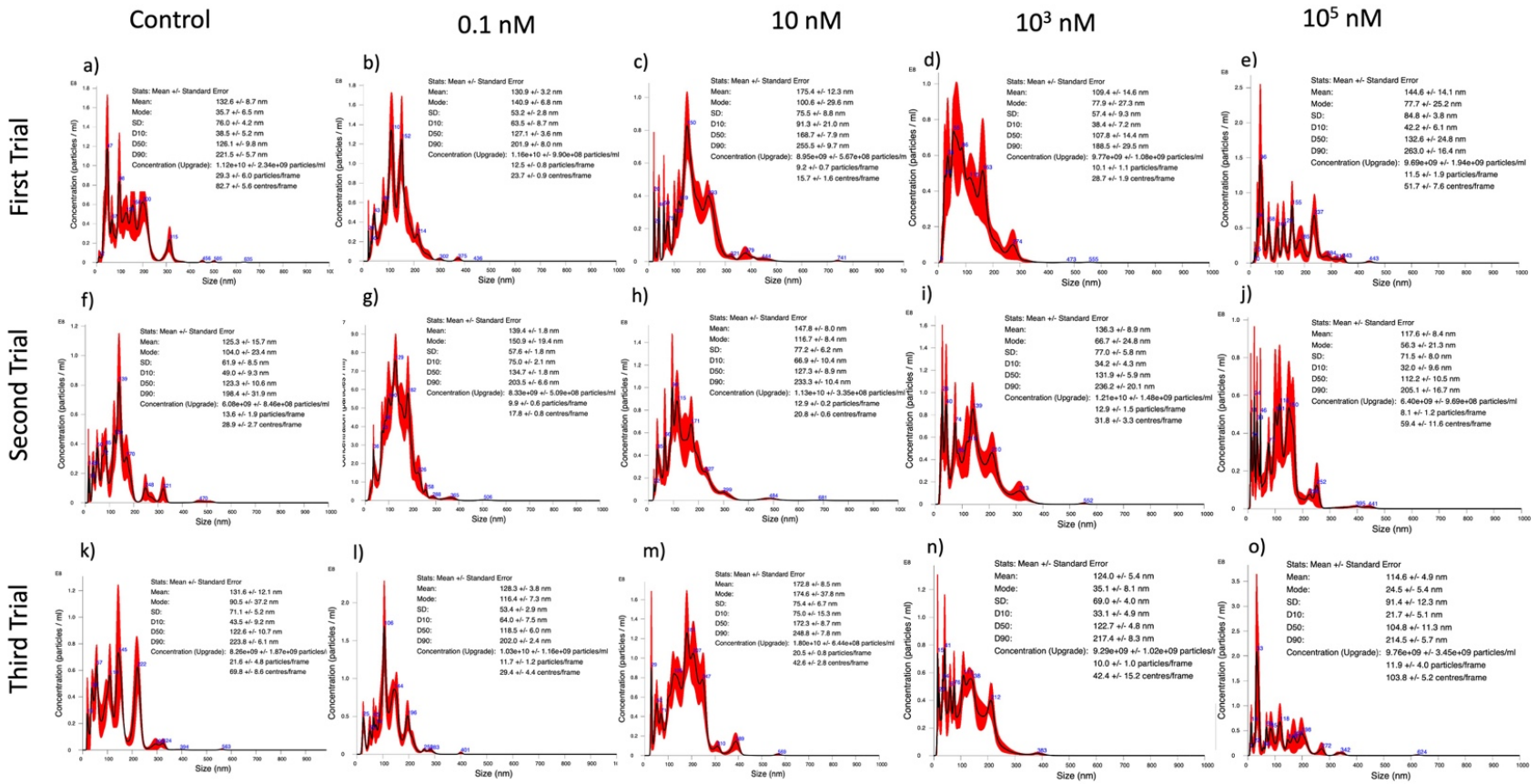


Figure 5.14. NTA analysis for control (non-treated) and docetexal (0.1 nM, 10 nM, 10^3 nM and 10^5 nM doses) administered cells under dynamic condition (n=3)

Finally, EVs isolated from dynamic conditions in docetaxel-treated experiments were analyzed (Figure 5.14). The values calculated in the NTA were shown with violin plots for further interpretations (Figure 5.15). Considering the mean plot, a significant difference was observed between the control group and 10 nM, between 10 nM and 10^3 nM, and between 10 nM and 10^5 nM of drug dose as a result of the ordinary one-way ANOVA test (n=3, $p<0.05$) (Figure 5.15a). In addition, the mean variance of the control group and the group treated with 0.1 nM of docetaxel was quite small compared to those treated with other high-dose drugs. In the mode graph shown in Figure 5.15b, a statistically significant difference was observed between the 0.1 nM and 10^5 nM of docetaxel-treated groups as a result of one-way ANOVA (n=3, $p<0.05$). Although there was no statistical difference in EVs numbers, control group had lower EV numbers compared to the drug treated groups (n=3, $p>0.05$) (Figure 5.15c).

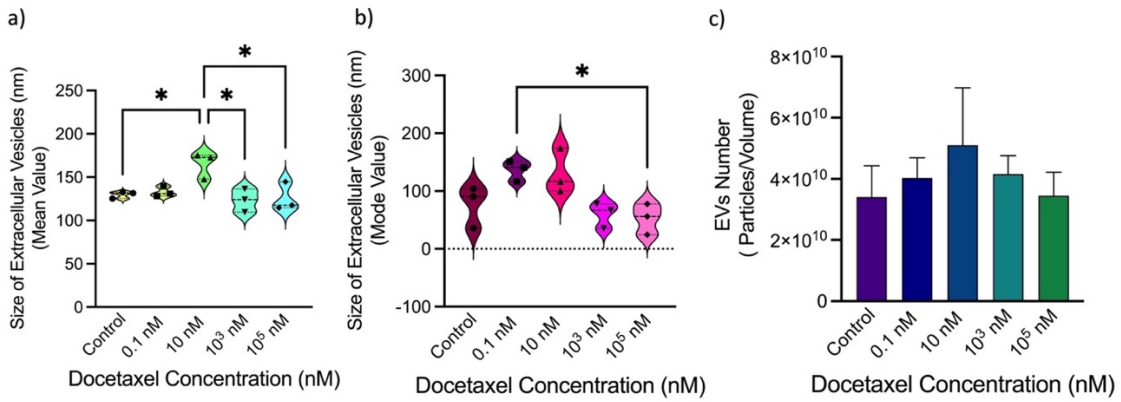


Figure 5.15. Investigating the effects of docetaxel size and concentration of EVs collected from dynamic conditions. a) Mean values, b) mode values, and c) EV concentrations are presented. For statistical assessments, we performed an ordinary one-way ANOVA test (n=3, $p<0.05$). Asterisk demonstrates statistical difference between the groups.

After static2D, static3D and dynamic conditions were evaluated within themselves, all conditions were evaluated together in Figure 5.15. According to two-way ANOVA test, a significant difference was observed between static3D and dynamic conditions at 10 nM of docetaxel (n=3, $p<0.05$) (Figure 5.16a). Evaluating the mode

graph obtained from three conditions, no significant difference was found between any groups (n=3, p>0.05) (Figure 5.16b). Finally, when considering at the EV numbers, a significant difference was found between static3D and dynamic conditions at a dose of 0.1 nM according to two-way ANOVA test (n=3, p<0.05) (Figure 5.16c). In addition, as a result of the same test, a statistically significant difference was found between static2D and static3D, and between static3D and dynamic conditions in 10^5 nM of docetaxel doses (n=3, p<0.005). In general, when Figure 5.16c is examined, the number of EVs obtained from the static 3D environment has the highest value for each experimental group. On the other hand, the number of EVs obtained from dynamic conditions was higher than those obtained from static2D in all groups except the 0.1 nM dose docetaxel-treated group.

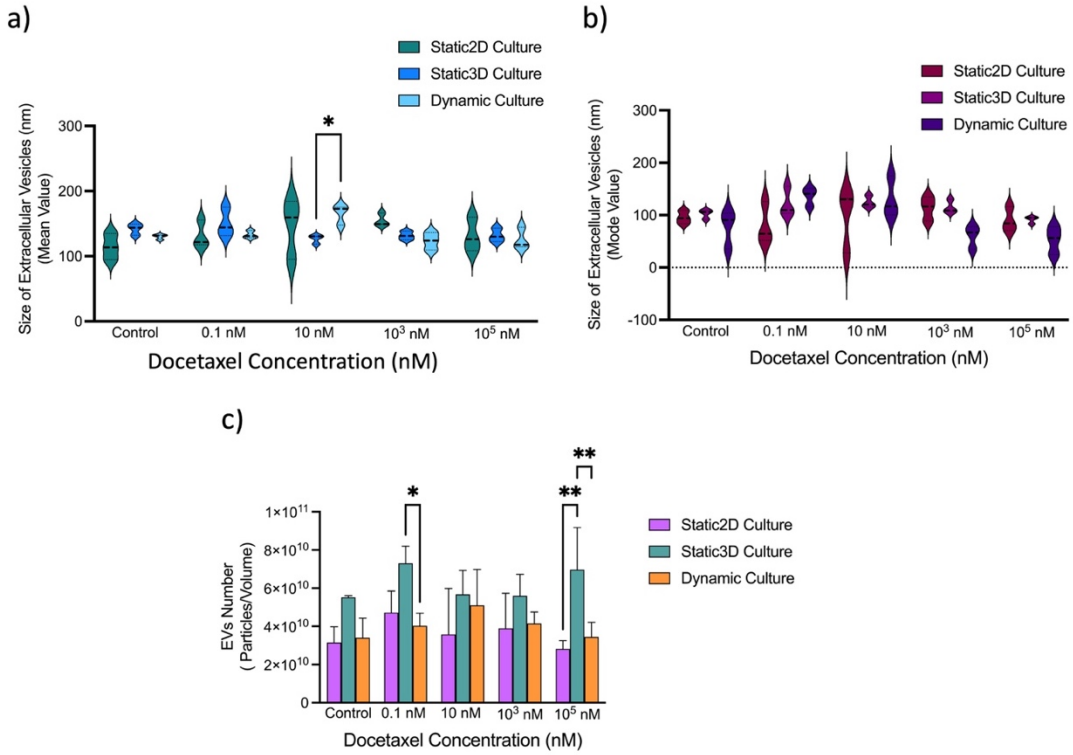


Figure 5.16. Comparing a) mean values, b) mode values, and c) EV concentrations of static2D, static3D and dynamic conditions on the course of docetaxel. For statistical assessments, we performed two-way ANOVA test (n=3). Statsitical differences were examined comprehensively in the analysis. * represents p<0.05 and ** states p<0.005.

5.2 Scanning Electron Microscopy (SEM) Results

In this section, the images of EVs obtained from static2D, static3D, and dynamic conditions in the absence and presence of anti-cancer drugs were analyzed. After the isolated EVs were mixed with paraformaldehyde at a ratio of 1:1 (v:v), they were dropped onto silicon wafers and allowed to dry at ambient temperature. Image J was used to process the images, and particle size was assessed. Figure 5.17 shows the EVs obtained from non-treated static2D, static3D, and dynamic conditions. EV sizes for static2D were around 177 nm, while EV sizes for static3D conditions were ~91 nm. Another noticeable difference between two conditions was that EVs collected from the static3D condition were denser and were in a clumped state. This might have hindered some alterations in the NTA analysis. When evaluating the dynamic conditions, EV sizes were around 128 nm and they were less intense, but they were spare.

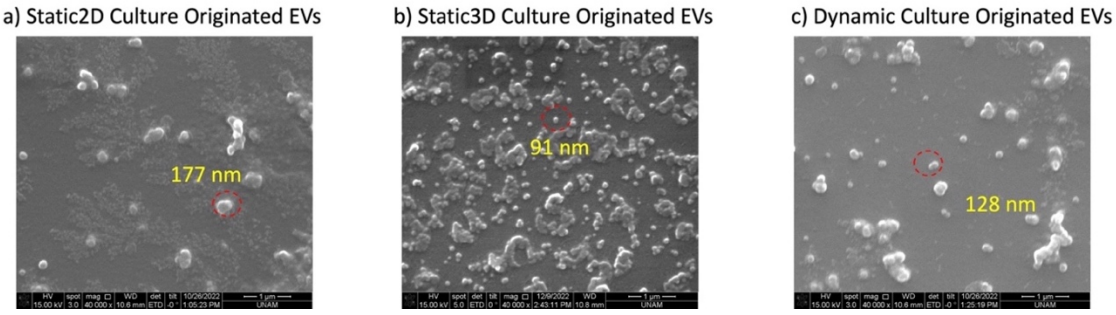


Figure 5.17. SEM image of EVs isolated from a) static2D, b) static3D, and c) dynamic conditions.

In addition, Figure 5.18 shows images of EVs collected from doxorubicin-treated media of three different conditions. Herein, there was a common trend for all three conditions. This trend was the decrease in EV size when the drug dose was increased after the control group. Figure 5.18a shows the images of EVs with an average size of 115 nm isolated from the static2D condition. When drugs were administered from low dose to high dose, the EV size decreased down to 102 nm, 96 nm, 91 nm, and 66 nm, respectively (Figure 5.18 a-e). In Figure 5.18 f-j, the EVs obtained in the static3D environment were presented. Unlike the results of static2D, the EVs were larger in size. With the increase

of the drug dose, herein we also observed the decrease in the size of EVs. The EV size was approximately 178 nm in the control group, and this size decreased down to 148 nm, 142 nm, 138 nm, and 80 nm for increasing drug doses. Finally, EVs isolated from dynamic conditions treated with doxorubicin were imaged (Figure 5.18 k-o). Compared to static3D, EVs from dynamic conditions were smaller in size. The size of EVs was 120 nm in the control group, and decreased to an average of 50 nm when the highest dose of 10^5 nM of doxorubicin was applied.

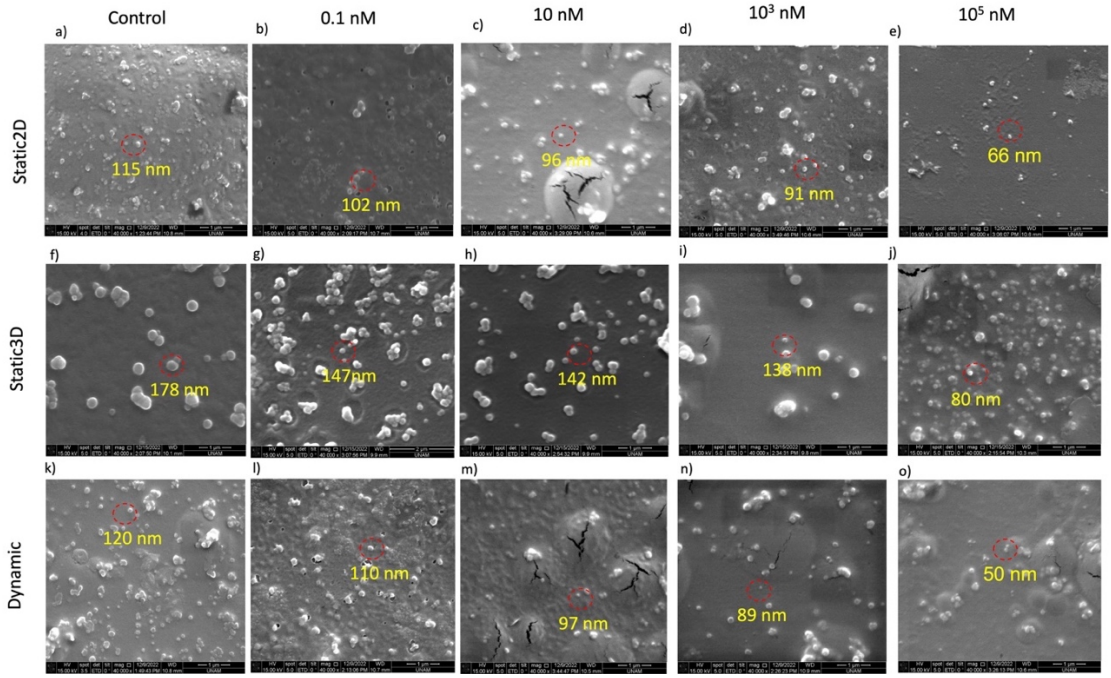


Figure 5.18. SEM images and size information of EVs from three different conditions treated with varying concentrations of doxorubicin.

The EVs isolated from static2D, static3D, and dynamic conditions treated with docetaxel were similar in size compared to the results derived from doxorubicin study. For all three conditions, the largest EV size was observed in the control group, while the smallest sizes were obtained after 10^5 nM of docetaxel was applied (Figure 5.19 a-e). While the EVs of control group in the static2D environment were 117 nm on average, this value decreased to 108 nm after 0.1 nM of docetaxel was introduced. When 10 nM, 10^3 nM, and 10^5 nM docetaxel were applied, the mean EV size were measured as 94 nm,

76 nm, and 61 nm, respectively. The sizes of EVs obtained from the static3D group were larger compared to those obtained from static2D and dynamic conditions. The EV size was around 184 nm in the control group, and it decreased down to 88 nm when 10^5 nM of drug dose was administered (Figure 5.19 d-j). For dynamic conditions, the EV size for the control group and increasing drug doses were found as 155 nm, 140 nm, 118 nm, 82 nm, and 53 nm, respectively (figure 5.19 k-o).

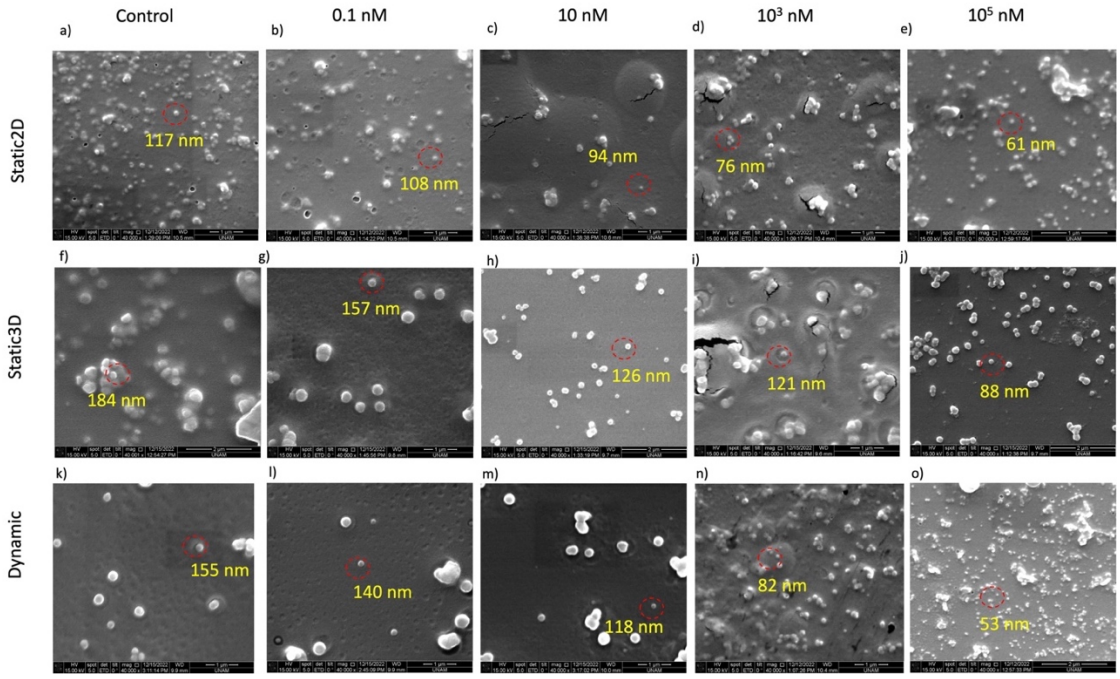


Figure 5.19. SEM images and size information of EVs from three different conditions treated with varying concentrations of docetaxel

5.3 Western Blot Analysis

Western blot analysis was performed by considering two of tetraspanin proteins (CD63 and CD81) located on EV membranes. Briefly, CD63 is strongly N-glycosylated and is known to influence cancer malignancy [145]. Because of the high glycosylation sites and significant amount of post-translational modifications CD63 protein provided a smear signal between 30 and 80 kDa [146]. Western blot analysis of EVs from drug-free (control group) of static2D, static3D, and dynamic conditions was shown in Figure 5.20.

The analysis of CD63 protein was depicted in Figure 5.20a. EVs collected from three different culture conditions resulted in an intense band of about 70 kDa and formed a smear up to 35 kDa. In addition, EVs specifically obtained from the static 3D environment provided a band around 50 kDa. On the other hand, Figure 5.20b shows the western blot analysis of CD81 protein. Usually, CD81 protein provides a band between 20-30 kDa values [147]. In this experiment, CD81 analysis of static2D, static3D, and dynamic conditions resulted in a clear band around 60 kDa and formed a smear image up to 25 kDa (Figure 5.19b). In addition, two distinct bands at 25 kDa and 50 kDa values were observed through the smear for EVs isolated from static3D condition. This could be because of non-specific antibody binding. This high molecular weight may be potentially related to intramolecular disulfide bonds [148]. In summary, distinct bands were observed in EVs from all samples for both analysis of CD63 and CD81 proteins. Consequently, we herein showed the successful isolation of EVs in this study.

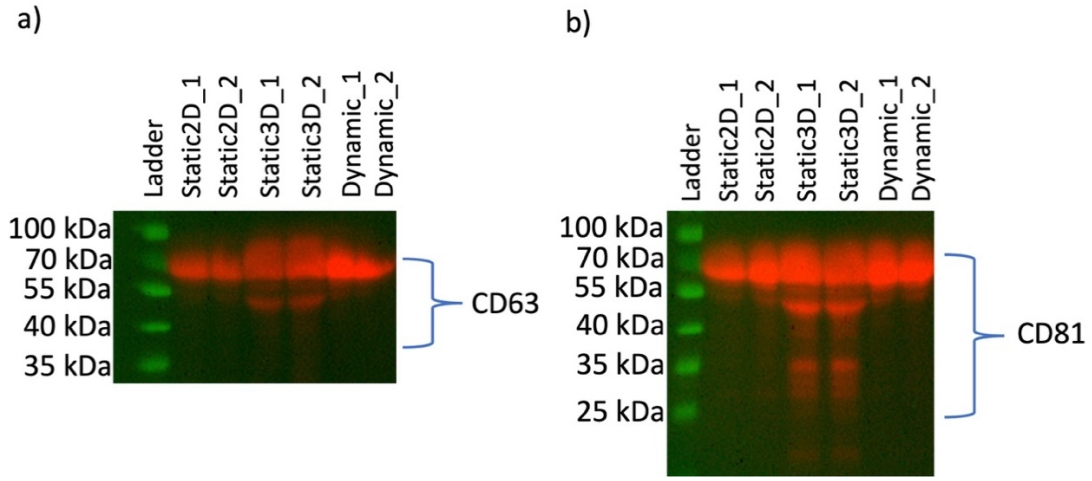


Figure 5.20. Western Blot analysis of static2D, static3D, and dynamic conditions for a) CD63 protein and b) CD81 protein.

On the other hand, western blot analysis was employed for two drug groups (doxorubicin and docetaxel). Figure 5.21 shows the western blot results of EVs from three conditions treated with doxorubicin. Figure 5.21a presents an analysis of CD63 protein. As in drug-free (control group) conditions, all samples provided 60 kDa band. On the other hand, western blot analysis of CD81 protein for the samples treated with doxorubicin showed distinct bands around 60 kDa for all samples (Figure 5.21b).

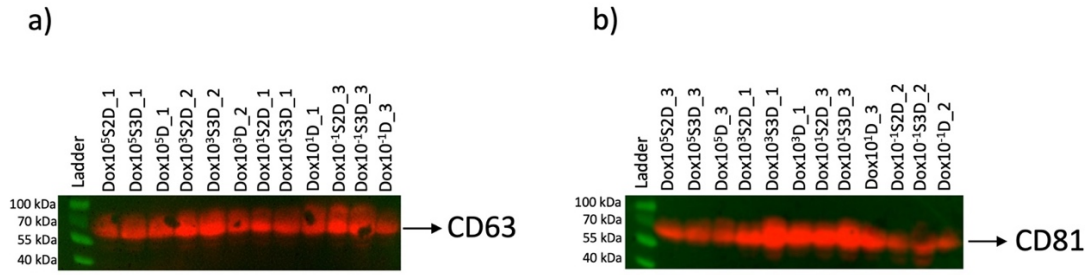


Figure 5.21 Western Blot analysis of a) CD63 protein and b) CD81 protein for EVs isolated from doxorubicin treated cells from static2D, static3D and dynamic conditions.

Finally, western blot analysis was performed for the sample obtained from static2D, static3D, and dynamic conditions treated with docetaxel (Figure 5.22). As a result of the analysis, all samples resulted in a band at 60 kDa for CD63 protein (Figure 5.22a). Likewise, EVs obtained from 10^5 nM, 10^3 nM, 10 nM, and 0.1 nM docetaxel treated condition were observed in the 60 kDa band for CD81 protein (Figure 5.22b).

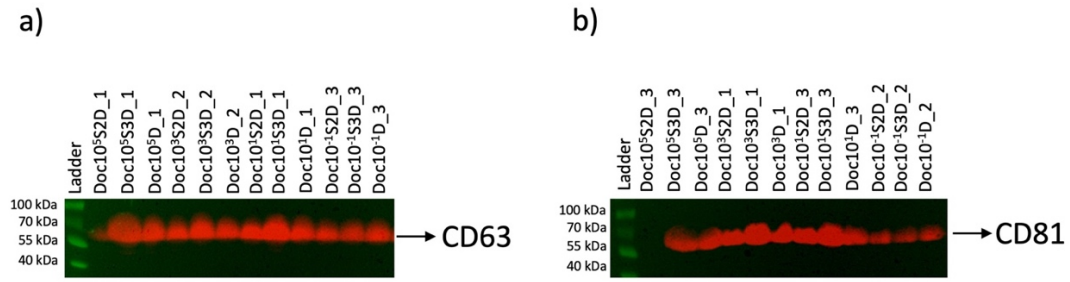


Figure 5.22 Western Blot analysis of a) CD63 protein and b) CD81 protein for EVs isolated from docetaxel treated cells from static2D, static3D and dynamic conditions.

CHAPTER 6

6.CONCLUSION AND FUTURE PROSPECTS

In this study, the effectiveness of microfluidic chip-based systems for monitoring cancer therapy was investigated. For this purpose, static 2D culture performed in a cell flask was used as traditional cell culture method, whereas static 3D culture experiments were operated with the modifications of the flasks with SF. On the other hand, dynamic culture was investigated on a microfluidic chip which was modified with SF under the controlled flow conditions. Besides traditional static2D culture, static3D strategy is desirable to create ECM to accurately mimic tumor microenvironment. In addition, dynamic cultures on a microfluidic chip is a method employed for mimicking both ECM and flow conditions in the body. Typically, in static cultures, cells have limited access to oxygen, nutrition, metabolites, and signal molecules, while in dynamic environments this access is quite high with the flow. It is realized that all these accessibility in the dynamic environment have an effect on tumor epithelial-to-mesenchymal transition (EMT) [140] and chemoresistance [105], and studies are carried out in this direction. Understanding EMT is particularly vital because cancer cells migrate through this transition, leading to metastasis. On the other hand, cells gain resistance to drugs after a certain period of time in patients receiving chemotherapy. Understanding the mechanism of this is very essential because chemoresistance has great potential to cause cancer cells to recur, spread, and eventually lead to mortality. The main purpose of this study is to make investigations using dynamic culture to understand the mechanism behind all these problems and whether traditional static cultures employed in cancer and drug studies are sufficient or have limitations.

The most important part throughout this study is to optimize culturing cells in microfluidic chips. In this regard, studies were first carried out to determine the number of cells to be cultured into microfluidic chips. The studies that started with 3,000 cells/channel ended with the determinations to culture 115,000 cells/channel. The amount of RNA obtained remained very low, as cells that were initially cultured with 3000 cells

did not increase enough at the end of the experiment period. This number was later changed to 30,000 and 60,000 cells/channel. Cells cultivated in these numbers could not have sufficient RNA concentrations at the end of experiment period. Later on, 115,000 cells/channel were cultured, and the cells obtained as a result of the experiments had a sufficient amount of RNA concentration. The microfluidic chip was able to accommodate more than 115,000 cells/channel; yet, sufficient space would not be provided for cells to grow and take 3D structures in that scenario.

The second optimization was performed to effectively remove cells that were cultured on SF from the surface. For this optimization, cells cultured in the channels were removed from the surface using trypsin-EDTA at the end of experiment period. However, it was very crucial the duration of trypsin-EDTA. First, trypsin-EDTA was injected into the channels at a rate of 200 μL/min for 2 minutes. However, this time was not enough for cells to separate from the surface. The time was then increased to 3 minutes. At the end of this period, the microfluidic channels were examined under the microscope, and it was observed that half of the cells remained in the channels. Finally, the time was increased to 5 minutes. At the end of this period, cells were effectively collected from the channels. Longer duration (>5 minutes) was not evaluated because longer trypsin-EDTA exposure induces cellular damage.

The third optimization was to determine the required doses for doxorubicin and docetaxel anti-cancer drugs. In order to choose appropriate doses, a literature review was first conducted and eight different doses were selected (10^6 nM, 10^5 nM, 10^4 nM, 10^3 nM, 10^2 nM, 10 nM, 1 nM, and 0.1 nM). Drug trials were carried out for these chosen doses. In the results, the highest dose of 10^6 nM was really lethal for cells and almost 90% of the cells died, and however, the RNA concentration was not sufficient for downstream analysis. For these reasons, this dose was eliminated from this study. When administrating 10^5 nM of doxorubicin and docetaxel, cells were viable at 40%, and their RNA concentration was sufficient for the other analyses. Therefore, we applied up to 10^5 nM of drug dose as the highest value for the experiments. The other doses were evaluated sequentially; however, 10-fold difference between drug concentrations did not cause a significant difference in cell viability. Therefore, it was decided to be 100-fold between drug concentrations. Accordingly, the doses were determined as 10^5 nM, 10^3 nM, 10 nM, and 0.1 nM for both anti-cancer drugs.

Once all these optimizations were completed, we evaluated the effect of cell culture conditions, i.e., static2D, static3D and dynamic conditions. The aim here was to understand whether the flow would have an effect on gene expression. The 7-day culture period was completed without administering any anti-cancer drug to the cells initially cultured under three conditions. At the end of this experiment period, RNA was isolated from the cells, cDNA synthesis and gene expression analysis were performed. The genes studied here were *EpCAM* and *CK-18*—highly expressed in MCF-7 cells, and they are thought to be involved in EMT. As a result of this analysis, interpretations would be made about EMT according to whether there was a difference in gene expressions or not. As depicted in Figure 3.7, *CK-18* expression was higher than *EpCAM* expression level in cells cultured under static2D and static3D conditions. On the other hand, *CK-18* expression was lower than *EpCAM* expression in cells cultured under dynamic conditions. In the literature, it has been reported that the downregulation of *CK-18* results in *EpCAM* upregulation in breast cancer, which in turn stimulates EMT and stemness. As a result of this experiment, we herein demonstrated that the flow on microfluidic chip had an effect on gene expression; potentially impacted on EMT; and played a role in metastasis.

In the Chapter 4, it was aimed to investigate whether cells develop any chemoresistance under the flow using doxorubicin and docetaxel. For these reasons, cells cultured in static2D, static3D, and dynamic conditions were treated with drugs for 72 hours on the fourth day after culturing. As a result of the experiment, the viability of cells, which were administered with different doses of doxorubicin under static2D conditions, decreased down to 52% at the highest dose of doxorubicin (Figure 4.1). This viability rate was 61% for cells cultured in static 3D conditions at a dose of 10^5 nM of doxorubicin (Figure 4.3). Finally, in the experiments performed under dynamic conditions, the viability of cells was 80% in the control group (non-treated group), while this rate decreased down to 40% when 10^5 nM of drug was administered. In summary, when the viability rates obtained from three conditions were compared, the most effective system in reducing the viability of cells were dynamic conditions (Figure 4.7). This could be due to the flow condition on the chip. In addition, cells located on the outer layer of 3D structure died when exposed to the drug, and the flow in the system removed dead cells from the environment due to continuous refreshing of the media in the channel. Living cells remained stable on the 3D surface and interacted with the drug, and hence, the

viability rate decreased. Finally, the viability rate was found to be the highest in static3D conditions, and this could be because cells remaining on the outer layer of 3D structure interacted with the drugs, and however, they were not able to be removed from the environment. For this reason, intact cells inside the 3D structure were not able to access the drug and preserve their viability. Similar to doxorubicin experiments, we observed the comparable trends for docetaxel. In Figure 4.9, cells cultured in static2D conditions were treated with docetaxel. The survival rate, which was 84% in the control group, decreased to 55% at the highest drug dose. In static3D conditions, this decrease was from 83% to 62% (Figure 4.11). In the results of dynamic conditions, the viability, we calculated 80% of viability in the control group, and this decreased down to 43% when 10^5 nM of docetaxel was applied (Figure 4.13). Considering the effect of the three groups on viability, the lowest viability rate belongs to the dynamic conditions as stated in doxorubicin. This was followed by static2D and static3D (Figure 4.15).

Gene expression analysis was performed for cells obtained from three different conditions after viability experiments. In these analyses, *MDR-1* and *BCRP* genes were also examined in addition to *EpCAM* and *CK-18*. Figure 4.17 shows the expression results obtained for four different genes under doxorubicin treatment. No changes in expression of all four genes were observed for cells cultured under static2D conditions. In static3D cells, on the other hand, as the drug dose increased, *CK-18* expression level decreased and *EpCAM* level increased. While no difference was observed for the *MDR-1* gene, the expression of *BCRP* increased at a dose of 10^3 nM of doxorubicin. When assessing the results of dynamic conditions, *CK-18* gene expression decreased in proportional to dose increments, while *EpCAM* expression amplified. In addition, an increase in *MDR-1* and *BCRP* gene expressions was also observed. Consequently, we herein observed that the flow had an effect on chemoresistance. It was also reported in a study that downregulation of *CK-18* level enhances the expression of *BCRP*-mediated *MDR-1* [149]. In Figure 4.18, *CK-18, EpCAM, MDR-1* and *BCRP* gene expression analyzes of the groups treated with docetaxel were examined. A stable trend is observed for all four genes for the static2D condition. While a stable trend was observed in *CK-18* and *MDR-1* gene expression for static 3D conditions, an increase in gene levels was observed in *EpCAM* and *BCRP* genes in 10^5 nM dose docetaxel groups. Finally, when the dynamic conditions under docetaxel were examined, it was observed that the *CK-18* level decreased while the drug dose was

increased. Contrary to *CK-18*, an increase was observed in *EpCAM* level. In addition, gene expression is gradually increased in *MDR-1* and *BCRP* genes from the start of drug administration.

Moreover, EVs isolated from each experimental group were analyzed with NTA. The mean, mode, and EV numbers were evaluated for non-treated static2D, static3D, and dynamic conditions. Figure 5.2a shows the mean values of EVs isolated from three different conditions. Although there was no statistical difference between the values, the variance was less in the group obtained from the dynamic conditions, and the mean values were close to each other. Considering the mode values, a significant difference was observed between static3D and dynamic conditions (Figure 5.2b). Finally, when the number of EVs was compared, there was a statistically significant difference between static2D and static3D (Figure 5.2c). The mean, mode, and number values of EVs isolated from cells cultured in static2D, static3D, and dynamic conditions treated with doxorubicin were compared in Figure 5.9. The comparison of mean values was shown in Figure 5.9a, and a significant difference was observed between static2D and static3D in the control group. When the mode values were compared, there was a difference between static2D and static3D in the control group, and there was a statistically significant difference found between static2D and static3D in the group given 10^3 nM of doxorubicin. In the control group, there was a considerable difference between static3D and dynamic conditions. In addition, a statistically difference between static2D and static3D were observed at doxorubicin concentrations of 10 nM, 10^3 nM, and 10^5 nM. (Figure 5.9c). Moreover, at both 10 nM and 10^5 nM of doses, a significant difference was realized between static3D and dynamic conditions. Finally, we compared EVs isolated from all conditions treated with docetaxel. The comparison of mean values was shown in Figure 5.16a. As a result of the analysis, a significant difference was observed between the static 3D and dynamic conditions in the groups given the 10 nM dose of docetaxel. No significant difference was observed between the mode values as shown in Figure 5.16b. Considering the EV numbers, there was a difference between static3D and dynamic conditions at 0.1 nM and 10^5 nM of doses, as well as between static2D and static3D at 10^5 nM of dose.

Moreover, in this study, a microfluidic chip was utilized to isolate EVs, and it provided a faster, facile-to-use solution along with low sample volume compared to

traditional EV isolation methods as detailed above. These chips have also been shown to effectively isolate EVs from cancer cells. Figure 5.17 showed EVs with an average size of 177 nm, 91 nm, and 128 nm isolated from control groups (non-treated) of static2D, static3D, and dynamic conditions, respectively. EVs isolated from static environments appeared to be more clumped, while those isolated from dynamic conditions had less clumpy structure. Figure 5.18 shows SEM images of EVs from three conditions treated with doxorubicin. In general, for the same experimental groups, the sizes of EVs obtained from static2D and dynamic conditions were closer to each other, while those obtained from static3D were larger. In general, after the control group, the size of EVs decreased as the drug dose increased. These results might have differed from the mean and mode values in NTA analyses, since small particles were more difficult to be captured by this instrument due to their clump state. Moreover, Figure 5.19 shows SEM images of EVs isolated from static2D, static3D and dynamic conditions treated with docetaxel. As with doxorubicin, the size of EVs decreased as the dose increased. Static3D had the highest size for each group.

Western blot analysis was performed to confirm the success of isolated EVs. In Figure 5.20, we presented western blot results showing CD63 and CD81 proteins for control (non-treated) groups. As expected, CD63 gave a strong band between 30 and 80 kDa. In particular, it gave a strong band for each group with a value of 70 kDa and also formed smears up to 35 kDa. This was because CD63 has highly N-glycosylated sites. On the other hand, while the CD81 protein has a value of 20-30 kDa, a band of around 60 kDa was observed as a result of western blot analysis, pointing out that potential intramolecular disulfide bonds. Figure 5.21 and Figure 5.22 show EVs isolated from cultures treated with doxorubicin and docetaxel, respectively. In the groups treated with doxorubicin, CD63 and CD81 proteins showed a band of 60 kDa (Figure 5.21). On the other hand, in the groups treated with docetaxel, we observed 60 kDa of bands for CD63 and CD81 proteins.

In a nutshell, in this thesis, we demonstrated a cell culture method utilizing in a microfluidic chip for 3D of cell culture under flow effects, which differs than conventional culture methods. Consequently, our goal was to imitate tumor microenvironments with the use of a microfluidic chip that mimics the flow inside the body and the formation of an original environment using an inexpensive, readily

available, and simple-to-modify SF biomaterial. As a result, we paved the way with a different approach to cancer research and chemoresistance studies. In near future, gene expression analyses of the isolated EVs would be examined. The same studies would be also performed in normal breast cells and the gene expressions of EVs would be compared subsequently. Therefore, it would be investigated whether EVs would be a vital biomarker for cancer and whether they could be a promising alternative for early diagnosis of cancer.

Bibliography

[1] H. Sung *et al.*, "Global Cancer Statistics 2020: GLOBOCAN Estimates of Incidence and Mortality Worldwide for 36 Cancers in 185 Countries," *CA Cancer J Clin*, vol. 71, no. 3, pp. 209–249, May 2021, doi: 10.3322/CAAC.21660.

[2] D. Hanahan and R. A. Weinberg, "Hallmarks of cancer: The next generation," *Cell*, vol. 144, no. 5, pp. 646–674, Mar. 2011, doi: 10.1016/J.CELL.2011.02.013.

[3] D. Hanahan and R. A. Weinberg, "The hallmarks of cancer," *Cell*, vol. 100, no. 1, pp. 57–70, Jan. 2000, doi: 10.1016/S0092-8674(00)81683-9.

[4] D. Hanahan, "Hallmarks of Cancer: New Dimensions," *Cancer Discov*, vol. 12, no. 1, pp. 31–46, Jan. 2022, doi: 10.1158/2159-8290.CD-21-1059.

[5] D. Hanahan, "Hallmarks of Cancer: New Dimensions," *Cancer Discov*, vol. 12, no. 1, pp. 31–46, Jan. 2022, doi: 10.1158/2159-8290.CD-21-1059.

[6] G. M. Cooper, "The Development and Causes of Cancer," 2000, Accessed: Dec. 07, 2022. [Online]. Available: https://www.ncbi.nlm.nih.gov/books/NBK9963/

[7] A. Patel, "Benign vs Malignant Tumors," *JAMA Oncol*, vol. 6, no. 9, pp. 1488–1488, Sep. 2020, doi: 10.1001/JAMAONCOL.2020.2592.

[8] T. Sinha, "Canc Therapy & Oncol Int J Tumors: Benign and Malignant Cancer Therapy & Oncology International Journal," *Canc Therapy & Oncol Int J*, vol. 10, no. 3, 2018, doi: 10.19080/CTOIJ.2018.10.555790.

[9] T. N. Seyfried and L. C. Huysentruyt, "On the Origin of Cancer Metastasis," *Crit Rev Oncog*, vol. 18, no. 1–2, p. 43, 2013, doi: 10.1615/CRITREVONCOG.V18.I1-2.40.

[10] J. Fares, M. Y. Fares, H. H. Khachfe, H. A. Salhab, and Y. Fares, "Molecular principles of metastasis: a hallmark of cancer revisited," *Signal Transduct Target Ther*, vol. 5, no. 1, Dec. 2020, doi: 10.1038/S41392-020-0134-X.

[11] "Benign Tumors," *Oral Radiol*, pp. 359–401, Jan. 2014, doi: 10.1016/B978-0-323-09633-1.00022-5.

[12] J. Vijg, "From DNA damage to mutations: All roads lead to aging," *Ageing Res Rev*, vol. 68, p. 101316, Jul. 2021, doi: 10.1016/J.ARR.2021.101316.

[13] N. Chatterjee and G. C. Walker, "Mechanisms of DNA damage, repair and mutagenesis," *Environ Mol Mutagen*, vol. 58, no. 5, p. 235, Jun. 2017, doi: 10.1002/EM.22087.

[14] J. L. Barnes, M. Zubair, K. John, M. C. Poirier, and F. L. Martin, "Carcinogens and DNA damage," *Biochem Soc Trans*, vol. 46, no. 5, p. 1213, Oct. 2018, doi: 10.1042/BST20180519.

[15] D. Zella and R. C. Gallo, "Viruses and Bacteria Associated with Cancer: An Overview," *Viruses*, vol. 13, no. 6, Jun. 2021, doi: 10.3390/V13061039.

[16] K. I. Avgerinos, N. Spyrou, C. S. Mantzoros, and M. Dalamaga, "Obesity and cancer risk: Emerging biological mechanisms and perspectives," *Metabolism*, vol. 92, pp. 121–135, Mar. 2019, doi: 10.1016/J.METABOL.2018.11.001.

[17] C. Pucci, C. Martinelli, and G. Ciofani, "Innovative approaches for cancer treatment: current perspectives and new challenges," *Ecancermedicalscience*, vol. 13, Sep. 2019, doi: 10.3332/ECANCER.2019.961.

[18] "Advancing Cancer Therapy," *Nature Cancer 2021 2:3*, vol. 2, no. 3, pp. 245–246, Mar. 2021, doi: 10.1038/s43018-021-00192-x.

[19] I. S. Haslam and E. Smart, “Chemotherapy-Induced Hair Loss: The Use of Biomarkers for Predicting Alopecic Severity and Treatment Efficacy,” *Biomark Insights*, vol. 14, Apr. 2019, doi: 10.1177/1177271919842180.
[20] N. Vasan, J. Baselga, and D. M. Hyman, “A view on drug resistance in cancer,” *Nature 2019 575:7782*, vol. 575, no. 7782, pp. 299–309, Nov. 2019, doi: 10.1038/s41586-019-1730-1.
[21] N. Vasan, J. Baselga, and D. M. Hyman, “A view on drug resistance in cancer,” *Nature 2019 575:7782*, vol. 575, no. 7782, pp. 299–309, Nov. 2019, doi: 10.1038/s41586-019-1730-1.
[22] F. Bragheri, R. M. Vázquez, and R. Osellame, “Microfluidics,” *Three-Dimensional Microfabrication Using Two-Photon Polymerization*, pp. 493–526, Jan. 2020, doi: 10.1016/B978-0-12-817827-0.00057-6.
[23] G. M. Whitesides, “The origins and the future of microfluidics,” *Nature 2006 442:7101*, vol. 442, no. 7101, pp. 368–373, Jul. 2006, doi: 10.1038/nature05058.
[24] J. W. Hong and S. R. Quake, “Integrated nanoliter systems,” *Nature Biotechnology 2003 21:10*, vol. 21, no. 10, pp. 1179–1183, Sep. 2003, doi: 10.1038/nbt871.
[25] G. A. Akceoglu, Y. Saylan, and F. Inci, “A Snapshot of Microfluidics in Point-of-Care Diagnostics: Multifaceted Integrity with Materials and Sensors,” *Adv Mater Technol*, vol. 6, no. 7, p. 2100049, Jul. 2021, doi: 10.1002/ADMT.202100049.
[26] S. M. Scott and Z. Ali, “Fabrication Methods for Microfluidic Devices: An Overview,” *Micromachines (Basel)*, vol. 12, no. 3, Mar. 2021, doi: 10.3390/MI12030319.
[27] R. S. Kane, A. D. Stroock, N. Li Jeon, D. E. Ingber, and G. M. Whitesides, “Soft Lithography and Microfluidics,” *Optical Biosensors*, pp. 571–595, 2002, doi: 10.1016/B978-044450974-1/50018-5.
[28] G. S. Fiorini and D. T. Chiu, “Disposable microfluidic devices: Fabrication, function, and application,” *Biotechniques*, vol. 38, no. 3, pp. 429–446, May 2005, doi: 10.2144/05383RV02/ASSET/IMAGES/LARGE/FIGURE7.JPEG.
[29] J. Ma, L. Jiang, X. Pan, H. Ma, B. Lin, and J. Qin, “A simple photolithography method for microfluidic device fabrication using sunlight as UV source,” *Microfluid Nanofluidics*, vol. 9, no. 6, pp. 1247–1252, Dec. 2010, doi: 10.1007/S10404-010-0630-3/FIGURES/4.
[30] T. Nguyen, T. Sarkar, T. Tran, S. M. Moinuddin, D. Saha, and F. Ahsan, “Multilayer Soft Photolithography Fabrication of Microfluidic Devices Using a Custom-Built Wafer-Scale PDMS Slab Aligner and Cost-Efficient Equipment,” *Micromachines (Basel)*, vol. 13, no. 8, p. 1357, Aug. 2022, doi: 10.3390/MI13081357/S1.
[31] Y.-J. ; Juang, Y.-J. Chiu, Y.-J. Juang, and Y.-J. Chiu, “Fabrication of Polymer Microfluidics: An Overview,” *Polymers 2022, Vol. 14, Page 2028*, vol. 14, no. 10, p. 2028, May 2022, doi: 10.3390/POLYM14102028.
[32] S. Halldorsson, E. Lucumi, R. Gómez-Sjöberg, and R. M. T. Fleming, “Advantages and challenges of microfluidic cell culture in polydimethylsiloxane devices,” *Biosens Bioelectron*, vol. 63, pp. 218–231, Jan. 2015, doi: 10.1016/J.BIOS.2014.07.029.
[33] A. D. Castiaux, D. M. Spence, and R. S. Martin, “Review of 3D cell culture with analysis in microfluidic systems,” *Analytical Methods*, vol. 11, no. 33, pp. 4220–4232, Aug. 2019, doi: 10.1039/C9AY01328H.

[34] S. T. Sanjay *et al.*, "Recent advances of controlled drug delivery using microfluidic platforms," *Adv Drug Deliv Rev*, vol. 128, pp. 3–28, Mar. 2018, doi: 10.1016/J.ADDR.2017.09.013.
[35] S. Sachdeva, R. W. Davis, and A. K. Saha, "Microfluidic Point-of-Care Testing: Commercial Landscape and Future Directions," *Front Bioeng Biotechnol*, vol. 8, p. 602659, Jan. 2020, doi: 10.3389/FBIOE.2020.602659.
[36] Z. Zhang and S. Nagrath, "Microfluidics and Cancer: Are we there yet?," *Biomed Microdevices*, vol. 15, no. 4, p. 595, Aug. 2013, doi: 10.1007/S10544-012-9734-8.
[37] R. L. Siegel, K. D. Miller, H. E. Fuchs, and A. Jemal, "Cancer statistics, 2022," *CA Cancer J Clin*, vol. 72, no. 1, pp. 7–33, Jan. 2022, doi: 10.3322/CAAC.21708.
[38] F. Alexis, J. W. Rhee, J. P. Richie, A. F. Radovic-Moreno, R. Langer, and O. C. Farokhzad, "New frontiers in nanotechnology for cancer treatment," *Urologic Oncology: Seminars and Original Investigations*, vol. 26, no. 1, pp. 74–85, Jan. 2008, doi: 10.1016/J.UROLONC.2007.03.017.
[39] R. L. Siegel, K. D. Miller, and A. Jemal, "Cancer statistics, 2016," *CA Cancer J Clin*, vol. 66, no. 1, pp. 7–30, Jan. 2016, doi: 10.3322/CAAC.21332.
[40] K. D. Miller *et al.*, "Cancer treatment and survivorship statistics, 2016," *CA Cancer J Clin*, vol. 66, no. 4, pp. 271–289, Jul. 2016, doi: 10.3322/CAAC.21349.
[41] R. Seigneuric *et al.*, "From Nanotechnology to Nanomedicine: Applications to Cancer Research," *Curr Mol Med*, vol. 10, no. 7, pp. 640–652, 2010.
[42] T. Fabian, P. Fejerdy, and P. Csermely, "Salivary Genomics, Transcriptomics and Proteomics: The Emerging Concept of the Oral Ecosystem and their Use in the Early Diagnosis of Cancer and other Diseases," *Curr Genomics*, vol. 9, no. 1, p. 11, Mar. 2008, doi: 10.2174/138920208783884900.
[43] C. H. Wong and Y. C. Chen, "Clinical significance of exosomes as potential biomarkers in cancer," *World J Clin Cases*, vol. 7, no. 2, p. 171, Jan. 2019, doi: 10.12998/WJCC.V7.I2.171.
[44] J. Marrugo-Ramírez, M. Mir, and J. Samitier, "Blood-Based Cancer Biomarkers in Liquid Biopsy: A Promising Non-Invasive Alternative to Tissue Biopsy," *International Journal of Molecular Sciences 2018, Vol. 19, Page 2877*, vol. 19, no. 10, p. 2877, Sep. 2018, doi: 10.3390/IJMS19102877.
[45] R. T. Krivacic *et al.*, "A rare-cell detector for cancer," *Proc Natl Acad Sci U S A*, vol. 101, no. 29, pp. 10501–10504, Jul. 2004, doi: 10.1073/PNAS.0404036101/ASSET/168B85C2-E1B1-4573-8D58-B3405A620CF5/ASSETS/GRAPHIC/ZPQ0290454420002.JPEG.
[46] J. R. Heath and M. E. Davis, "Nanotechnology and Cancer," *Annu Rev Med*, vol. 59, p. 251, 2008, doi: 10.1146/ANNUREV.MED.59.061506.185523.
[47] P. K. Sorger, "Microfluidics closes in on point-of-care assays," *Nature Biotechnology 2008 26:12*, vol. 26, no. 12, pp. 1345–1346, Dec. 2008, doi: 10.1038/nbt1208-1345.
[48] Z. Lin, G. Luo, W. Du, T. Kong, C. Liu, and Z. Liu, "Recent Advances in Microfluidic Platforms Applied in Cancer Metastasis: Circulating Tumor Cells' (CTCs) Isolation and Tumor-On-A-Chip," *Small*, vol. 16, no. 9, Mar. 2020, doi: 10.1002/SMLL.201903899.
[49] D. Caballero, M. A. Luque-González, R. L. Reis, and S. C. Kundu, "Microfluidic systems in cancer research," *Biomaterials for 3D Tumor Modeling*, pp. 331–377, Jan. 2020, doi: 10.1016/B978-0-12-818128-7.00015-0.

[50] G. A. van Norman, “Limitations of Animal Studies for Predicting Toxicity in Clinical Trials: Is it Time to Rethink Our Current Approach?,” *JACC Basic Transl Sci*, vol. 4, no. 7, p. 845, Nov. 2019, doi: 10.1016/J.JACBTS.2019.10.008.

[51] S. Azadi, H. Aboulkheyr Es, A. Kulasinghe, P. Bordhan, and M. Ebrahimi Warkiani, “Application of microfluidic technology in cancer research and therapy,” *Adv Clin Chem*, vol. 99, pp. 193–235, Jan. 2020, doi: 10.1016/BS.ACC.2020.02.012.

[52] T. Yao and Y. Asayama, “Animal-cell culture media: History, characteristics, and current issues,” *Reprod Med Biol*, vol. 16, no. 2, p. 99, Apr. 2017, doi: 10.1002/RMB2.12024.

[53] R. Edmondson, J. J. Broglie, A. F. Adcock, and L. Yang, “Three-Dimensional Cell Culture Systems and Their Applications in Drug Discovery and Cell-Based Biosensors,” *Assay Drug Dev Technol*, vol. 12, no. 4, p. 207, May 2014, doi: 10.1089/ADT.2014.573.

[54] D. Lv, Z. Hu, L. Lu, H. Lu, and X. Xu, “Three-dimensional cell culture: A powerful tool in tumor research and drug discovery,” *Oncol Lett*, vol. 14, no. 6, pp. 6999–7010, Dec. 2017, doi: 10.3892/OL.2017.7134/HTML.

[55] E. C. Costa, A. F. Moreira, D. de Melo-Diogo, V. M. Gaspar, M. P. Carvalho, and I. J. Correia, “3D tumor spheroids: an overview on the tools and techniques used for their analysis,” *Biotechnol Adv*, vol. 34, no. 8, pp. 1427–1441, Dec. 2016, doi: 10.1016/J.BIOTECHADV.2016.11.002.

[56] H. B. Frieboes, X. Zheng, C. H. Sun, B. Tromberg, R. Gatenby, and V. Cristini, “An Integrated Computational/Experimental Model of Tumor Invasion,” *Cancer Res*, vol. 66, no. 3, pp. 1597–1604, Feb. 2006, doi: 10.1158/0008-5472.CAN-05-3166.

[57] J. Lee, M. J. Cuddihy, and N. A. Kotov, “Three-Dimensional Cell Culture Matrices: State of the Art,” *https://home.liebertpub.com/teb*, vol. 14, no. 1, pp. 61–86, Mar. 2008, doi: 10.1089/TEB.2007.0150.

[58] M. Kapałczyńska *et al.*, “2D and 3D cell cultures – a comparison of different types of cancer cell cultures,” *Arch Med Sci*, vol. 14, no. 4, p. 910, 2018, doi: 10.5114/AOMS.2016.63743.

[59] F. Pampaloni, E. G. Reynaud, and E. H. K. Stelzer, “The third dimension bridges the gap between cell culture and live tissue,” *Nature Reviews Molecular Cell Biology 2007 8:10*, vol. 8, no. 10, pp. 839–845, Oct. 2007, doi: 10.1038/nrm2236.

[60] M. Ravi, V. Paramesh, S. R. Kaviya, E. Anuradha, and F. D. Paul Solomon, “3D Cell Culture Systems: Advantages and Applications,” *J Cell Physiol*, vol. 230, no. 1, pp. 16–26, Jan. 2015, doi: 10.1002/JCP.24683.

[61] J. C. Fontoura *et al.*, “Comparison of 2D and 3D cell culture models for cell growth, gene expression and drug resistance,” *Materials Science and Engineering: C*, vol. 107, p. 110264, Feb. 2020, doi: 10.1016/J.MSEC.2019.110264.

[62] S. A. Langhans, “Three-dimensional in vitro cell culture models in drug discovery and drug repositioning,” *Front Pharmacol*, vol. 9, no. JAN, p. 6, Jan. 2018, doi: 10.3389/FPHAR.2018.00006/BIBTEX.

[63] T. R. Sodunke, K. K. Turner, S. A. Caldwell, K. W. McBride, M. J. Reginato, and H. M. Noh, “Micropatterns of Matrigel for three-dimensional epithelial cultures,” *Biomaterials*, vol. 28, no. 27, pp. 4006–4016, Sep. 2007, doi: 10.1016/J.BIOMATERIALS.2007.05.021.

[64] C. Jensen and Y. Teng, “Is It Time to Start Transitioning From 2D to 3D Cell Culture?,” *Front Mol Biosci*, vol. 7, p. 33, Mar. 2020, doi: 10.3389/FMOLB.2020.00033/BIBTEX.

[65] B. B. Aggarwal, D. Danda, S. Gupta, and P. Gehlot, “Models for prevention and treatment of cancer: problems vs promises,” *Biochem Pharmacol*, vol. 78, no. 9, pp. 1083–1094, Nov. 2009, doi: 10.1016/J.BCP.2009.05.027.

[66] S. F. Chen, Y. C. Chang, S. Nieh, C. L. Liu, C. Y. Yang, and Y. S. Lin, “Nonadhesive Culture System as a Model of Rapid Sphere Formation with Cancer Stem Cell Properties,” *PLoS One*, vol. 7, no. 2, p. e31864, Feb. 2012, doi: 10.1371/JOURNAL.PONE.0031864.

[67] B. M. Baker and C. S. Chen, “Deconstructing the third dimension-how 3D culture microenvironments alter cellular cues,” *J Cell Sci*, vol. 125, no. 13, pp. 3015–3024, Jul. 2012, doi: 10.1242/JCS.079509/258092/AM/DECONSTRUCTING-THE-THIRD-DIMENSION-HOW-3D-CULTURE.

[68] S. Khetan and J. A. Burdick, “Patterning network structure to spatially control cellular remodeling and stem cell fate within 3-dimensional hydrogels,” *Biomaterials*, vol. 31, no. 32, pp. 8228–8234, Nov. 2010, doi: 10.1016/J.BIOMATERIALS.2010.07.035.

[69] S. Breslin and L. O’Driscoll, “Three-dimensional cell culture: the missing link in drug discovery,” *Drug Discov Today*, vol. 18, no. 5–6, pp. 240–249, Mar. 2013, doi: 10.1016/J.DRUDIS.2012.10.003.

[70] C. P. Soares, V. Midlej, M. E. W. de Oliveira, M. Benchimol, M. L. Costa, and C. Mermelstein, “2D and 3D-Organized Cardiac Cells Shows Differences in Cellular Morphology, Adhesion Junctions, Presence of Myofibrils and Protein Expression,” *PLoS One*, vol. 7, no. 5, p. e38147, May 2012, doi: 10.1371/JOURNAL.PONE.0038147.

[71] J. A. Hickman *et al.*, “Three-dimensional models of cancer for pharmacology and cancer cell biology: Capturing tumor complexity in vitro/ex vivo,” *Biotechnol J*, vol. 9, no. 9, pp. 1115–1128, Sep. 2014, doi: 10.1002/BIOT.201300492.

[72] Y. Park, K. M. Huh, and S. W. Kang, “Applications of Biomaterials in 3D Cell Culture and Contributions of 3D Cell Culture to Drug Development and Basic Biomedical Research,” *Int J Mol Sci*, vol. 22, no. 5, pp. 1–21, Mar. 2021, doi: 10.3390/IJMS22052491.

[73] B. B. Mandal and S. C. Kundu, “Cell proliferation and migration in silk fibroin 3D scaffolds,” *Biomaterials*, vol. 30, no. 15, pp. 2956–2965, May 2009, doi: 10.1016/J.BIOMATERIALS.2009.02.006.

[74] W. Sun, D. A. Gregory, M. A. Tomeh, and X. Zhao, “Silk Fibroin as a Functional Biomaterial for Tissue Engineering,” *Int J Mol Sci*, vol. 22, no. 3, pp. 1–28, Feb. 2021, doi: 10.3390/IJMS22031499.

[75] T. L. Liu *et al.*, “Cytocompatibility of regenerated silk fibroin film: a medical biomaterial applicable to wound healing,” *J Zhejiang Univ Sci B*, vol. 11, no. 1, p. 10, Jan. 2010, doi: 10.1631/JZUS.B0900163.

[76] Q. Wang, G. Han, S. Yan, and Q. Zhang, “3D Printing of Silk Fibroin for Biomedical Applications,” *Materials 2019, Vol. 12, Page 504*, vol. 12, no. 3, p. 504, Feb. 2019, doi: 10.3390/MA12030504.

[77] S. S. Silva *et al.*, “2.11 Polymers of Biological Origin,” *Comprehensive Biomaterials II*, pp. 228–252, Jan. 2017, doi: 10.1016/B978-0-12-803581-8.10134-1.

[78] M. A. di Bella, “Overview and Update on Extracellular Vesicles: Considerations on Exosomes and Their Application in Modern Medicine,” *Biology 2022, Vol. 11, Page 804*, vol. 11, no. 6, p. 804, May 2022, doi: 10.3390/BIOLOGY11060804.
[79] M. P. Zaborowski, L. Balaj, X. O. Breakefield, and C. P. Lai, “Editor’s Choice: Extracellular Vesicles: Composition, Biological Relevance, and Methods of Study,” *Bioscience*, vol. 65, no. 8, p. 783, Aug. 2015, doi: 10.1093/BIOSCI/BIV084.
[80] M. Battistelli and E. Falcieri, “Apoptotic Bodies: Particular Extracellular Vesicles Involved in Intercellular Communication,” *Biology (Basel)*, vol. 9, no. 1, Jan. 2020, doi: 10.3390/BIOLOGY9010021.
[81] N. Gebara, A. Rossi, R. Skovronova, J. M. Aziz, A. Asthana, and B. Bussolati, “Extracellular Vesicles, Apoptotic Bodies and Mitochondria: Stem Cell Bioproducts for Organ Regeneration,” *Curr Transplant Rep*, vol. 7, no. 2, pp. 105–113, Jun. 2020, doi: 10.1007/S40472-020-00282-2/TABLES/2.
[82] A. lie Ståhl, K. Johansson, M. Mossberg, R. Kahn, and D. Karpman, “Exosomes and microvesicles in normal physiology, pathophysiology, and renal diseases,” *Pediatr Nephrol*, vol. 34, no. 1, p. 11, Jan. 2019, doi: 10.1007/S00467-017-3816-Z.
[83] A. Yokoi and T. Ochiya, “Exosomes and extracellular vesicles: Rethinking the essential values in cancer biology,” *Semin Cancer Biol*, vol. 74, pp. 79–91, Sep. 2021, doi: 10.1016/J.SEMCANCER.2021.03.032.
[84] L. M. Doyle and M. Z. Wang, “Overview of Extracellular Vesicles, Their Origin, Composition, Purpose, and Methods for Exosome Isolation and Analysis,” *Cells*, vol. 8, no. 7, Jul. 2019, doi: 10.3390/CELLS8070727.
[85] D. Zheng *et al.*, “The Role of Exosomes and Exosomal MicroRNA in Cardiovascular Disease,” *Front Cell Dev Biol*, vol. 8, p. 1810, Jan. 2021, doi: 10.3389/FCELL.2020.616161/BIBTEX.
[86] M. Tkach and C. Théry, “Communication by Extracellular Vesicles: Where We Are and Where We Need to Go,” *Cell*, vol. 164, no. 6, pp. 1226–1232, Mar. 2016, doi: 10.1016/j.cell.2016.01.043.
[87] C. Théry, “Exosomes: secreted vesicles and intercellular communications,” *F1000 Biol Rep*, vol. 3, no. 1, p. 15, Jul. 2011, doi: 10.3410/B3-15.
[88] M. Simons and G. Raposo, “Exosomes – vesicular carriers for intercellular communication,” *Curr Opin Cell Biol*, vol. 21, no. 4, pp. 575–581, Aug. 2009, doi: 10.1016/J.CEB.2009.03.007.
[89] Z. Andreu and M. Yáñez-Mó, “Tetraspanins in extracellular vesicle formation and function,” *Front Immunol*, vol. 5, no. SEP, p. 442, Sep. 2014, doi: 10.3389/FIMMU.2014.00442/BIBTEX.
[90] M. N. Huda *et al.*, “Potential Use of Exosomes as Diagnostic Biomarkers and in Targeted Drug Delivery: Progress in Clinical and Preclinical Applications,” *ACS Biomater Sci Eng*, vol. 7, no. 6, pp. 2106–2149, Jun. 2021, doi: 10.1021/ACSBIOMATERIALS.1C00217/ASSET/IMAGES/LARGE/AB1C00217_0006.JPEG.
[91] A. Carretero-González, I. Otero, L. Carril-Ajuria, G. de Velasco, and L. Manso, “Exosomes: Definition, Role in Tumor Development and Clinical Implications,” *Cancer Microenvironment*, vol. 11, no. 1, p. 13, Jun. 2018, doi: 10.1007/S12307-018-0211-7.

[92] T. B. Steinbichler, J. Dudás, H. Riechelmann, and I. I. Skvortsova, “The role of exosomes in cancer metastasis,” *Semin Cancer Biol*, vol. 44, pp. 170–181, Jun. 2017, doi: 10.1016/J.SEMCANCER.2017.02.006.
[93] C. Rajagopal and K. B. Harikumar, “The Origin and Functions of Exosomes in Cancer,” *Front Oncol*, vol. 8, no. MAR, p. 66, Mar. 2018, doi: 10.3389/FONC.2018.00066.
[94] K. Brennan *et al.*, “A comparison of methods for the isolation and separation of extracellular vesicles from protein and lipid particles in human serum,” *Sci Rep*, vol. 10, no. 1, Dec. 2020, doi: 10.1038/S41598-020-57497-7.
[95] P. Li, M. Kaslan, S. H. Lee, J. Yao, and Z. Gao, “Progress in Exosome Isolation Techniques,” *Theranostics*, vol. 7, no. 3, p. 789, 2017, doi: 10.7150/THNO.18133.
[96] J. Chen *et al.*, “Review on Strategies and Technologies for Exosome Isolation and Purification,” *Front Bioeng Biotechnol*, vol. 9, p. 1378, Jan. 2022, doi: 10.3389/FBIOE.2021.811971/BIBTEX.
[97] K. Brennan *et al.*, “A comparison of methods for the isolation and separation of extracellular vesicles from protein and lipid particles in human serum,” *Scientific Reports 2020 10:1*, vol. 10, no. 1, pp. 1–13, Jan. 2020, doi: 10.1038/s41598-020-57497-7.
[98] B. J. Tauro *et al.*, “Comparison of ultracentrifugation, density gradient separation, and immunoaffinity capture methods for isolating human colon cancer cell line LIM1863-derived exosomes,” *Methods*, vol. 56, no. 2, pp. 293–304, Feb. 2012, doi: 10.1016/J.YMETH.2012.01.002.
[99] Z. Onódi *et al.*, “Isolation of high-purity extracellular vesicles by the combination of iodixanol density gradient ultracentrifugation and bind-elute chromatography from blood plasma,” *Front Physiol*, vol. 9, no. OCT, p. 1479, Oct. 2018, doi: 10.3389/FPHYS.2018.01479/BIBTEX.
[100] L. Filipović *et al.*, “Affinity-based isolation of extracellular vesicles by means of single-domain antibodies bound to macroporous methacrylate-based copolymer,” *N Biotechnol*, vol. 69, pp. 36–48, Jul. 2022, doi: 10.1016/J.NBT.2022.03.001.
[101] J. Chen *et al.*, “Review on Strategies and Technologies for Exosome Isolation and Purification,” *Front Bioeng Biotechnol*, vol. 9, p. 1378, Jan. 2022, doi: 10.3389/FBIOE.2021.811971/BIBTEX.
[102] “Expression of Constitutively Active Akt-3 in MCF-7 Breast Cancer Cells Reverses the Estrogen and Tamoxifen Responsivity of these Cells in Vivo1 | Clinical Cancer Research | American Association for Cancer Research.” https://aacrjournals.org/clincancerres/article/9/8/2933/204824/Expression-of-Constitutively-Active-Akt-3-in-MCF-7 (accessed Dec. 04, 2022).
[103] N. Bhardwaj, Y. P. Singh, and B. B. Mandal, “Silk Fibroin Scaffold-Based 3D Co-Culture Model for Modulation of Chondrogenesis without Hypertrophy via Reciprocal Cross-talk and Paracrine Signaling,” *ACS Biomater Sci Eng*, vol. 5, no. 10, pp. 5240–5254, Oct. 2019, doi: 10.1021/ACSBIOMATERIALS.9B00573/ASSET/IMAGES/LARGE/AB9B00573_0003.JPEG.
[104] S. Lee, S. H. Kim, Y. Y. Jo, W. T. Ju, H. B. Kim, and H. Kweon, “Effects of Ultraviolet Light Irradiation on Silk Fibroin Films Prepared under Different Conditions,” *Biomolecules*, vol. 11, no. 1, pp. 1–11, Jan. 2021, doi: 10.3390/BIOM11010070.

[105] U. L. Triantafillu, S. Park, and Y. Kim, “Fluid Shear Stress Induces Drug Resistance to Doxorubicin and Paclitaxel in the Breast Cancer Cell Line MCF7,” *Adv Ther (Weinh)*, vol. 2, no. 3, p. 1800112, Mar. 2019, doi: 10.1002/ADTP.201800112.
[106] R. C. Wang *et al.*, “Sensitivity of docetaxel-resistant MCF-7 breast cancer cells to microtubule-destabilizing agents including vinca alkaloids and colchicine-site binding agents,” *PLoS One*, vol. 12, no. 8, Aug. 2017, doi: 10.1371/JOURNAL.PONE.0182400.
[107] L. Li, C. C. Liu, X. Chen, S. Xu, S. H. Cortes-Manno, and S. H. Cheng, “Mechanistic study of bakuchiol-induced anti-breast cancer stem cell and in vivo anti-metastasis effects,” *Front Pharmacol*, vol. 8, no. OCT, p. 746, Oct. 2017, doi: 10.3389/FPHAR.2017.00746/BIBTEX.
[108] R. Z. Shi *et al.*, “Epithelial cell adhesion molecule promotes breast cancer resistance protein-mediated multidrug resistance in breast cancer by inducing partial epithelial–mesenchymal transition,” *Cell Biol Int*, vol. 45, no. 8, pp. 1644–1653, Aug. 2021, doi: 10.1002/CBIN.11598.
[109] J. S. Lim, G. Y. Jung, and S. Y. Park, “Nkx-2.5 Regulates MDR1 Expression via Its Upstream Promoter in Breast Cancer Cells,” *J Korean Med Sci*, vol. 34, no. 12, Apr. 2019, doi: 10.3346/JKMS.2019.34.E100.
[110] J. Hu, H. Zhang, L. Liu, B. Han, G. Zhou, and P. Su, “TRPS1 Confers Multidrug Resistance of Breast Cancer Cells by Regulating BCRP Expression,” *Front Oncol*, vol. 10, p. 934, Jun. 2020, doi: 10.3389/FONC.2020.00934/BIBTEX.
[111] F. Inci, “Benchmarking a Microfluidic-Based Filtration for Isolating Biological Particles,” *Langmuir*, vol. 38, no. 5, pp. 1897–1909, Feb. 2022, doi: 10.1021/ACS.LANGMUIR.1C03119/ASSET/IMAGES/MEDIUM/LA1C03119_0010.GIF.
[112] R. S. Hebbar, A. M. Isloor, and A. F. Ismail, “Contact Angle Measurements,” *Membrane Characterization*, pp. 219–255, Feb. 2017, doi: 10.1016/B978-0-444-63776-5.00012-7.
[113] M. A. Mohamed, J. Jaafar, A. F. Ismail, M. H. D. Othman, and M. A. Rahman, “Fourier Transform Infrared (FTIR) Spectroscopy,” *Membrane Characterization*, pp. 3–29, Jan. 2017, doi: 10.1016/B978-0-444-63776-5.00001-2.
[114] D. Peak, “Fourier Transform Infrared Spectroscopic Methods of Soil Analysis,” *Reference Module in Earth Systems and Environmental Sciences*, Jan. 2013, doi: 10.1016/B978-0-12-409548-9.05170-8.
[115] D. Kowalczuk and M. Pitucha, “Application of FTIR Method for the Assessment of Immobilization of Active Substances in the Matrix of Biomedical Materials,” *Materials*, vol. 12, no. 18, Sep. 2019, doi: 10.3390/MA12182972.
[116] G. Greczynski and L. Hultman, “X-ray photoelectron spectroscopy: Towards reliable binding energy referencing,” *Prog Mater Sci*, vol. 107, p. 100591, Jan. 2020, doi: 10.1016/J.PMATSCI.2019.100591.
[117] M. Aziz and A. F. Ismail, “X-Ray Photoelectron Spectroscopy (XPS),” *Membrane Characterization*, pp. 81–93, Jan. 2017, doi: 10.1016/B978-0-444-63776-5.00005-X.
[118] C. Gardiner, Y. J. Ferreira, R. A. Dragovic, C. W. G. Redman, and I. L. Sargent, “Extracellular vesicle sizing and enumeration by nanoparticle tracking analysis,” *J Extracell Vesicles*, vol. 2, no. 1, 2013, doi: 10.3402/JEV.V2I0.19671/SUPPL_FILE/ZJEV_A_11815495_SM0001.DOCX.

[119] D. Koga, S. Kusumi, M. Shibata, and T. Watanabe, "Applications of Scanning Electron Microscopy Using Secondary and Backscattered Electron Signals in Neural Structure," *Front Neuroanat*, vol. 15, p. 100, Dec. 2021, doi: 10.3389/FNANA.2021.759804/BIBTEX.
[120] K. C. A. Smith and C. W. Oatley, "The scanning electron microscope and its fields of application," *British Journal of Applied Physics*, vol. 6, no. 11, p. 391, Nov. 1955, doi: 10.1088/0508-3443/6/11/304.
[121] C. Achilli, A. Ciana, and G. Minetti, "Oxidation of cysteine-rich proteins during gel electrophoresis," *J Biol Methods*, vol. 5, no. 4, p. e104, Dec. 2018, doi: 10.14440/JBM.2018.275.
[122] R. Stringer, "ELECTROPHORESIS | Overview," *Encyclopedia of Analytical Science: Second Edition*, pp. 356–363, Jan. 2005, doi: 10.1016/B0-12-369397-7/00120-5.
[123] K. Webb, V. Hlady, and P. A. Tresco, "Relative importance of surface wettability and charged functional groups on NIH 3T3 fibroblast attachment, spreading, and cytoskeletal organization," *J Biomed Mater Res*, vol. 41, no. 3, p. 422, Sep. 1998, doi: 10.1002/(sici)1097-4636(19980905)41:3<422::aid-jbm12>3.0.co;2-k.
[124] J. Zhong, X. Zhou, C. Ye, W. Yu, and Y. Tang, "Using FTIR Imaging to Investigate Silk Fibroin-Based Materials," *Methods in Molecular Biology*, vol. 2347, pp. 207–219, 2021, doi: 10.1007/978-1-0716-1574-4_18/FIGURES/1.
[125] M. Aiman Mohtar, S. E. Syafruddin, S. N. Nasir, and L. T. Yew, "Revisiting the Roles of Pro-Metastatic EpCAM in Cancer," *Biomolecules 2020, Vol. 10, Page 255*, vol. 10, no. 2, p. 255, Feb. 2020, doi: 10.3390/BIOM10020255.
[126] R. Shi *et al.*, "Downregulation of cytokeratin 18 induces cellular partial EMT and stemness through increasing EpCAM expression in breast cancer," *Cell Signal*, vol. 76, p. 109810, Dec. 2020, doi: 10.1016/J.CELLSIG.2020.109810.
[127] Y. Cheng *et al.*, "Cytokeratin 18 regulates the transcription and alternative splicing of apoptotic-related genes and pathways in HeLa cells," *Oncol Rep*, vol. 42, no. 1, pp. 301–312, Jul. 2019, doi: 10.3892/OR.2019.7166/HTML.
[128] U. Woelfle, G. Sauter, S. Santjer, R. Brakenhoff, and K. Pantel, "Down-Regulated Expression of Cytokeratin 18 Promotes Progression of Human Breast Cancer," *Clinical Cancer Research*, vol. 10, no. 8, pp. 2670–2674, Apr. 2004, doi: 10.1158/1078-0432.CCR-03-0114.
[129] R. Shi *et al.*, "Downregulation of cytokeratin 18 enhances BCRP-mediated multidrug resistance through induction of epithelial-mesenchymal transition and predicts poor prognosis in breast cancer," *Oncol Rep*, vol. 41, no. 5, pp. 3015–3026, May 2019, doi: 10.3892/OR.2019.7069.
[130] V. Mittal, "Epithelial Mesenchymal Transition in Tumor Metastasis," *https://doi.org/10.1146/annurev-pathol-020117-043854*, vol. 13, pp. 395–412, Jan. 2018, doi: 10.1146/ANNUREV-PATHOL-020117-043854.
[131] R. Kalluri and R. A. Weinberg, "The basics of epithelial-mesenchymal transition," *J Clin Invest*, vol. 119, no. 6, p. 1420, Jun. 2009, doi: 10.1172/JCI39104.
[132] C. F. Thorn *et al.*, "Doxorubicin pathways: pharmacodynamics and adverse effects," *Pharmacogenet Genomics*, vol. 21, no. 7, p. 440, 2011, doi: 10.1097/FPC.0B013E32833FFB56.
[133] K. A. Lyseng-Williamson and C. Fenton, "Docetaxel: A review of its use in metastatic breast cancer," *Drugs*, vol. 65, no. 17, pp. 2513–2531, Sep. 2005, doi: 10.2165/00003495-200565170-00007/FIGURES/TAB6.

[134] M. Imran, S. Saleem, A. Chaudhuri, J. Ali, and S. Baboota, "Docetaxel: An update on its molecular mechanisms, therapeutic trajectory and nanotechnology in the treatment of breast, lung and prostate cancer," *J Drug Deliv Sci Technol*, vol. 60, p. 101959, Dec. 2020, doi: 10.1016/J.JDDST.2020.101959.
[135] G. L. David *et al.*, "MDR1 promoter hypermethylation in MCF-7 human breast cancer cells: changes in chromatin structure induced by treatment with 5-Aza-cytidine," *Cancer Biol Ther*, vol. 3, no. 6, pp. 540–548, 2004, doi: 10.4161/CBT.3.6.845.
[136] K. L. Mealey, "Therapeutic implications of the MDR-1 gene," *J Vet Pharmacol Ther*, vol. 27, no. 5, pp. 257–264, Oct. 2004, doi: 10.1111/J.1365-2885.2004.00607.X.
[137] M. M. Gottesman and I. H. Pastan, "The Role of Multidrug Resistance Efflux Pumps in Cancer: Revisiting a JNCI Publication Exploring Expression of the MDR1 (P-glycoprotein) Gene," *JNCI Journal of the National Cancer Institute*, vol. 107, no. 9, p. 222, Sep. 2015, doi: 10.1093/JNCI/DJV222.
[138] T. Nakanishi and D. D. Ross, "Breast cancer resistance protein (BCRP/ABCG2): its role in multidrug resistance and regulation of its gene expression," *Chin J Cancer*, vol. 31, no. 2, p. 73, 2012, doi: 10.5732/CJC.011.10320.
[139] L. A. Doyle and D. D. Ross, "Multidrug resistance mediated by the breast cancer resistance protein BCRP (ABCG2)," *Oncogene 2003 22:47*, vol. 22, no. 47, pp. 7340–7358, Oct. 2003, doi: 10.1038/sj.onc.1206938.
[140] N. Ludwig, T. L. Whiteside, and T. E. Reichert, "Challenges in Exosome Isolation and Analysis in Health and Disease," *Int J Mol Sci*, vol. 20, no. 19, Oct. 2019, doi: 10.3390/IJMS20194684.
[141] R. Xu, D. W. Greening, H. J. Zhu, N. Takahashi, and R. J. Simpson, "Extracellular vesicle isolation and characterization: toward clinical application," *J Clin Invest*, vol. 126, no. 4, p. 1152, Apr. 2016, doi: 10.1172/JCI81129.
[142] B. M. Hussen *et al.*, "Strategies to overcome the main challenges of the use of exosomes as drug carrier for cancer therapy," *Cancer Cell International 2022 22:1*, vol. 22, no. 1, pp. 1–23, Oct. 2022, doi: 10.1186/S12935-022-02743-3.
[143] S. Allelein *et al.*, "Potential and challenges of specifically isolating extracellular vesicles from heterogeneous populations," *Scientific Reports 2021 11:1*, vol. 11, no. 1, pp. 1–12, Jun. 2021, doi: 10.1038/s41598-021-91129-y.
[144] K. Aubertin *et al.*, "Massive release of extracellular vesicles from cancer cells after photodynamic treatment or chemotherapy," *Scientific Reports 2016 6:1*, vol. 6, no. 1, pp. 1–11, Oct. 2016, doi: 10.1038/srep35376.
[145] N. Tominaga, K. Hagiwara, N. Kosaka, K. Honma, H. Nakagama, and T. Ochiya, "RPN2- mediated glycosylation of tetraspanin CD63 regulates breast cancer cell malignancy,"Mol Cancer, vol. 13, no. 1, p. 134, May 2014, doi: 10.1186/1476-4598-13-134.
[146] E. J. K. Kowal, D. Ter-Ovanesyan, A. Regev, and G. M. Church, "Extracellular Vesicle Isolation and Analysis by Western Blotting," Methods Mol Biol, vol.1660, pp. 143–152, 2017, doi: 10.1007/978-1-4939-7253-1_12/FIGURES/2.
[147] J. Jankovičová, P. Sečová, K. Michalková, and J. Antalíková, "Tetraspanins, More than Markers of Extracellular Vesicles in Reproduction," Int J Mol Sci, vol. 21,no. 20, pp. 1– 30, Oct. 2020, doi: 10.3390/IJMS21207568.
[148] M. Frolikova et al., "CD9 and CD81 Interactions and Their Structural Modelling in Sperm Prior to Fertilization," International Journal of Molecular Sciences 2018,

Vol. 19, Page 1236, vol. 19, no. 4, p. 1236, Apr. 2018, doi:10.3390/IJMS19041236.
[149] R. Shi et al., “Downregulation of cytokeratin 18 enhances BCRP-mediated multidrug resistance through induction of epithelial-mesenchymal transition and predicts poor prognosis in breast cancer,” Oncol Rep, vol. 41, no. 5, pp. 3015–3026, May 2019, doi: 10.3892/OR.2019.7069/HTML.